

Dissertation in Astronomy
submitted to the
Combined Faculties of the Natural Sciences and Mathematics
of the Ruperto-Carola-University of Heidelberg, Germany,
for the degree of
Doctor of Natural Sciences

Put forward by
M.Sc. *Dading Nugroho*
born in Batu, Indonesia

Oral examination: 31.10.12

**Diagnosing galaxy merger events
in the recent past of Active Galactic Nuclei:
An Integral Field Spectroscopy perspective**

Dading Nugroho
Max-Planck-Institut für Astronomie

Referees: Dr. Knud Jahnke
Prof. Dr. Jochen Heidt

Zusammenfassung

Wir untersuchen die räumlich aufgelösten kinematischen Eigenschaften von Wirtsgalaxien von Typ-1-Quasaren mit einer Rotverschiebung $z < 0.2$. Basierend auf der Kombination einer kinematischen Analyse mit morphologischen Informationen aus optischen Bilddaten detektieren wir Störungen des Geschwindigkeitsfeldes und der Morphologie, um die Bedeutung großer Verschmelzungen (“major mergers”) für die Auslösung von Quasar-Aktivität zu analysieren.

Wir präsentieren die Ergebnisse der Analyse von 19 Quasar-Wirtsgalaxien, die mit dem VIMOS-Feldspektrographen beobachtet wurden. Wir entwerfen ein quantitatives Klassifikationsschema für die Störungen der Geschwindigkeitsfelder und zeigen, dass die Fälle von Störungen in den Geschwindigkeitsfeldern und in optischen Bilddaten im allgemeinen miteinander konsistent sind. Das Vorherrschen schwacher Störungssignaturen deutet darauf hin, dass sich die Mehrheit der von uns untersuchten Quasare nicht in dem intensivsten Teil des Verschmelzungsprozesses befindet.

Weiterhin untersuchen wir eine mögliche Beziehung zwischen dem Wechselwirkungszustand der Wirtsgalaxie und dem Grad an Aktivität des supermassereichen schwarzen Loches. Auf Grundlage unseres Samples finden wir keine Abhängigkeit der Akkretionsrate von der Masse des schwarzen Loches oder dem Störungszustand der Wirtsgalaxie. Folglich können wir die Hypothese, dass große Verschmelzungen der dominanteste Mechanismus für die Auslösung von Quasar-Aktivität seien, nicht bestätigen.

Abstract

We investigate the spatially resolved kinematics properties of type 1 quasar host galaxies with redshift $z < 0.2$. Using combination of kinematic analysis with morphological information from optical imaging data, we diagnose the existence of disturbances in velocity field and morphology to study the importance of major merger to ignite quasar activity.

We present results of 19 quasar host galaxies analysis observed with VIMOS integral field spectrograph. We construct a quantitative distortion classification scheme for the velocity fields and we demonstrate that the occurrences of distortion in the velocity fields and optical imaging are generally consistent with each other. The prevalence of mild level of distortion signatures indicates that majority of our quasars are not in the most intense part of galaxies merger process.

Further, we investigate a possible relation between interaction state of the host galaxy and level of supermassive black hole activity. Using our sample, we find there is no dependency of accretion rate on neither black hole mass nor distortion state of the host galaxy and is therefore unable to support the hypothesis that major merger is the most dominant fueling mechanism to ignite quasar activity.

CONTENTS

1	INTRODUCTION	1
1.1	STATE OF THE ART AGN HOST GALAXIES STUDY	2
1.1.1	GALAXIES EVOLUTION	2
1.1.2	SCALING RELATIONS	4
1.2	AGN FUELING MECHANISMS	6
1.2.1	INTERNAL PROCESSES	7
1.2.2	EXTERNAL PROCESSES	7
1.3	MAJOR MERGER – AGN ACTIVITY – STAR FORMATION HYPOTHESIS	8
1.4	PLAN OF THE THESIS	10
1.4.1	STRATEGY/APPROACH	11
1.4.2	INTEGRAL FIELD SPECTROSCOPY	11
1.4.3	SIGN OF DISTURBANCES IN IMAGING AND KINEMATICS	13
2	SAMPLE AND OBSERVATIONS	15
2.1	SAMPLE	15

2.1.1	HAMBURG/ESO SURVEY QSO SAMPLE	15
2.1.2	A PREVIOUS MULTICOLOR STUDY OF THE SAMPLE	18
2.2	OBSERVATIONS	18
2.2.1	VIMOS DESCRIPTION	18
2.2.2	OBSERVING STRATEGY	20
3	DATA PREPARATION & REDUCTION	21
3.1	VIMOS DATA REDUCTION	21
3.1.1	RAW DATA DESCRIPTION	22
3.1.2	SPECTRA TRACING	23
3.1.3	DISTORTION AND DISPERSION CORRECTIONS	23
3.1.4	BUILDING THE DATA CUBE (DAR CORRECTION)	24
3.1.5	SKY SUBTRACTION	24
3.1.6	FLUX CALIBRATION	25
3.2	OPTICAL IMAGING	25
3.3	QUASAR – HOST GALAXY DECOMPOSITION	25
4	EXTRACTION OF PHYSICAL PARAMETERS	33
4.1	EMISSION LINE FITTING	33
4.1.1	VELOCITY FIELDS	34
4.1.2	BPT DIAGRAM	34
4.1.3	BLACK HOLE PARAMETER MEASUREMENTS	36
4.2	KINEMATIC ANALYSIS	37
4.2.1	HARMONIC EXPANSION	37
4.2.2	VELOCITY FIELD CLASSIFICATION SCHEME	39

5	RESULTS: BLACK HOLE PARAMETERS AND PHYSICAL CONDITIONS OF THE IONIZED GAS	41
5.1	BLACK HOLE PARAMETERS	41
5.2	BPT DIAGRAMS	41
6	RESULTS: KINEMATICS PROPERTIES OF QUASAR HOST GALAXIES	51
6.1	OPTICAL IMAGES AND VELOCITY FIELDS	51
6.1.1	HE0952 – 1552	51
6.1.2	HE1019 – 1414	53
6.1.3	HE1020 – 1022	53
6.1.4	HE1029 – 1401	53
6.1.5	HE1043 – 1346	53
6.1.6	HE1110 – 1910	53
6.1.7	HE1201 – 2409	58
6.1.8	HE1228 – 1637	58
6.1.9	HE1237 – 2252	58
6.1.10	HE1239 – 2426	58
6.1.11	HE1254 – 0934	58
6.1.12	HE1300 – 1325	63
6.1.13	HE1310 – 1051	65
6.1.14	HE1315 – 1028	65
6.1.15	HE1335 – 0847	65
6.1.16	HE1338 – 1423	65
6.1.17	HE1405 – 1545	65
6.1.18	HE1416 – 1256	65
6.1.19	HE1434 – 1600	71

6.2	VELOCITY CLASSIFICATION RESULTS	71
7	DISCUSSION AND CONCLUSIONS	77
7.1	LINKING TOGETHER ALL RESULTS	78
7.2	CONCLUDING REMARKS AND FUTURE OUTLOOK	84
A	APPENDIX A: RESULTS OF THE QUASAR – HOST GALAXY DECOMPOSITION	87
B	APPENDIX B: BLACK HOLE PARAMETER MEASUREMENTS	107
	BIBLIOGRAPHY	116

The study of Active Galactic Nucleus (AGN) is one of main science driver for major astronomical facilities and an extremely active subject in astronomy. The term "active galactic nucleus" was introduced by [Ambartsumian \(1971\)](#) to emphasize differences between activity of the central part of a galaxy (also called nucleus) and in other parts. Physical processes that could occur in the nucleus are for example: "the violent motions of gaseous clouds, considerable excess of radiation in the ultraviolet, relatively rapid changes of brightness, expulsion of jets and condensations" ([Ambartsumian 1971](#)). Brad Peterson classified AGN as "the existence of energetic phenomena in the nuclei, or central regions, of galaxies which can not be attributed clearly and directly to stars" ([Peterson 1997](#)).

The energy output of an AGN can reach 10^4 times the luminosity of a typical galaxy or around $10^{15}L_{\odot}$, which makes AGN the most energetic class of objects in the universe and is remarkably that this energy is produced in a small region (of order $\sim 10AU$). Various mechanism have been proposed to explain such energetic nuclear activity. This started with the idea of a supermassive star (with mass $10^5M_{\odot} - 10^8M_{\odot}$) as a source for gravitational and thermonuclear energy ([Hoyle & Fowler 1963](#)) and in the same paper they also mentioned the possibility of gravitational collapse to explain the energetic nature of the nucleus. [Zel'dovich \(1964\)](#), [Salpeter \(1964\)](#) and [Lynden-Bell \(1969\)](#) followed this with modified ideas, i.e. gravitational accretion onto a supermassive ($M > 10^6M_{\odot}$) collapsed object, for example massive black holes.

The first observational report of an AGN observation was made by [Fath \(1909\)](#), who reported their analysis of the spectrum of NGC 1068. He wrote that the spiral nebula ¹ NGC 1068 has absorption features produced from a collection of large number of stars and six emission line

¹He used term "spiral nebula" instead of "galaxy" which is common before the Shapley – Curtis Debate on 26 April 1920 on the nature of spiral nebulae and the size of the universe. William Herschel used the term "Spiral Nebula" for the first time when he made his deep sky objects catalogue in 1786.

features similar to the spectra of planetary nebulae in the Milky Way galaxy. During the following years, [Slipher \(1917\)](#) confirmed [Fath's](#) analysis of NGC 1068 using better spectra, and [Edwin Hubble](#) in 1926 reported planetary–nebulae–like features for three extragalactic nebulae (NGC 1068, NGC 4051, NGC 4151). [Humason \(1932\)](#) reported emission line studies of two further extragalactic nebulae, NGC 1275 and [Mayall 1934](#).

[Carl Seyfert](#) carried out the first systematic study of 12 known objects at that time. He found that their nuclei are luminous and have semi-stellar appearance (i.e. point-like), their spectra show nebular spectra of high ionization emission lines with widths larger than that of the absorption features.

1.1 STATE OF THE ART AGN HOST GALAXIES STUDY

Since the first observation of AGN by [Fath \(1909\)](#), who observed and studied spectrum of NGC 1068, there are so many developments in our understanding about AGN. The rapid development also resulted more questions into our current knowledge and understanding about AGN in particular and galaxies in general.

One important results from that development is about unification of AGN (e.g. [Urry & Padovani 1995](#)).

According to the unified AGN model (shown in [figure 1.1](#)), supermassive black hole in the center surrounded by accretion disk. The accretion disk emits thermal emission in the form of UV/optical continuum. The outer part of the accretion disk meets with inner part of the broad line region (BLR) which produces broad emission lines. The outer part of the BLR connected with inner region of so called dust torus structure. The distance of the inner part of torus characterized by minimum distance from the center where dust can exist called the dust sublimation radius. All of the structures which mentioned before are enclosed by narrow line region (NLR) which produces narrow emission lines. Additional feature which common but not observed in every object is jet. In [table 1.1](#), we present more quantitative description about AGN structure according to the unified AGN model based on [Roger Blandford's](#) lecture note for Saas-Fee Advanced Courses, [Blandford et al. \(1990\)](#).

1.1.1 GALAXIES EVOLUTION

In standard structure formation model (e.g. [Benson 2010](#)), theory of galaxy formation prescribed within Λ -cold dark matter cosmological model (Λ CDM). Seeds manifest as matter density per-

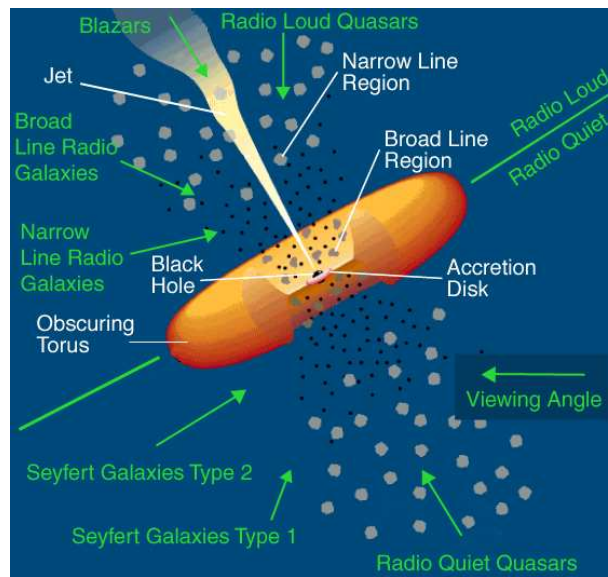


Figure 1.1: AGN unified model complemented with additional labels to point out specific feature/structure and the differences among different families in the AGN zoo. *Source:* http://www.auger.org/news/PRagn/images/agn4_prouza.png

turbations in early universe and Inflation expands to cosmological scale. Through the time, dark matter density perturbations will evolve and form dark matter halos. Dark matter halo is nearly stable structure supported by random motion of its components. From smallest scale perturbations, the first dark matter halo generation formed and merging of dark matter halos will produce later generation. Baryon matter expected to follow dark matter distribution and concentrate in the center of dark matter haloes.

Galaxies form as baryonic condensations in the center of dark matter haloes. In this picture of Λ -cold dark matter (Λ CDM) structure formation dark matter haloes and galaxies are built up hierarchically, larger structure resulting from the merger of smaller structures. As a result, a diverse set of galaxies with very different masses and ages has formed over time.

We² follow constraints from Baldry et al. (2004) to construct Color Magnitude Diagram (CMD) of galaxies in local universe shown in figure 1.2. From the database, we select galaxies with magnitude $13.5 < r < 17.77$, redshift $0.004 < r < 0.08$ and absolute magnitude $-23.5 < M_r < -15.5$. Total number of galaxies from these selection is 152,130 galaxies. Bell et al. (2004) and Faber et al. (2007) investigate luminosity function of galaxies at $z \sim 1$ until present day universe

²We use the term "We" instead of "I" in this thesis to show that this thesis is not purely produced by the work of one single person. During the journey of this thesis, some people also contribute (data reduction, discussions, language checking etc.) to this work with the main work is done by the author.

Table 1.1: Quantitative description of unified AGN model

Distance from the center	Structure/Properties
~ 2 AU	Supermassive black hole, event horizon
~ 20 AU	Relativistic accretion disk
~ 200 AU	UV accretion disk
~ 2000 AU	Broad line region (BLR)
0.1 pc	outer part of BLR
1 pc	Star conglomeration with Keplerian orbit
10 pc	Inner part of the narrow line region
100 pc	Bulge
1 kpc	Jet, additional inner structure of galaxy (e.g. inner disk, bar), extended narrow line region (ENLR).
10 kpc	Host galaxy, ENLR
100 kpc	Jet, companion galaxies, gravitational interaction
1 Mpc	Jet, radio lobe and hotspots, interaction with nearby large scale structure

Notes. Source: http://www.astro.virginia.edu/class/whittle/ast553/Topic12/Lecture_12.html

and they found that the number of red galaxies is increasing since $z \sim 1$, contrary with the number of blue galaxies which approximately constant. One possible implication from this finding is that blue galaxies can provide progenitors to form red galaxies. Faber et al. (2007) proposed three mechanisms to form red galaxies.

1. Evolutionary scenario started with small blue galaxies. Early star formation quenching happened to these galaxies hence it will move galaxies to redder color and mass growth achieved with dry mergers at the red sequence.
2. Second scenario started with late star formation quenching. Mass accumulation occurred when galaxies still at blue cloud and after that galaxies getting redder and not involved in any merger processes at red sequence.
3. A combination of the two above.

Independently of which scenario actually applies, the necessary ingredients are merging, aging and a mechanism to truncate star formation before galaxies can arrive at the red sequence.

1.1.2 SCALING RELATIONS

Before mid 1990s, AGN studies are kind of detached with galaxies formation and evolution studies but since the discovery of possible relation between supermassive black hole in the center of

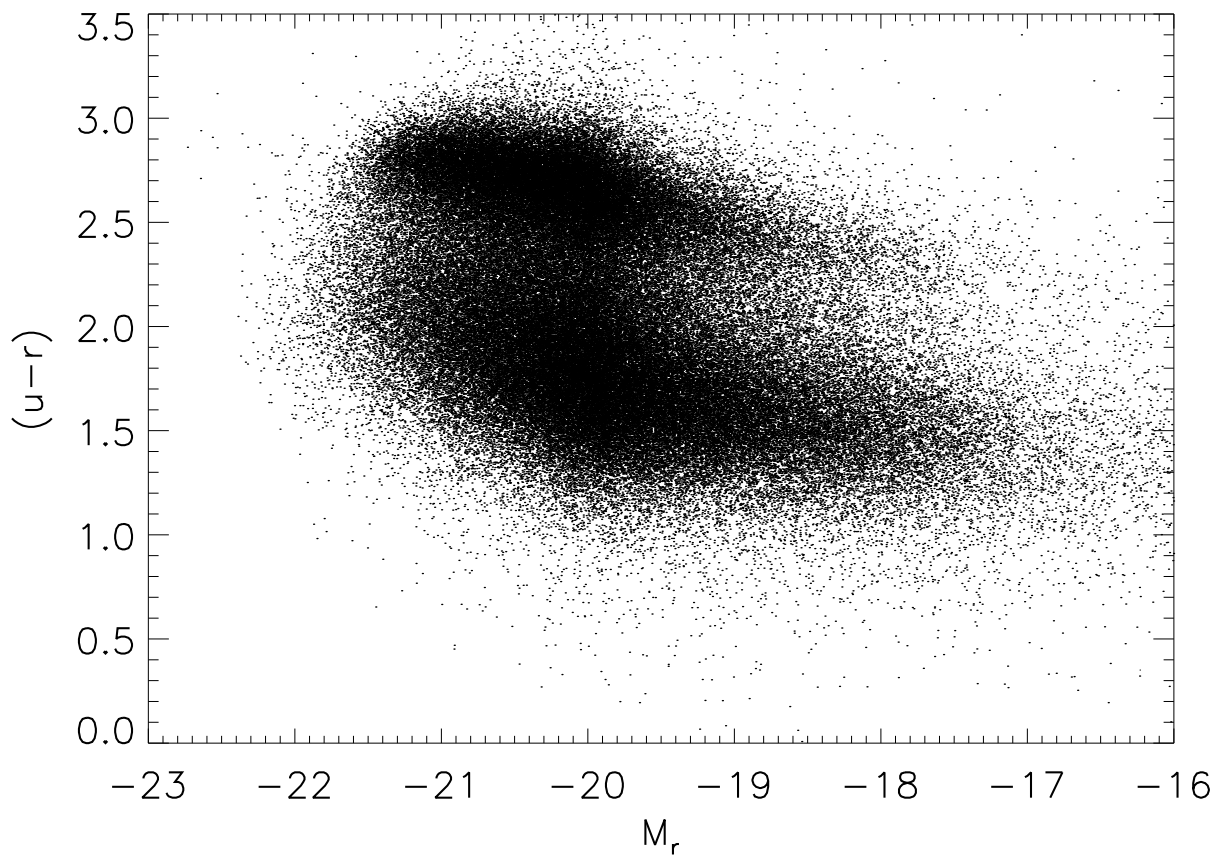


Figure 1.2: Distribution of 152,130 SDSS galaxies in color magnitude diagram of galaxies in local universe. There are two recognizable distribution, "red sequence" galaxies and "blue cloud" galaxies. The third additional type is "green valley" galaxy correspond to transition region between other two types.

galaxies with their host galaxies, those two studies were more closely connected. Supermassive black hole are also discovered not only in active galaxies but also in inactive galaxies, for example work by [Kormendy & Richstone \(1992\)](#) in NGC 3115 and in our Milky way galaxy [Genzel et al. \(1997\)](#). A coupled history and potential physical connection of black hole and galaxy growth is possible, though not yet proven.

A lot of literature was published reporting studies of relation between host galaxy properties and its supermassive black hole properties. It begun with work of [Kormendy & Richstone \(1995\)](#) who reported and suggested a correlation between the total blue magnitude of the host spheroids³ and supermassive black hole mass (M_{BH}). Another relation found by [Magorrian et al. \(1998\)](#),

³Generic term of "spheroid" refers to spheroid shaped structure from a galaxy, for spiral galaxy this refers to

suggested a correlation between the supermassive black hole mass and bulge mass. Two independent groups (Ferrarese & Merritt 2000; Gebhardt et al. 2000) found a relation between supermassive black hole mass and stellar velocity dispersion (σ) in the galaxy bulge. Different types of relation were suggested and found in the following years for example supermassive black hole mass and infrared luminosity (Marconi & Hunt 2003), supermassive black hole mass and bulge mass (Marconi & Hunt 2003; Häring & Rix 2004), supermassive black hole mass and number of globular clusters (Berkert & Tremaine 2010; Snyder et al. 2011).

Tight relation between black hole mass and host galaxy properties indicates possible connection between black hole growth and host galaxy evolution. The idea of black hole and host galaxy coevolution also developed by advancement of theoretical study of galaxy formation and evolution within cosmological structure formation. Peng (2007) and Jahnke & Macciò (2011) showed that M_{BH} and galaxy total mass (M_{gal}) relation can be produced by random merging events hence their results support a non-causal relation between black hole mass and galaxy total mass.

1.2 AGN FUELING MECHANISMS

The central and yet not fully solved problem is how to transport gas into the supermassive black holes in the centers of galaxies let the black hole grows and to ignite an AGN. It requires full knowledge of what happens on the various scale from Mpc (galaxy environment) until micro parsec (surrounding the black hole). Different conditions and physical mechanisms exist and are at work at different scales and we can probe a limited scale with each observation. This has the consequence for observational studies that a single set of data can only probe part of the picture. Nevertheless, for single object studies observation for different scale can be used in order to create a full physical interpretation about what drives the gas from galactic scales to the inner part of galaxies and fueling the supermassive black hole. An additional dimension is to investigate large numbers of objects provide statistical significance to a study beyond single objects. AGN fueling is the reduction of angular momentum of matter (gas or star) relative to the supermassive black hole. See e.g. Combes (2001), Martini (2004), Jogee (2006) for more detailed reviews. In general, one can divide the mechanisms responsible for angular momentum transfer into two broad classes: mechanisms internal to the galaxies and those triggered by external events.

bulge part and for elliptical galaxy case this would be the whole galaxy

1.2.1 INTERNAL PROCESSES

Proposed fueling mechanisms which are based on internal processes inside a galaxy itself are for example: gravitational torques by large scale bar or nuclear bars, dynamical friction on molecular clouds can move the cloud toward smaller radius, stellar disruption of stars due to tidal interaction with the black hole and stellar mass loss or supernovae feedback producing low angular momentum wind. Some of these processes can only provide low rates of fuel (e.g. stellar disruption) and clearly ruled out as the dominant processes for high-L AGN. Instabilities, however, are good candidates also for this population (Hopkins & Quataert 2010).

1.2.2 EXTERNAL PROCESSES

External processes can potentially be more violent and can involve large masses. Galaxy mergers are one expected physical consequence of the bottom-up large scale structure formation in our universe, supported by vast observational evidence. Merger processes can be classified into two main types, major mergers and minor mergers with the mass ratio (μ) as a deciding criteria. We follow the definition used by Hopkins et al. (2010), who define mergers of two structures with mass ratio larger than $\mu = 1/4$ as major mergers and merger with mass ratios less than that as minor mergers. According to Hopkins et al. (2010) definition of mass which is used also important in studying merger process. There are three alternatives of mass definition, stellar galaxy mass, baryonic (stellar and gas) mass and halo mass.

There is a lot of observational evidence for galaxy merger processes. For example, our own Milky Way shows signature of minor mergers with small satellite galaxies, indicating ongoing mass accumulation processes from smaller structures. The Sloan Digital Sky Survey (SDSS) produced an unprecedented star map which enables scientist to find and measure in detail stellar streams for example the famous Sagittarius stream discovered by Ibata et al. (1995) analysed with SDSS data by Belokurov et al. (2006). Stellar streams are also observed for other nearby galaxies, for example the Andromeda galaxy/M31 by the Pan-Andromeda Archaeological Survey (PAndAS) (Mackey et al. 2010), or NGC 5907 (Martínez-Delgado et al. 2008). Even for nearby galaxies detecting and studying streams and minor merger are already challenging tasks and for distant galaxies it becomes increasingly difficult. Inside the Milky way, a large number of stars make up confusing foreground or background objects, increasing the difficulties to study a specific stellar distribution as tracers for stellar streams. Even for nearby objects, faint tidal features can be found at really low surface brightness (larger than 28.5 mag arcsec²) hence we need dedicated observational strategies to obtain deep images.

AGN host galaxies exist in various conditions and environments. It has been clear for a long

time that some of AGN host galaxies found to be interacting systems or isolated galaxies with remnants of gravitational interaction. Advancement of detector and space based telescope technology complemented with development of data analysis techniques brought a rapid progress for imaging studies of AGN host galaxies. For 20 quasars with redshift $z < 0.3$ Bahcall et al. (1997), found that three quasars are strongly interacting system, McLure et al. (1999) found 14 out of 19 AGN are interacting or shows sign of gravitational interaction and Jahnke et al. (2004a) found 9 out of 19 quasars with signs of interactions. These studies suggest that gravitational interaction could play a role in triggering AGN activity but definite conclusions could only drawn after comparison of AGN samples with comparison samples of inactive galaxies with similar properties. Cisternas et al. (2011) investigated 140 X-ray selected AGN host galaxies and a control sample of 1264 inactive galaxies at redshifts $0.3 < z < 1.0$ and suggest that major merger is not the dominant process to trigger AGN activity due to an absent significant difference between the distortion fractions for AGN and the inactive galaxies in the control samples.

1.3 MAJOR MERGER – AGN ACTIVITY – STAR FORMATION HYPOTHESIS

An extension of the above picture is the suggestion, that major mergers could be responsible also for other properties and phenomena in the inner region of a galaxy such as formation of the bulge, starburst and nuclear star cluster. From the study of Ultra Luminous Infra Red Galaxies (ULIRGs), (Sanders et al. 1988a,b) suggested an evolutionary sequence from ULIRG to optical quasars and they showed that ULIRG morphologies are often strongly interacting while showing large amount of gas for fueling starbursts.

Motivated by these observational facts, AGN and galaxy experts developed a model/framework which connects those three important effects: major merging, AGN activity and star formation. One of the prominent examples is the work by Hopkins et al. (2010), Figure 1.3 shows a proposed schematic framework of the phases from an isolated disk galaxy, through a major merger to produced a "dead" elliptical galaxy.

In this picture the first phase is an isolated disk galaxy dominated by internal secular processes driven by internal structures such as spiral arms, bars and the halo. These secular processes are claimed to be able already to fuel a supermassive black hole in the center, but with a low accretion rate to produce Seyfert –galaxy–like luminosity. This galaxy is a member of a larger structure and only near neighbors can affect this galaxy. Depending on galaxy mass and distance of each other, possible gravitational interaction are: weak/distant encounters (dynamical friction, tidal interaction) and strong/close encounters (mergers). For close/strong encounter, two rich gas disc galaxies can merge and gravitational torques can resulting inflow of gas which can be use for star formation and fueling of the supermassive black hole. Star formation rate would be increasing.

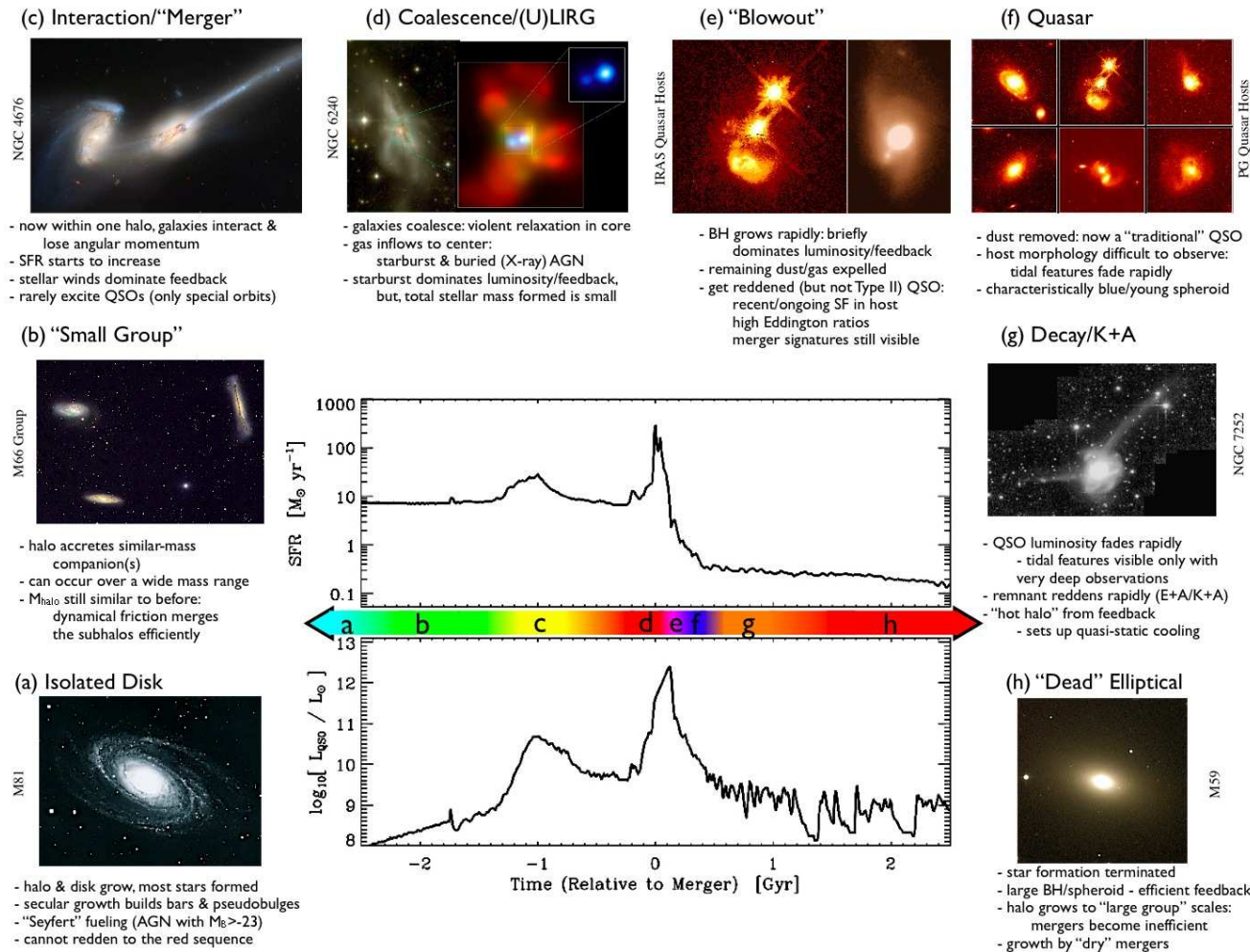


Figure 1.3: An example of a proposed theoretical framework connecting galaxies merger and AGN activity by Hopkins et al. (2010). See text for an explanation.

For the final stage of a merger, the two galaxies coalesce and the gas inflow rate would be larger than during the initial merger stage, producing starburst activity and a higher AGN luminosity. Feedback from starburst and black hole activity can disperse the remaining gas (referred to as "blowout" phase) during short period of time. For the next stage, star formation and AGN activity would be decreasing due to lack of fuel and as dust was removed by the blowout. This shows as an optically quasar phase with an observable host galaxy. Stellar population of the merger remnant shows post-starburst signature (K+A or E+A). The product in this framework is a red and dead elliptical galaxy with no star formation. Previous starburst activity decays and the galaxy changes its color towards red rapidly, moving from blue cloud to red sequence galaxy in the galaxy CMD.

The main objective of this thesis is to test this merger hypothesis by investigating 19 type 1 quasars⁴ through data obtained with the VIMOS integral field unit (IFU) mounted on the Very Large Telescope (VLT). We investigate the kinematic properties of these quasar host galaxies using emission lines of ionized gas and diagnose disturbances in the velocity fields. These data also enable us to study the spatially resolved ionization state of the interstellar medium (ISM) as well as star formation rates. We combine our analysis with a morphology analysis of the same galaxy sample as presented by Jahnke et al. (2004a) plus new high-resolution HST images to test the importance of major mergers in triggering AGN activity.

1.4 PLAN OF THE THESIS

The outline of this thesis is as follows: we motivate and lay out the scientific question on the relevance of mergers to fuel quasars and our approach of using a kinematical analysis in combination with optical imaging in chapter 1 using kinematics approach combined with optical imaging in chapter 1. In chapter 2, we describe our data sample and observations. We then discuss the non-trivial VIMOS data preparation and data reduction in chapter 3, including our quasar–host galaxy decomposition method for integral field spectroscopy data. In chapter 4, we describe our steps of analysis to extract the physical parameters such as emission lines fluxes, velocity, black hole parameters as well as the approach to kinematics analysis. Results for the physical conditions of the ionized gas and black hole parameters are presented in chapter 5. In chapter 6 we present results of our kinematics analysis. In chapter 7 we discuss the implications of our results for answering the scientific question. Throughout this thesis we adopt concordance cosmology with $H_0 = 73$ km/sec/Mpc, $\Omega_{matter} = 0.27$, $\Omega_{vacuum} = 0.73$

⁴The original definition of quasar is a quasi–stellar radio source and the original definition of QSO is quasi stellar objects. We use the term "quasar" to refer both "quasar" and "QSO" as similar objects.

1.4.1 STRATEGY/APPROACH

The most widely used method to probe galaxy structure/morphology with respect to distortions as signs of post merging is the use of imaging data through galaxy images. We can study the distribution of stellar components or with narrow-band imaging also of ionized gas, in order to analyze the galaxy morphology and identify potential additional features marking deviations from a, e.g. tidal tails or loops. Imaging of quasar host galaxies improved greatly since the onset of space based information (Hubble Space Telescope) as well as the use of adaptive optics for ground based telescopes. Morphology studies show AGN host galaxies to exist with a wide range of morphologies and environments, being strongly interacting systems to being smooth isolated galaxies (e.g. Bahcall et al. 1997; Jahnke et al. 2004a). More detailed studies of AGN host galaxies and matching control sample of inactive galaxies find that majority of AGN host galaxies out to $z = 1$ and for stellar mass $M_* \lesssim 10^{11} M_\odot$ do not have mergers signature, and the fraction of strongly distorted galaxies is similar for AGN host and inactive galaxies (Cisternas et al. 2011).

A completely complementary approach which is more time consuming than imaging is the kinematical analysis by studying relative velocities and velocity dispersions of the emission and absorption across a galaxy. We can infer kinematic properties of AGN host galaxies from this approach, for example systematic deviations from circular velocity, and at the same time in principle also determine gas properties (ionization states, abundances, metallicities), stellar properties (stellar populations, star formation history). Spectroscopically studying of AGN host galaxies is challenging in particular for type 1 AGN because the faint host galaxy emission coexist with the bright nuclear emission. Sophisticated techniques to decompose nucleus and host galaxy are needed in order to study type 1 AGN host galaxy.

1.4.2 INTEGRAL FIELD SPECTROSCOPY

The transition from aperture spectroscopy to long slit spectroscopy in its time produced a rapid development in astronomy, in parallel with the advancement of modern detector technology. The next step is the transition from long slit to integral field spectroscopy (hereafter IFS) also known as 3D spectroscopy. The common motivation is, to avoiding loss of light because of the narrow slit geometry and that astronomical objects and regions of interest are often more complex than a long-slit can accommodate. The main idea for IFS is to divide the telescope focal plane into a number of elements, which can be achieved using lenslets, fibers, slicers or combination of them and to create a pseudo-slit to disperse the light and which will be recorded on a two dimensional detector. Figure 1.4 shows an illustration of techniques of integral field spectroscopy adapted from figure 1 of Allington-Smith & Content (1998).

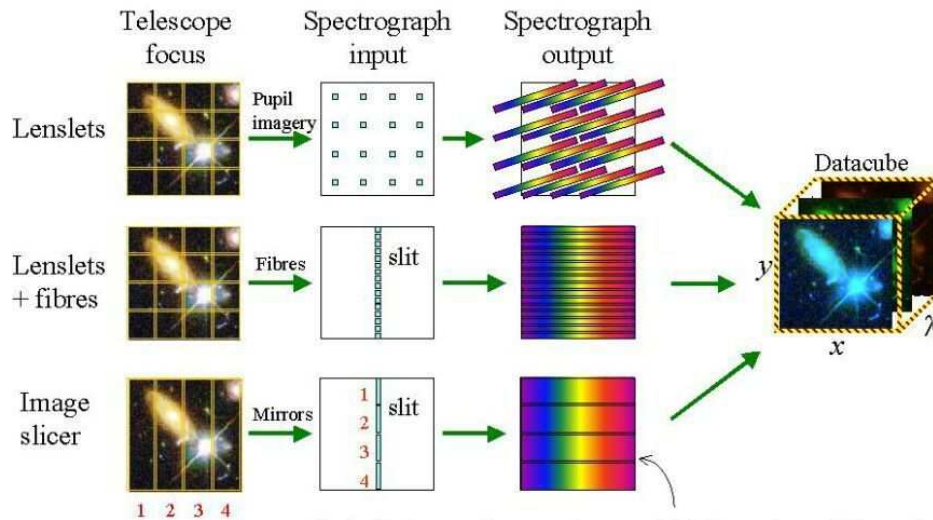


Figure 1.4: Techniques of integral field spectroscopy. *Source:* http://www.dur.ac.uk/images/cfai/ifu_tech_s.jpg

The main objective of IFS is to simultaneously produce a spectrum of every spatial element (referred to as "spaxel") in a field of view (FOV), with the spatial sampling and size of FOV determined by the instrument. The output for the data reduction process is a datacube with two-dimensional spatial information and spectral information as a third axis.

We describe briefly the three most important techniques to resample a telescope focal plane to be arranged onto the detector:

1. Lenslets

This technique uses an array of lenslets (small lenses) to sample a FOV. Light will be dispersed by a number of spectrographs with dispersion angle slightly tilted with respect to the lenslet array to avoid overlap between spectra of different lenslets. Advantages of this technique are a high throughput and continuous spatial coverage. Disadvantages are not optimal use of detector space, limited length of spectrum and complex data format. Integral field spectrographs using this technique are OASIS (**O**ptically **A**daptive **S**ystem for **I**maging **S**pectroscopy) on CFHT (**C**anada-**F**rance-**H**awaii **T**lescope) and WHT (**W**illiam **H**erschel **T**elescope), SAURON (**S**pectrographic **A**real **U**nit for **R**esearch on **O**ptical **N**ebulae) on WHT, and OSIRIS (**O**H-**S**uppressing **I**nfrared **I**ntegral **F**ield **S**pectrograph) on the Keck-I telescope.

2. Combination of lenslet and fibres

This technique uses fibres to rearrange light from each lenslet into "pseudo slits" which

will go to the spectrograph. Advantages using this technique are optimal use of detector space and longer range of spectral bandpass than simple lenslets. Disadvantages are possible light loss due to a limited fiber throughput. VIMOS (**V**isible imaging **M**ulti-**O**bject **S**pectrograph) on the VLT (**V**ery **L**arge **T**elescope)-Melipal, PMAS (**P**otsdam **M**ulti-**A**perture **S**pectrophotometer) on the Calar Alto 3.5m telescope, and GMOS (**G**emini **M**ulti-**O**bject **S**pectrographs) on the Gemini telescope use lenslets and optical fibres combined.

3. Image slicers

The last technique is restricted to infrared wavelengths and uses a mirror array to resample the image to form long pseudo slit. Advantage of this technique is that spatial information is preserved, and that this is feasible with a compact design. Technologically, it is difficult to produce image slicers due to the extreme requirement on the optical quality. SINFONI (the **S**pectrograph for **I**Ntegral **F**ield **O**bservations in the **N**ear **I**nfrared) and in the near future the Multi Unit Spectroscopic Explorer (MUSE) on the VLT use image slicer technique.

Integral field spectroscopy can provide spatial and spectral information simultaneously with substantially less observing time compared with long slit spectroscopy. Until now, most of the integral field spectroscopy observations were limited by the size of the FOV which can cause problems to observe a Point Spread Function (PSF) reference star at the same time with the quasar. A PSF reference is needed for proper quasar–galaxy deblending (section 3.3). Fortunately, the quasar nucleus itself can be used to characterize the PSF of our observation set up (section 3.3).

In the present day, larger IFS surveys are being carried out for example the Calar Alto Legacy Integral Field Area (CALIFA) survey⁵ (Sánchez et al. 2012) and the ATLAS^{3D} survey⁶ (Cappellari et al. 2011). Both aim at characterizing the local galaxy population in great detail with a total of 600 (CALIFA) and 260 (ATLAS3D) targeted galaxies.

1.4.3 SIGN OF DISTURBANCES IN IMAGING AND KINEMATICS

As described, major merging has been proposed as a main mechanism to explain AGN activity especially for AGN of high luminosity. Unfortunately, for each galaxy one can only observe a single snapshot in time and cannot follow the whole evolutionary process due to long time scales. This is also true for merger of galaxies which only present themselves to us in one single observed phase. A merger sequence could only be pieced together from numerous galaxies: a pair of close

⁵http://www.caha.es/CALIFA/public_html/

⁶<http://www-astro.physics.ox.ac.uk/atlas3d/>

galaxies, not yet coalesced, a system in the middle of merging process, and a system which is the end result after coalescence with remaining signs of gravitational interaction.

Qualitatively, a merger process will disturb the initial properties of a galaxy. The Merger can redistribute stellar and gas components hence alter a galaxy's morphology. Gravitational interaction can produce a number of characteristic signatures: tidal tails, stellar streams, bridges, rings, warped disks or shells.

In addition to changing morphological properties, gravitational interaction can also modify the kinematic structure of the galaxy. We will discuss in more detail in Chapter 4, but the main idea this thesis is to identify past gravitational interaction signatures in the kinematic properties of AGN host galaxies, in order to diagnose the past interaction and potentially link AGN activity with a merger trigger. Some signatures that can indicate kinematic disturbances and that we are looking for are:

We will analyze a sample of 19 AGN host galaxies at z , observed with the VLT-VIMOS IFU with respect to the incidence of such signatures and both compare to an analysis of imaging data, as well as interpret the joint incidence of distortion signatures regarding past major merging events.

2.1 SAMPLE

In this work, we use a data set which consists of 19 type 1 quasars with redshifts $z < 0.2$ selected from the Hamburg/ESO Survey (HES) for bright quasars by Wisotzki et al. (2000). The sample was drawn independent of the host galaxy morphologies and it is flux limited and statistically complete for intermediate-luminosity quasars in the southern hemisphere.

2.1.1 HAMBURG/ESO SURVEY QSO SAMPLE

HES (Wisotzki et al. 1996; Reimers et al. 1996) is a southern hemisphere wide angle survey using an objective prism combined with the ESO 1m Schmidt telescope. Supplemented with Kodak IIIa-J photographic plates and the 4° prism, they provide a wavelength range of $3200\text{\AA} - 5400\text{\AA}$ and 10\AA resolution at $H\gamma$. The ~ 380 plates (which cover an area of $\sim 10,000\text{ deg}^2$) have been scanned and reduced in Hamburg using the Hamburg PDS 1010G microdensitometer (Wisotzki et al. 1996).

The bright quasar catalog derived from HES is produced using multiple selection criteria from the digitized and reduced photographic plates as described by Wisotzki et al. (2000). Follow up observations using long slit spectroscopy were done using ESO 3.6 m, 2.2 m and 1.52 m telescopes during period 1990 – 1994. The quasar selection criteria which they used are morphology, color, and spectral features. Quasar will most likely have stellar/point source morphology on image and have a distinct Ultraviolet (UV) excess compared with the bulk of normal stars in inactive galaxies. From its spectrum, a quasar is an emission line object and the spectra of type 1 quasars show specifically prominent features from the active nucleus such as broad line emission.

Table 2.1 summarizes some main properties of the sample. Based on the local quasar type 1 luminosity function (e.g. Schulze et al. 2009; Koehler et al. 1997), our sample can be categorized as typical of intermediate luminosity quasars in the nearby universe. In Figure 2.1, we show that our data are complementary with studies of other samples (Dumas et al. 2007; Letawe et al. 2007) in terms of luminosity. It is thought that different AGN activity triggering mechanisms produce different mass accretion rates, and that this leads to different AGN luminosities. For low luminosity objects, secular processes are most likely to provide the physical mechanisms to ignite an AGN while for high luminosity objects major mergers are expected to provide the fuel required for triggering the AGN. The combination of our study with the two others illustrated in Figure 2.1 can provide a more comprehensive view of AGN triggering mechanisms as it fills the gap of intermediate luminosity AGN.

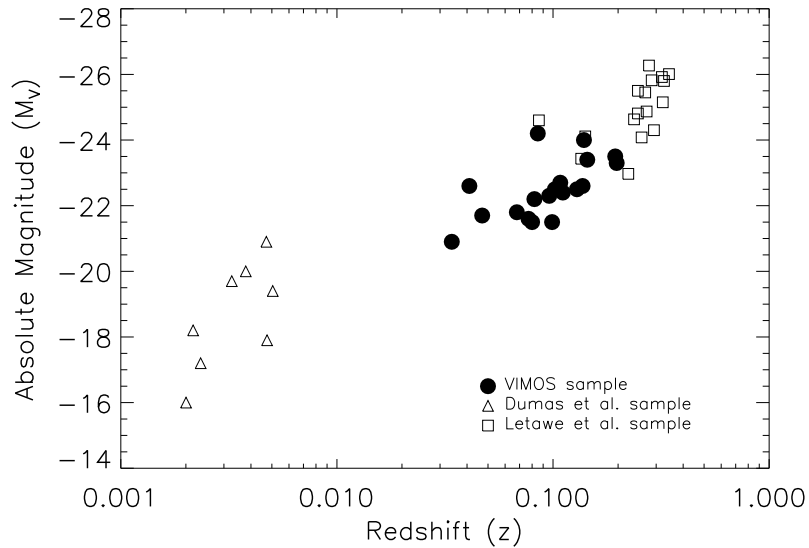


Figure 2.1: Plot of absolute magnitude vs redshifts for our sample (filled circles) and also for the two previous best studies of low redshift AGN: Seyfert galaxies (triangle) by Dumas et al. (2007) and long slit spectroscopy of $z \sim 0.3$ QSOs by Letawe et al. (2007).

Table 2.1: General properties of our VIMOS sample

Name	α (hh:mm:sss)	δ (dd:mm:ss.sss)	M_v (QSO) mag	Host morphology	Redshift	Scale (kpc/arcsec)	Optical Image
(1)	(2)	(3)	(4)	(5)	(6)	(7)	(8)
HE 0952–1552	09:54:29.58	–16:06:51.20	–23.3	Disk	0.108	2.177	DFOSC
HE 1019–1414	10:22:24.70	–14:28:58.00	–22.3	Disk	0.078	1.422	DFOSC
HE 1020–1022	10:22:32.82	–10:37:44.20	–23.9	Spheroid	0.197	3.158	WFPC2
HE 1029–1401	10:31:54.30	–14:16:51.00	–24.9	Spheroid	0.087	1.569	WFPC2
HE 1043–1346	10:46:17.00	–14:02:28.00	–22.5	Disk	0.069	1.276	ACS
HE 1110–1901	11:12:50.90	–19:26:23.00	–23.2	Spheroid	0.113	1.974	ACS
HE 1201–2409	12:03:37.70	–24:25:41.00	–23.5	Spheroid	0.138	2.349	DFOSC
HE 1228–1637	12:31:24.70	–16:53:51.00	–23.2	Spheroid	0.103	1.823	ACS
HE 1237–2252	12:40:28.30	–23:09:26.00	–23.0	Disk	0.096	1.735	DFOSC
HE 1239–2426	12:42:37.20	–24:42:40.00	–23.0	Disk	0.083	1.502	ACS
HE 1254–0934	12:56:56.90	–09:50:16.00	–24.7	Disk (Merger)	0.139	2.377	DFOSC
HE 1300–1325	13:03:22.23	–13:41:33.71	–22.5	Spheroid	0.047	0.899	DFOSC
HE 1310–1051	13:13:05.78	–11:07:42.40	–21.7	Disk	0.034	0.675	WFPC2
HE 1315–1028	13:18:36.20	–10:44:17.00	–22.1	Disk	0.099	1.775	DFOSC
HE 1335–0847	13:37:39.60	–09:02:28.00	–22.3	Spheroid	0.08	1.46	DFOSC
HE 1338–1423	13:41:12.90	–14:38:40.58	–23.3	Unclear (Disk)	0.042	0.810	DFOSC
HE 1405–1545	14:08:24.50	–15:59:29.00	–24.2	Disk (Merger)	0.194	3.116	DFOSC
HE 1416–1256	14:19:03.80	–13:10:44.00	–23.2	Spheroid	0.129	2.232	WFPC2
HE 1434–1600	14:36:49.60	–16:13:41.00	–24.1	Spheroid	0.144	2.451	ACS

Notes. (1) Name from original catalogue; (2) Right Ascension of the object¹; (3) Declination of the object¹; (4) Absolute magnitude of the quasar in V band; (5) Host galaxy morphology according to the analysis by Jahnke et al. (2004a); (6) Redshift¹; (7) Physical scale at the quasar’s redshift¹ (8) Source of the optical image. DFOSC is the *Danish Faint Object Spectrograph and Camera* mounted at the Danish 1.54-m telescope, WFPC2 is the *Wide Field Planetary Camera 2* on Hubble Space Telescope and ACS is the *Advanced Camera for Surveys* also on Hubble. Hubble data are obtained from the Hubble Legacy Archive (HLA)².

⁽¹⁾ Based on NASA/IPAC Extragalactic Database (NED)

⁽²⁾ <http://hla.stsci.edu>

2.1.2 A PREVIOUS MULTICOLOR STUDY OF THE SAMPLE

Our sample objects were also studied by Jahnke et al. (2004a) who carried out an analysis of the optical morphologies and the stellar population properties. This was based on multicolor photometric data and additionally for some objects, added long slit spectroscopic data from ground-based observations.

Based on the morphology analysis of the nucleus-subtracted host galaxies, Jahnke et al. (2004a) classified the objects into three main classes: bulge dominated, disk dominated and composite. The spectral energy distributions (SEDs) were derived from multicolor photometric observations in the optical and near-Infrared using the B, V, R, I, J, H, K filters, and the SEDs fitted with stellar population models. Jahnke et al. (2004a) found that the quasar host galaxies have bluer colors compared with a comparison sample of inactive galaxies. The age of the stellar populations for the best fitting SSPs is intermediate, ranging from 0.7 Gyr up to 6 Gyr, and they emphasized that the best fitting models contain intermediately young stellar populations (≤ 2 Gyr).

2.2 OBSERVATIONS

Observations of our sample were performed during ESO periods 72 and 83 in service mode and we list our objects and setup information for the observations in table 2.2. The technical details of the instrument and our observing strategy which will be useful for the upcoming analysis are described in the following section.

2.2.1 VIMOS DESCRIPTION

The Visible MultiObject Spectrograph (VIMOS, Le Fèvre et al. 2003) is an optical wide field imager and multi-object spectrograph mounted on the Nasmyth B focus of Unit telescope (UT) 3 Melipal of the ESO-VLT. Of the three different modes of VIMOS (imaging, multi-object spectroscopy (MOS) and integral field unit (IFU)) we use the VIMOS-IFU capability for this thesis. The VIMOS-IFU is a fiber-fed spectrograph consisting of 6400 fibers coupled with microlenses, with four 2048×4096 detectors, spectral resolution of $R \sim 220$ to 3100 and a $27'' \times 27''$ field of view for the high resolution setup with a $0.67''/\text{fibre}$ spatial sampling. More details of the VIMOS-IFU characteristics which we used are presented in table 2.3.

Table 2.2: Summary of the VIMOS-IFU Observations.

Name	Grism	Sampling ("/fibre)	Exposure time (s)	Airmass	Seeing
HE0952–1552	HR orange	0.67	2700	1.1	1.2
HE1019–1414	HR blue	0.67	2000	1.0	1.2
	HR orange	0.67	3000	1.1	1.3
HE1020–1022	HR orange	0.33	2000	1.1	1.0
	HR red	0.33	3000	1.2	1.3
HE1029–1401	HR blue	0.67	900	1.1	1.2
	HR orange	0.67	2700	1.2	1.3
HE1043–1346	HR blue	0.67	2700	1.2	1.3
	HR orange	0.67	2000	1.2	1.3
HE1110–1901	HR orange	0.67	2700	1.1	1.2
HE1201–2409	HR orange	0.33	1500	1.1	
	HR red	0.33	1000	1.0	
HE1228–1637	HR orange	0.67	3150	1.2 – 1.6	1.3
HE1237–2252	HR orange	0.67	2700	1.6 - 2.3	1.5
HE1239–2426	HR blue	0.67	900	1.5	1.4
	HR orange	0.67	2700	1.2 – 1.5	1.3
HE1254–0934	HR orange	0.67	2700	1.4 – 1.8	1.3
	HR red	0.67	2000	1.2	1.5
HE1300–1325	HR blue	0.67	2000	1.2 – 1.5	1.4
	HR orange	0.67	3000	1.2	1.3
HE1310–1051	HR blue	0.67	2000	1.2	1.6
	HR orange	0.67	3000	1.3 – 1.5	1.1
HE1315–1028	HR orange	0.67	3000	1.3 – 1.7	1.4
HE1335–0847	HR blue	0.33	2000	1.3 – 1.6	
HE1338–1423	HR blue	0.67	2000	1.1	1.3
	HR orange	0.67	3000	1.2 – 1.5	1.3
HE1405–1545	HR orange	0.67	2700	1.2 – 1.5	2.3
	HR red	0.67	900	1.2	1.5
HE1416–1256	HR orange	0.33	2000	1.3 – 1.5	1.2
	HR red	0.33	3000	1.1	1.2
HE1434–1600	HR orange	0.33	1500	1.2 – 1.5	
	HR red	0.33	1000	1.2	

Table 2.3: VIMOS-IFU characteristics with the high-resolution (HR) grism

Grism	Filter	Wavelength Coverage	Spectral Resolution	Dispersion ($\text{\AA}/\text{pixel}$)
HR blue	Free	4150–6200 \AA	2550	0.51
HR orange	GG435	5250–7400 \AA	2650	0.60
HR red	GG475	6450–8600 \AA	3100	0.60

Notes: For the high resolution grism setup, both field of view options ($13'' \times 13''$ and $27'' \times 27''$) are available using a spatial sampling (magnification) of $0''.33$ per fibre and $0''.67$ per fibre respectively.

2.2.2 OBSERVING STRATEGY

For our observations, the high-resolution gratings were used for all objects. The specific setup for each object was chosen in order that the wavelength range would cover the $H\beta$ and $H\alpha$ lines. The data were taken under conditions with seeing estimated between $0''.8$ and $1''.7$ and the instruments setup used different spatial sampling depending on an object's angular size. We chose the spatial sampling which would produce the optimum field of view to cover the object extension wherever possible.

The observing sequence was arranged as follows. After the initial telescope preset, for each target we obtained three dithered exposures for object IFU acquisition and another exposure for blank sky IFU acquisition. This was followed with night time screenflats and arc calibrations. Due to wrong coordinate input, two objects (HE 1201–2408 and HE 1434–1600) were not fully observed by our observations. HE 1020–2022 is also ignored in our subsequent for next analysis because of bad observing conditions for the spectrophotometry.

3.1 VIMOS DATA REDUCTION

This chapter will describe our approach to reduce VIMOS-IFU data from raw data frames to reduced science data cubes, which be used to study the quasar host galaxies. We also describe our complementary optical imaging data. On the last section of this chapter, we describe an important data preparation step to study type 1 quasar host galaxies, our quasar–host galaxy decomposition.

We retrieved the VIMOS data of our two programmes from the ESO archive and we used the data reduction on the R3D ¹ pipeline (Sánchez et al. 2006) complemented with customized Python scripts. There are other pipeline available for VIMOS-IFU data reduction besides R3D, for example the official ESO pipeline or the VIMOS Interactive Pipeline and Graphical Interface (VIPGI, Zanichelli et al. 2005) ² developed by the VIRMOS Consortium. The main goal of the ESO pipeline is quality assessment during the observation and VIPGI is a semiautomatic and interactive pipeline built on top of the automatic ESO pipeline as the main program.

While the VIMOS-IFU instrument offers the largest field of view for optical integral field spectroscopy with 8-m class telescopes, it also has some disadvantages which make data reduction more complicated compare to other IFUs. Examples are cross-talk phenomena, contamination from adjacent spectra caused by the high density of spectra on the detector resulting from 6400 tightly packed fibres and each spectrum being projected onto five detector pixels. Another complication is caused by mechanical flexures between four quadrants of the detector which affects spectral positions on the detector. With such complexities, an automatic pipeline will not be op-

¹<http://www.caha.es/sanchez/r3d/>

²<http://cosmos.iasf-milano.inaf.it/pandora/vipgi.html>

timal so a flexible pipeline is needed. We prefer to use R3D, a flexible data reduction package for field spectroscopy data, to carry out the main steps of the data reduction, which will be described on the following sections.

3.1.1 RAW DATA DESCRIPTION

We obtained raw data together with its respective calibration files. Figure 3.1 shows four examples of typical data which we use in this work.

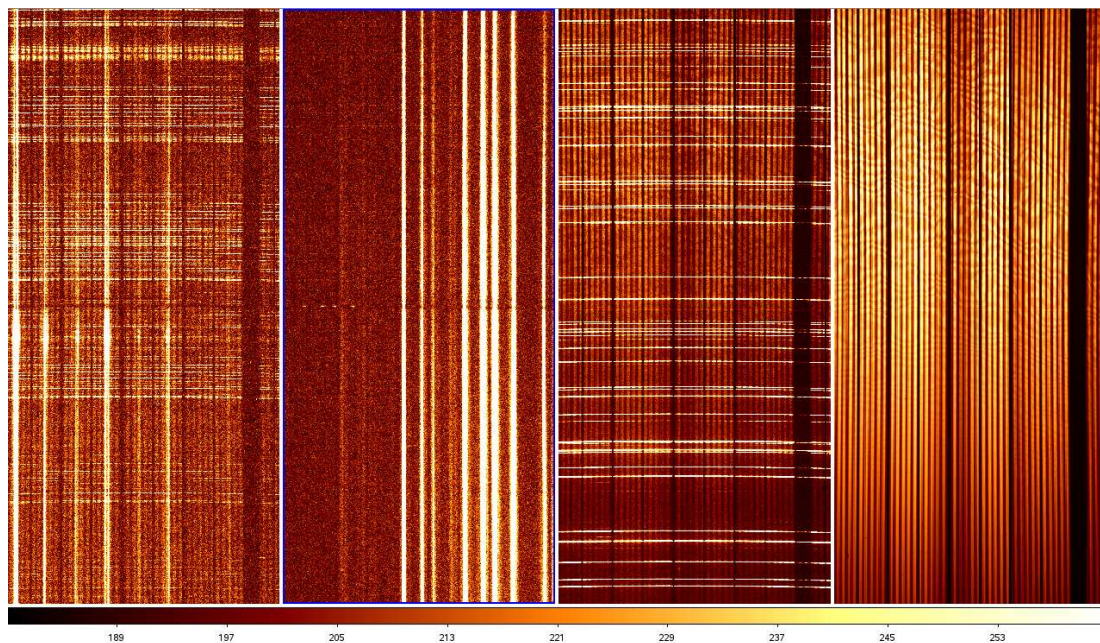


Figure 3.1: Example of raw data and calibration files from high resolution grism red (HR red) of quadrant 4. Each VIMOS CCD quadrant's dimension is 2048×4096 , vertical axis is dispersion axis with wavelength is redder toward the top. First panel: science frame. Second panel: spectrophotometric standard star frame. Third panel: arc lamps frame. Fourth panel: screen flat frame with significant fringing.

The following steps have been carried out in order to prepare the data for it can be use with R3D: bias subtraction of science and calibration frames and then cosmic ray hit removal from single image using *dcr*³ written by Wojtek Pych (Pych 2004). *dcr* is simple and faster and produces comparable results to other existing cosmic ray removal codes. An example of the cosmic ray hit removal showed in Fig. 3.2.

³<http://users.camk.edu.pl/pych/DCR/index.html>

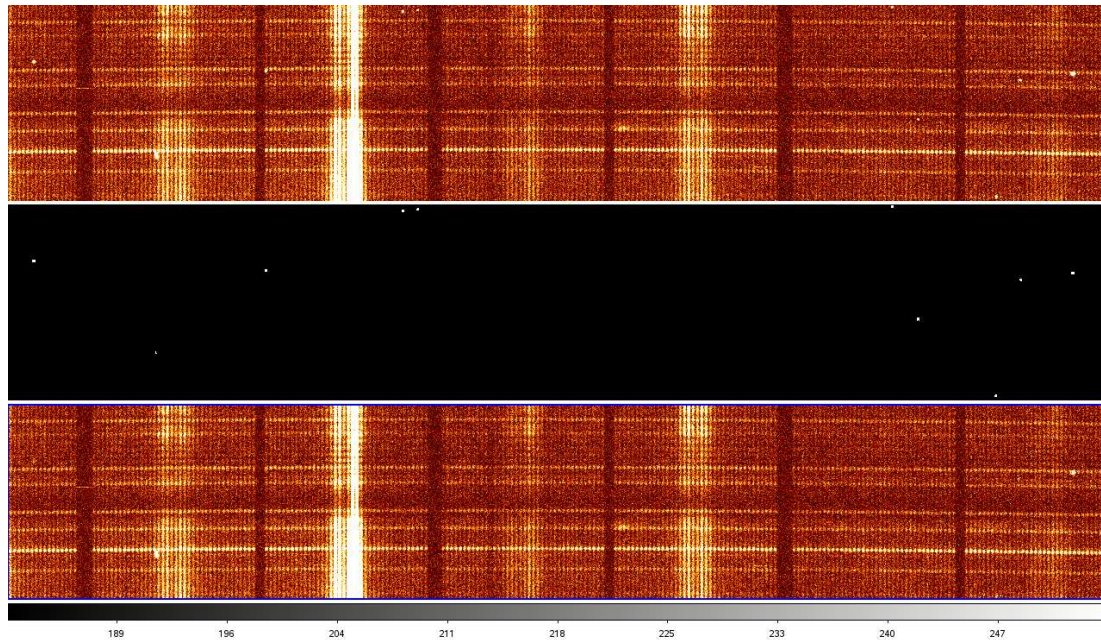


Figure 3.2: Example of cosmic ray removal from a single image using *dcr*. The top panel shows the original science frame. Due to the large size of detector, we show only a subfield to emphasize the result. The middle panel is the cosmic ray image constructed by the code and in the bottom panel is the cleaned science frame is shown.

3.1.2 SPECTRA TRACING

The first step with R3D to reduce VIMOS-IFU data is identify positions of the spectra on the detector as a function of wavelength. We use a high signal to noise ratio frame screen flat field to trace the peak intensities. Inside R3D the main process is a comparison of pixel's intensity with its neighboring pixels and finding peak criterium set by the user. In R3D we have to specify and adjust dispersion axis direction, minimum distant between neighboring spectra and a threshold to define peak intensity. Using R3D we can do visual inspection during the tracing process as shown in figure 3.3.

3.1.3 DISTORTION AND DISPERSION CORRECTIONS

After we achieved optimal peak identification and its position as function of wavelength measurement, we extract flux for each spectrum across the dispersion axis, by co-adding flux within an aperture and save it into a 2 dimensional image known as row stacked spectra (RSS). An

example of a part of a RSS image is shown in figure 3.4 and the dispersion axis is X axis. In a RSS frame each fibre spectrum now contained in a single row, as we can see from RSS image, the dispersion of light of the spectrograph is not homogeneous across the dispersion axis. This distortion is called the "C distortion", where the dispersion is larger in both edges compared to the center. To correct for this distortion, we choose one emission line from the RSS image and trace its location across dispersion in R3D, then shift all spectra to the same reference using a polynomial correction. We applied the same type of correction to the other lines to produce a distortion corrected RSS image as shown in right panel of Fig. 3.4. As the final steps for data reduction using R3D, we have to find the wavelength solution by transforming the distortion corrected image to a wavelength system using arc lamp frames.

3.1.4 BUILDING THE DATA CUBE (DAR CORRECTION)

We did conversion of the RSS to data cube using a Python script. The goal is to map the RSS image into the field of view of our observation for each wavelength. To do this, we need a position table provided by ESO, a table which relates the position of each fiber with its corresponding position in the sky. Due to the refractive characteristic of Earth's atmosphere we have to take into account the effect of Differential Atmospheric Refraction (DAR). The incoming light experiences refraction by Earth's atmosphere, which is wavelength dependent, hence the image position of the object will be different in the focal plane at different wavelengths. To correct for this, we shifted each image slice per wavelength to a common reference center position after we estimated the shift using a polynomial fit to the center coordinates and the reference center position. The shifting process was done using a sub-pixel resampling technique. In addition to the science data cube, we also produced a variance data cube by combining read-out noise from the detector and poisson noise from incoming photons and co-registered this cube astrometrically with the science cube..

3.1.5 SKY SUBTRACTION

During the observations in ESO period 83 we were taking blank sky IFU observations to be used to subtract sky contribution from the science frames. For period 72 we did not have blank sky images hence sky subtraction was done, using sky estimated from the science frames themselves in regions without object emission.

3.1.6 FLUX CALIBRATION

Last part of the data reduction is flux calibration using standard spectrophotometric star. The goal is to convert the count rate which detected and read by the detector into flux density. To do this we have to know the sensitivity function which takes into account atmosphere effect to the amount of photon from the celestial objects to the telescope and detector. We compare our quasar observation with standard star observations to calculate the sensitivity function for each pointing.

3.2 OPTICAL IMAGING

For this work, we also incorporate existing data, specifically optical imaging data. All of our objects were observed with DFOSC (Danish Faint Object Spectrograph and Camera) mounted on the Danish 1.54-m telescope and, as mentioned in table 1.1, we also use publicly available Hubble observations which were provided by the Hubble Legacy Archive (HLA) for 9 objects.

3.3 QUASAR – HOST GALAXY DECOMPOSITION

Recently, [Jahnke et al. \(2007\)](#) and [Letawe et al. \(2007\)](#) developed algorithms to decompose nucleus and host galaxies in on-nucleus long slit spectroscopic observation of AGN. [Jahnke et al. \(2007\)](#) used the spatial information of the long slit on PSF and host galaxy morphology to model the spatial component of nucleus and host galaxy spectra in 2D simultaneously and [Letawe et al. \(2007\)](#) used formal deconvolution of the spectra in 2D.

For our analysis, we use an iterative nucleus and host galaxies decomposition in integral field spectroscopic data developed and applied by [Jahnke et al. \(2004b\)](#), [Sánchez et al. \(2006\)](#), [Christensen et al. \(2006\)](#), and [Husemann et al. \(2008\)](#). From the quasar's position, we extracted a nucleus spectrum. The nuclear emission comes from an unresolved region within our observations and we assume that the nuclear spectrum, representing a point source object, is the same across the field of view, only with varying amplitude of the point spread function, created by Earth's atmosphere and our optical system configuration.

We defined spectral broad line and continuum regions for the nucleus spectrum and host galaxy spectra and use the ratio of broad line flux to rescale the nucleus spectrum to construct a nuclear template data cube, which is then subtracted from the original data cube, to get a host galaxy data cube. This steps is adequate if there are negligible contributions from the stellar component

of the host galaxy to the nucleus emission. Otherwise, we have to take into account contribution from the scattered stellar component of host galaxy which requires an iteration map. In this case we extracted a new nucleus spectrum from nucleus subtracted data cube (first iteration) and determine host galaxy contribution from its surrounding. The difference will be a new "cleaner" nucleus spectrum and we iterate these same steps to produce a subtracted data cube until the nucleus spectrum converges during iteration. we find that in this process, the nucleus spectrum is not changing after the third iteration. We illustrate how our QSO host galaxy decomposition works on figure 3.6. The nucleus-subtracted host galaxy spectra produced from this decomposition method will be used for next steps of analysis in this work and the results for the remaining objects other than HE 0952–252 will be presented in Appendix A.

We also present the flow chart of our quasar–host galaxy decomposition algorithm in Fig. 3.5 and we describe the main idea of our decomposition method with following mathematical approach:

1. First step, we use ideal approach where we assume that the flux of specific wavelength range of broad line emission line for each spaxel is only the nuclear spectrum of the same wavelength range modified by the scale factor.

$$F_{spaxel} = s \times F_{quasar} \quad (3.1)$$

$$s = \frac{F_{spaxel}}{F_{quasar}}, \quad (3.2)$$

where F_{spaxel} is the flux in the spaxel, F_{quasar} is flux from the nuclear spectrum within wavelength range of broad line emission and s is the scale factor for each spaxel. Two dimensional scale factor images produced from scale factor from every spaxels and it can also extend to data cube.

2. Second step, we assume that there is possibility that host galaxy spectrum contaminates the nuclear spectrum. We subtract host galaxy spectrum produced from spaxels surrounding the nuclear spaxel to get more cleaner nuclear spectrum.

$$F_{quasar}^{1st} = F_{quasar} - F_{host} \quad (3.3)$$

$$F_{spaxel} = s^{1st} \times F_{quasar}^{1st} \quad (3.4)$$

$$F_{spaxel} = s^{1st} \times (F_{quasar} - F_{host}) \quad (3.5)$$

$$s^{1st} = \frac{F_{spaxel}}{(F_{quasar} - F_{host})}. \quad (3.6)$$

F_{quasar}^{1st} is the new nuclear spectrum, F_{host} is the host galaxy spectrum and produced from and s^{1st} is scale factor resulted from this second step.

3. Third step, we repeat second step but using nucleus-subtracted data cube from the second step.

$$F_{quasar}^{2nd} = F_{quasar}^{1st} - F_{host}^{1st} \quad (3.7)$$

$$F_{spaxel} = s^{2nd} \times F_{quasar}^{2nd} \quad (3.8)$$

$$F_{spaxel} = s^{2nd} \times (F_{quasar}^{1st} - F_{host}^{1st}) \quad (3.9)$$

$$s^{2nd} = \frac{F_{spaxel}}{(F_{quasar}^{1st} - F_{host}^{1st})} \quad (3.10)$$

$$s^{2nd} = \frac{F_{spaxel}}{(F_{quasar} - F_{host} - F_{host}^{1st})} \quad (3.11)$$

$$(3.12)$$

4. Fourth step, the next iteration using nucleus-subtracted data cube from the third step.

$$F_{quasar}^{3rd} = F_{quasar}^{2nd} - F_{host}^{2nd} \quad (3.13)$$

$$F_{spaxel} = s^{3rd} \times F_{quasar}^{3rd} \quad (3.14)$$

$$F_{spaxel} = s^{3rd} \times (F_{quasar}^{2nd} - F_{host}^{2nd}) \quad (3.15)$$

$$s^{3rd} = \frac{F_{spaxel}}{(F_{quasar}^{2nd} - F_{host}^{2nd})} \quad (3.16)$$

$$s^{3rd} = \frac{F_{spaxel}}{(F_{quasar}^{1st} - F_{host}^{1st} - F_{host}^{2nd})} \quad (3.17)$$

$$s^{3rd} = \frac{F_{spaxel}}{(F_{quasar} - F_{host} - F_{host}^{1st} - F_{host}^{2nd})} \quad (3.18)$$

$$(3.19)$$

5. Fifth step. We repeat the same step using the latest nucleus-subtracted data cube until contribution of surrounding host galaxy spectrum is negligible hence the nuclear spectrum converges.

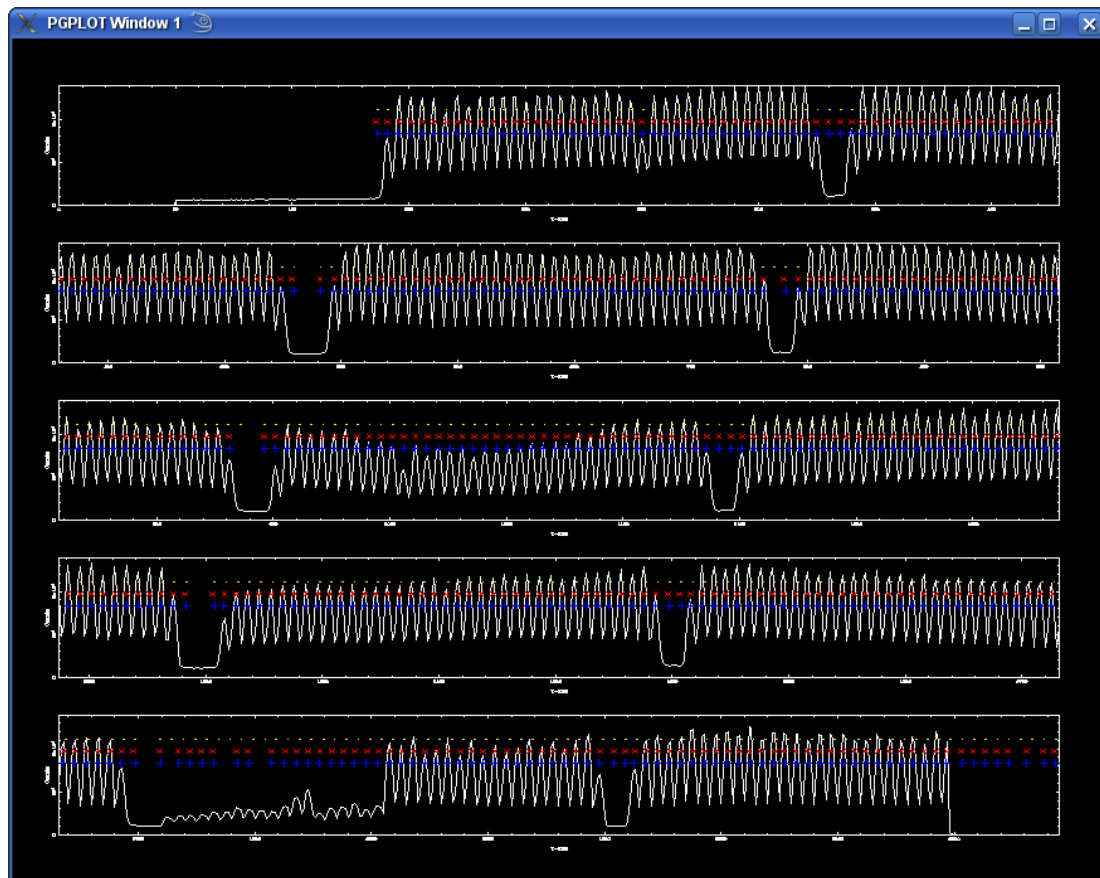


Figure 3.3: Example of visual inspection during identification of spectrum positions of VIMOS-IFU data using R3D. X axis is position across the chip and Y axis is intensity. We have to modify our input parameters in order that three points (yellow, red and blue) are correctly identifying peak positions. From this visual inspection plot we also can see low fibre transmission and even broken fibres in our data.

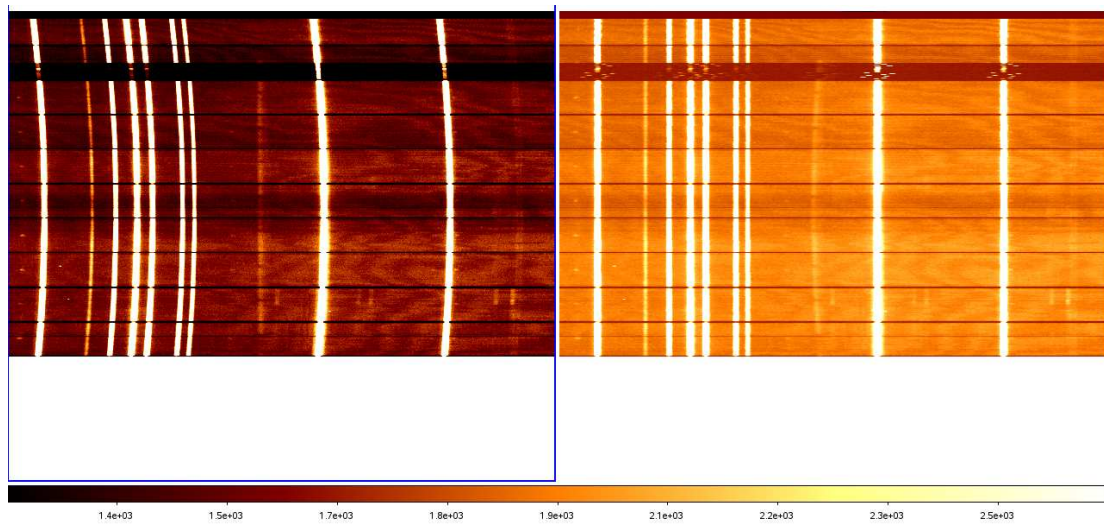


Figure 3.4: The left panel shows row stacked spectra (RSS) and right panel shows same part of the image after distortion correction applied. The dispersion axis is X-axis.

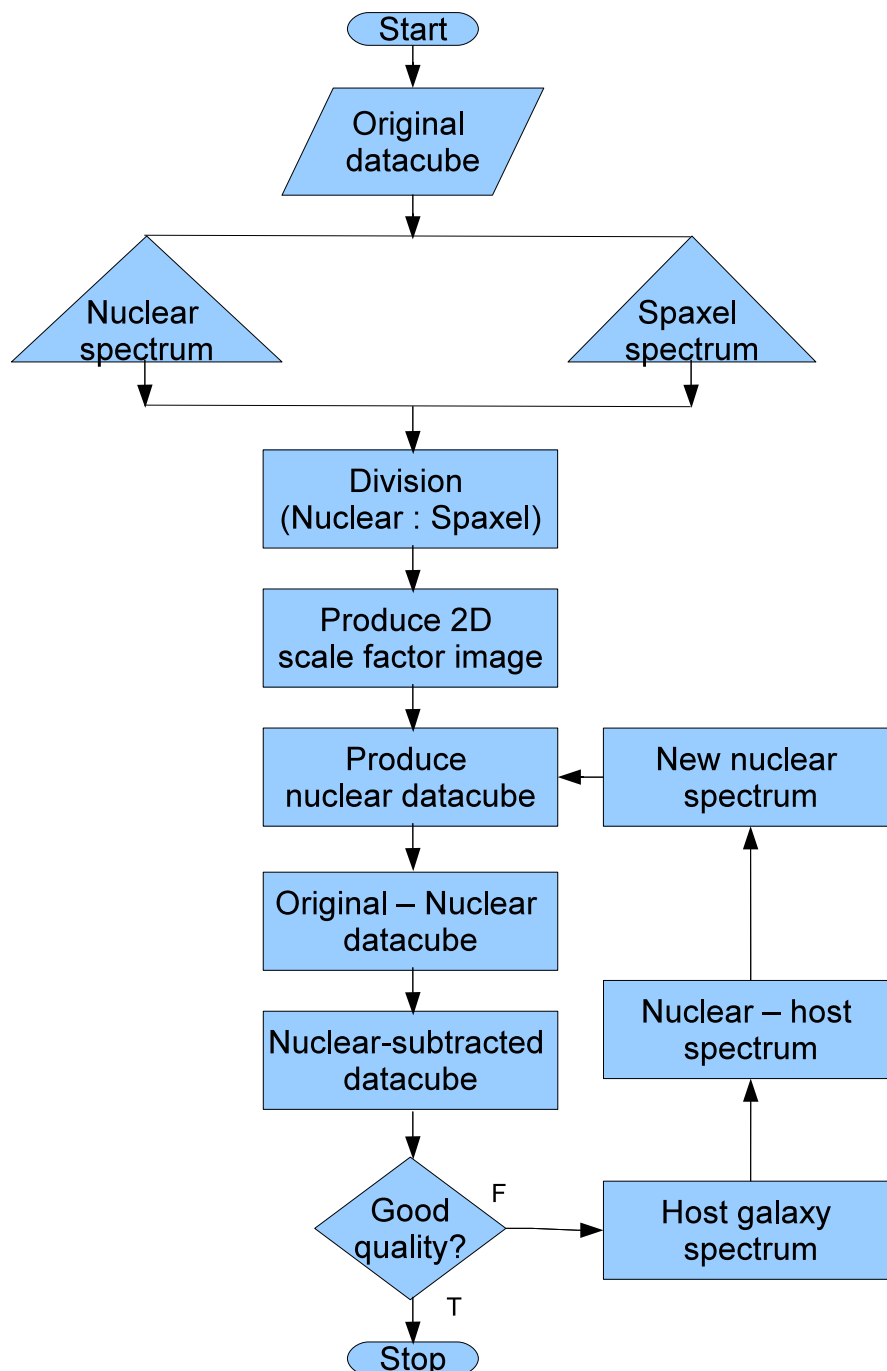


Figure 3.5: Algorithm of our quasar–host galaxy decomposition. We use spectra division technique added with host galaxy subtraction from quasar nuclear spectrum. More detail explanation provided in the text.

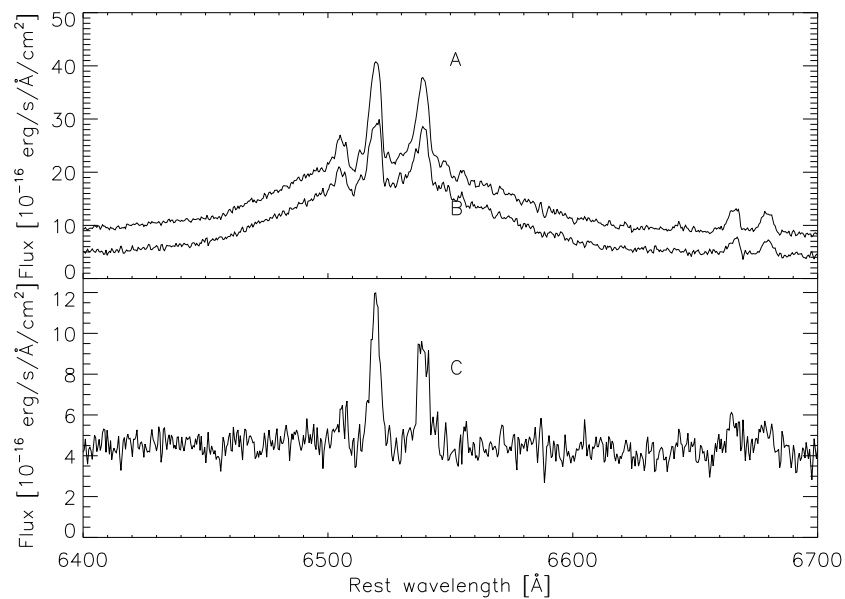
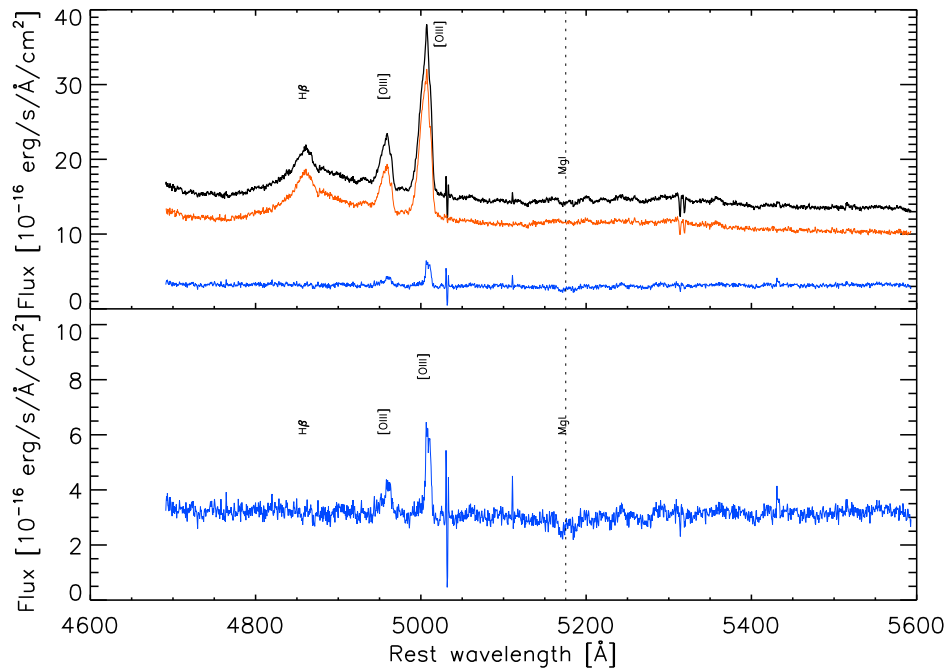
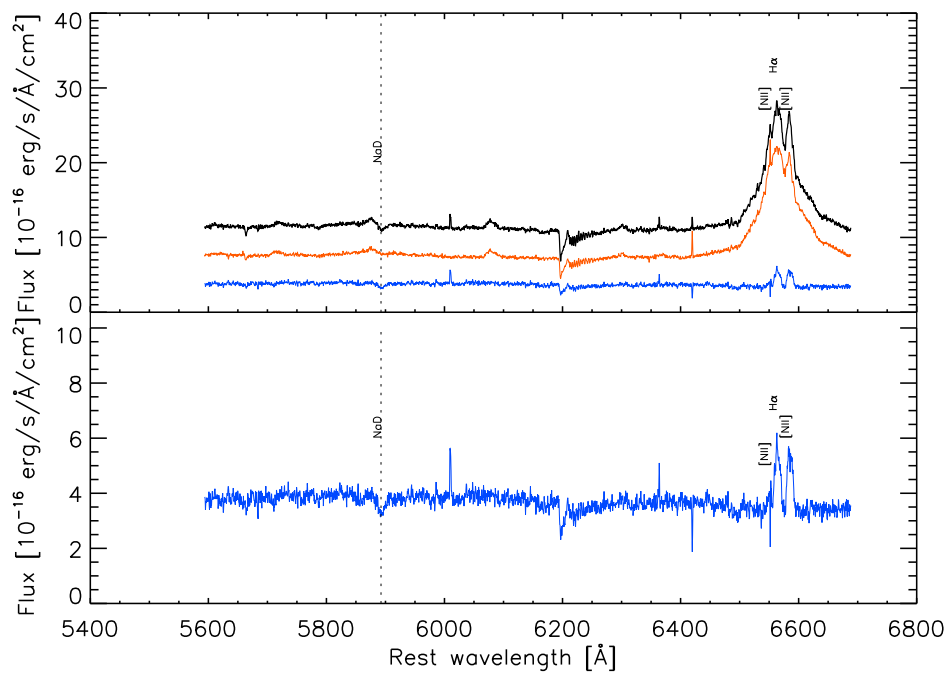


Figure 3.6: A demonstration of our quasar – host galaxy decomposition method for $H\alpha + [N II]$ complex using spectrum of HE 1237–2252. Top panel shows (A) spectrum from coadded region within $1''$ radius of the center, constructed from the original data cube and (B) spectrum of the nucleus template, constructed by multiplying the nucleus spectrum, extracted from the central spaxel, with a specific scale factor for each spaxels. The corresponding scale factor is computed by scaling the strength of the broad $H\alpha$ broad line in every spaxels with respect to the quasar’s spaxel. The bottom panel shows the host galaxy spectrum (C) from the same region as above after we subtracted nucleus template from original data cube. We can see from this figures that after nucleus subtraction, all broad line feature, produced by nucleus, are not present any more.



(a) Spectrum of HE0952–1552 shows $H\beta$ and [OIII] complex.



(b) Spectrum of HE0952–1552 shows $H\alpha$ + [N II] complex.

Figure 3.7: For further example we show quasar – host galaxy decomposition method for HE 0952–1552. Results for the remaining objects will be presented in the Appendix. (a) Spectrum with $H\beta$ and [OIII] complex. (b) spectrum with $H\alpha$ + [N II] complex. Black: original spectrum, red: scaled nucleus spectrum, blue: host galaxy spectrum without broad-line emission.

EXTRACTION OF PHYSICAL PARAMETERS

From the final nucleus subtracted data cubes produced by our quasar–host galaxy decomposition method, we continued with the next step, data analysis, which will be described in this chapter. Our main aim here is the extraction of physical parameters relevant to the science goals, mainly by emission line fitting to enable emission line kinematic analysis and an investigation of the physical conditions of the ionized gas and broad line modeling for black hole parameter measurement. The result will be presented in the two subsequent chapter 5 and 6.

4.1 EMISSION LINE FITTING

As mentioned before this study will improve over previous studies by its vast amount of spatial information for quasars at good signal to noise ratio. This enable us to measure in very much detailed and spatially resolved a number of diagnostic emission lines. From the wavelength range covered by by our observations, we have all lines from from $H\beta$ to $[SII]\lambda 6731$ available for each object. We modelled all prominent emission lines in this range using our IDL script with gaussian profiles to determine four line parameters centroid, width, flux, velocity dispersion. Our IDL script built mainly using IDL routines MPFIT, MPFITFUN and MPFITPEAK written by Craig Markwardt (Markwardt 2009)¹. For black hole parameters determination, we modelled $H\beta$ and $[OIII]\lambda\lambda 4959, 5007$ system of the nuclear template with multiple gaussians using an IDL fitting package called XGAUSSFIT².

For this thesis, our main objectives is to utilize the kinematic properties of the host galaxies based on emission line centroid which are not strongly affected by continuum determination.

¹<http://purl.com/net/mpfit>

²http://fuse.pha.jhu.edu/analysis/fuse_idl_tools.html

Hence our emission line fitting procedure does not take into account contribution of the stellar component to the continuum, we only fit the continuum with linear profile which can lead to mild overestimations of the measured line fluxes as emphasized by Sarzi et al. (2006).

4.1.1 VELOCITY FIELDS

For extracting line parameters, we fitted at each spaxel we fitted $H\beta$ and $[OIII]\lambda\lambda 4959, 5007$ simultaneously as one and $H\alpha$, $[NII]\lambda\lambda 6548, 6584$ as second system. We reduced the number of free parameters during the fitting process by fixing the flux ratio of $[OIII]\lambda\lambda 4959, 5007$ to its theoretical value of 2.98 and the flux ratio for $[NII]\lambda\lambda 6548, 6584$ to 2.96. We obtained spatial maps of emission line fluxes, centroid wavelength and full-width-at-half-maximum (FWHM) for each emission lines of the host galaxy. From this information we produced flux maps, relative velocity map and velocity dispersion maps, respectively, which we present in chapter 6. Uncertainties for our velocity maps are ~ 25 km/s for worst fit.

4.1.2 BPT DIAGRAM

Baldwin et al. (1981) and Veilleux & Osterbrock (1987) proposed a method to classify galaxies based on their excitation mechanisms using emission line intensity ratios of their spectra. This two dimensional classification well known as Baldwin, Phillips and Terlevich (hereafter BPT) diagram uses intensity ratios of lines which have to fulfill these requirements:

1. Clearly observable, which means it should be strong emission lines and not blended with other lines.
2. Emission lines with small wavelength separation to Balmer lines in order to minimize reddening effect.
3. High-ionization potential on one axis, low-ionization potential on the other, both normalized by Hydrogen lines.

The standard BPT diagram uses $[OIII]\lambda 5007 / H\beta$ versus $[NII]\lambda 6584 / H\alpha$, while other versions use $[OIII]\lambda 5007 / H\beta$ versus $[OI]\lambda 6300 / H\alpha$ or $[OIII]\lambda 5007 / H\beta$ versus $[SII]\lambda 6717 + \lambda 6731 / H\alpha$.

Baldwin et al. (1981) and Veilleux & Osterbrock (1987) used an empirical line in the diagnostic diagram to classify emission line galaxies into two main classes, star forming galaxies, which

have emission line ratios like HII region and AGN-ionized galaxies. Star forming galaxies are located in region lower than the demarcation line and to the left (BPT figure) Kewley et al. (2001) define a maximum limit for massive stars ionization in starburst galaxy by using photoionization models with MAPPINGS III code and stellar population models shown with dashed lines. Kauffmann et al. (2003) define the demarcation lines (solid line) empirically based on 55 757 objects from SDSS with signal to noise larger than 3 for four emission lines.

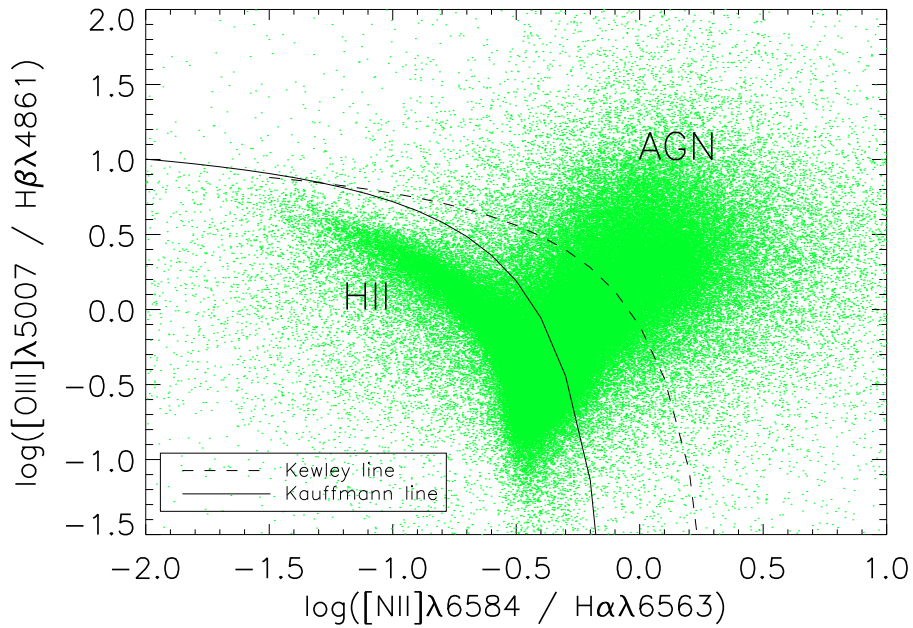


Figure 4.1: BPT diagram from SDSS data release 2.

From SDSS BPT diagram (Figure 4.1) we can see that Kewley demarcation line is a lower limit for the AGN number because we can see objects nearly below and to the left of Kewley line with different distribution compare with star forming galaxies sequence.

Based on excitation mechanisms we can distinguish between star forming galaxies and AGN where the latter can be classify into two sub groups, Seyferts and LINERS. Kewley line, modeled a maximum theoretical limit for massive stars ionization in the BPT diagram. Kauffmann determine delineation line empirically from SDSS galaxies.

We construct BPT diagrams, based on our wavelength coverage and signal to noise consideration we will use ratio of $[OIII]\lambda 5007 / H\beta 4861$ and $[NII]\lambda 6584 / H\alpha 6563$, hence the "classical" line set. investigate type of of the emission lines spectra. which can explained nature of the emission line objects. provides a guide to diagnose excitation mechanisms for ionized gas in astrophysical

objects in order to understand the physical condition of the ionized gas. For our BPT diagram construction, we will use co-added spectra and apply our emission line fitting routines to it hence we will not have spatial information until spaxel scale. Based on to construct the classical BPT diagram.

4.1.3 BLACK HOLE PARAMETER MEASUREMENTS

One of the key parameter for characterizing an AGN is the central black hole mass, which we require for inferring the accretion rate as the central diagnostic for the activity state of the AGN. We can estimate black hole masses for our quasar sample from the available single epoch spectral observation using the so called "Virial method" where we assume that the Broad Line Region (BLR) is virialized in Keplerian motion and the black hole mass can be estimated using the relation (Kelly & Bechtold 2007):

$$M_{BH} = \frac{fR_{BLR}\Delta V^2}{G}, \quad (4.1)$$

where M_{BH} is the black hole mass, f is a scale factor, R_{BLR} is the BLR size, ΔV is width of the broad line and G the gravitational constant. There are two options that one can use for determine the width of the broad line, the first is the FWHM and the other uses the line dispersion, i.e. second moment of the line profile. We decided for our measurements to use line dispersion, because it lower sensitive to the strong narrow line component and because it can be measured with smaller uncertainties than the FWHM (Peterson et al. (2004), Collin et al. (2006), Decarli et al. (2008)).

We construct the quasar spectrum from the nuclear template which we used for the quasar–host galaxy decomposition. We subtracted the best fit for the $H\beta$ (narrow component), $[OIII]\lambda\lambda 4959, 5007$ and $Fe II \lambda 4924$ and $\lambda 5018$ from the quasar spectrum and we determine the second moment from the resulted spectrum. The first moment of emission line profile $F(\lambda)$ is:

$$\lambda_0 = \frac{\int \lambda F(\lambda) d\lambda}{\int F(\lambda) d\lambda}. \quad (4.2)$$

The variance or mean square is the second moment of the profile,

$$\sigma_{line}^2 = \langle \lambda^2 \rangle - \lambda_0^2 = \left[\frac{\int \lambda^2 F(\lambda) d\lambda}{\int F(\lambda) d\lambda} \right] - \lambda_0^2. \quad (4.3)$$

the square root of σ_{line}^2 is the line dispersion, σ_{line} or root mean square width of the line.

We use scaling relation between continuum luminosity and BLR size which is readily available in the literature, in our case from [Bentz et al. \(2009\)](#),

$$\log(R_{BLR}) = -21.3 + 0.519\log(L_{5100}), \quad (4.4)$$

where L_{5100} is the continuum flux at 5100\AA . We use $f = 3.85$ for the case of taking the line dispersion as width following [Collin et al. \(2006\)](#).

In order to calculate the accretion rate as an Eddington ratio (ϵ)

$$\epsilon = \frac{L_{bol}}{L_{edd}}, \quad (4.5)$$

with $L_{edd} = 1.3 \times 10^{38}(M/M_{\odot})\text{erg s}^{-1}$, we require the Bolometric luminosity can be estimated from the continuum luminosity assuming bolometric correction factor (f_L), .

$$L_{bol} = f_L L_{5100}, \quad (4.6)$$

we choose $f_L = 9$ as suggested by [Kaspi et al. \(2000\)](#). An example of the fitting process shown in Figure 4.2 and results of this measurement are again presented in the next chapter 5.

4.2 KINEMATIC ANALYSIS

4.2.1 HARMONIC EXPANSION

After producing velocity fields (see section 4.1.1.) we made a qualitative assessment of their quality which we express as a quality flag for each velocity field. Flag "0" for bad and unusable velocity field for the purpose of kinematical analysis and Flag "1" for good velocity field which will be used for the next steps. Our decision is mainly based on the extension of the velocity fields, i.e. on S/N of the emission lines.

For analysis we use a harmonic expansion of the observed velocity fields and combine this with a visual inspection to determine whether an observed velocity field is regular or distorted. With this approach we attempt to provide a more qualitative and minimize the effect of subjectivity in this classification. Another advantage is that we can also immediately detect non-circular motions from the observed velocity field and then can be followed up with a more detailed analysis, e.g. of spiral or bar structure and inflow/outflow motions.

For the quantitative analysis of our observed velocity field, we follow the method by [van de Ven & Fathi \(2010\)](#) which is similar to the approach of [Krajnović et al. \(2006\)](#) who developed the Kinemetry.

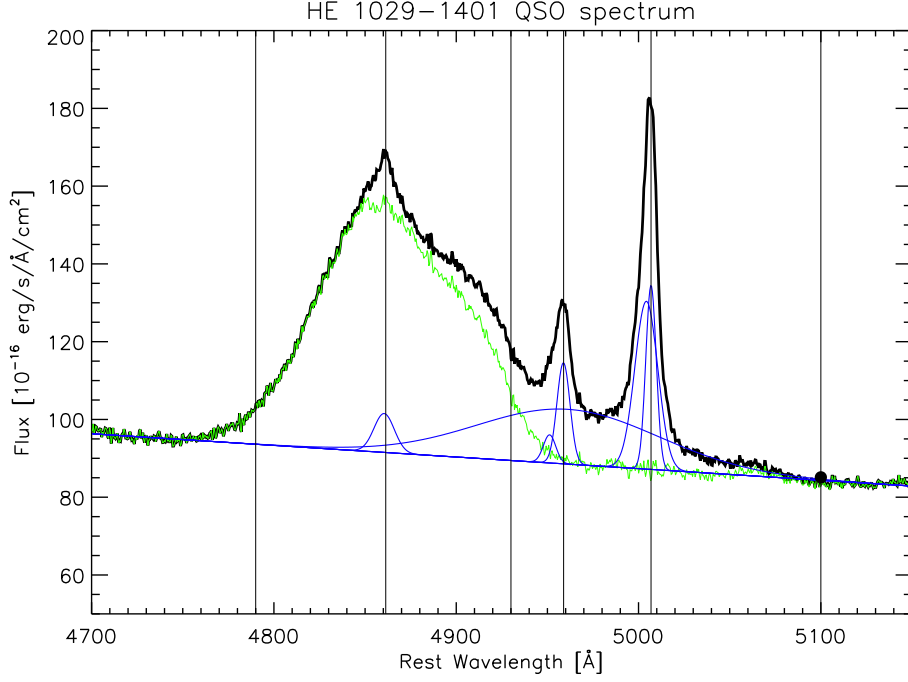


Figure 4.2: Example of fitting gaussians for black hole parameters determination from $H\beta$, $[OIII]\lambda\lambda 4959, 5007$ system of HE 1029–1401. Black line is nuclear spectrum, gaussian profiles in blue color are best fit for $H\beta$ narrow line components, $[OIII]\lambda\lambda 4959, 5007$ lines and possible Fe complex. The straight line is continuum determination and black filled circle shows the continuum flux at 5100\AA . We determine the line dispersion of $H\beta$ line from the green spectrum, produced from subtraction of gaussian profiles from the original nuclear spectrum.

In the Cartesian coordinates we can describe the velocity field as a set of ellipses with center (x_0, y_0) and angle (ψ_0) :

$$\begin{aligned} x' &= x'_0 + R \cos \psi \cos \psi_0 - q R \sin \psi \sin \psi_0, \\ y' &= y'_0 + R \cos \psi \sin \psi_0 + q R \sin \psi \cos \psi_0. \end{aligned} \quad (4.7)$$

If we choose that x' is oriented North and y' oriented West, the position angle of the kinematic major axis (Γ) is defined by $\Gamma = \psi_0 - \pi/2$, measured from North to East. We fit the circular model to the velocity field by adjusting the ellipse parameters, center (x_0, y_0) , position angle (Γ), inclination (i), and systemic velocity ((v_{sys})).

We can expand the velocity along each of the ellipses with a harmonic expansion:

$$V_{los} = c_0(R) + \sum_{m=1}^n c_m(R) \cos m\psi + s_m(R) \sin m\psi, \quad (4.8)$$

where V_{los} is the observed line-of-sight velocity, R is the semimajor axis, n is the order of the fit, ψ is the azimuthal angle, c_0 is the systematic velocity, and c_m and s_m are the coefficients of the harmonic expansion.

Using this approach, we assume that the gas disk is infinitely thin and we fit the harmonic expansion to the best fitted ellipses using a stepwise and iterative processes. Steps of our method to obtain the kinematics parameters are:

1. We determine concentric ellipses with the number of spaxels and signal to noise ratio as input constraints.
2. We perform a non-linear least squares fit of the circular rotation ($V_{los} = c_0 + c_1 \cos \psi \sin i$) along the ellipses and treat the ellipse parameters ($x_0, y_0, \Gamma, i, v_{sys}$) as free parameters for the first iteration. For the second iteration, we fit circular velocity with fix values for the center position, the position angle and systemic velocity. The best value for those three parameters are measured using the mean value over the radius calculated with bi-weight formalism. We fix all five parameters for the third iteration.
3. We fit harmonic expansion terms along the ellipses.

We present plots of harmonic expansion parameters in Chapter 6 which can be used to analyze the velocity field. The c_1 coefficient is related to circular motion so if there is only circular motion then all other coefficients will be zero, and non-zero if there are non-circular motions (e.g. inflows/outflows). The coefficient c_1 is related, as mentioned, with the rotation velocity curve, s_1 to the radial velocity component and c_2, s_2, c_3, c_3 are related to the non circular motion if existing in the residual. Every coefficient will be divided by $\sin i$ for inclination correction. Uncertainties for the harmonic expansion parameters are computed by means of Monte Carlo simulations. We repeat this same analysis on 500 randomized velocity fields, assuming that the velocity errors are gaussian. The resulting distributions provide the uncertainty for the parameters.

4.2.2 VELOCITY FIELD CLASSIFICATION SCHEME

Classifying galaxies, to learn about the underlying physics of the classification, is one of the main diagnostics of galaxy research. Various galaxy properties have already been used for such

classifications, for example structure or morphology, colors, stellar populations, star formation and also kinematics. Kinematic classification is only an emerging technique compared to other galaxy properties, due to the difficulties to produce two dimensional velocity field (before the current rapid development of integral field spectroscopy). Kinematic classification also can be carried out using one dimensional rotational curves, for example in studies by Rubin et al. (1999), Sofue et al. (1999), Swaters et al. (2009), or as in our case, using integral field spectroscopy data for example Flores et al. (2006), Emsellem et al. (2007) .

One of the central aim of this thesis is to study merger signatures as diagnosed from integral field spectroscopy data and compare them with optical morphology indicators. Stellar and gaseous components behave differently during the merger process, hence can show differences in their post merger distribution. As a comparison, we use morphological information from the study of Jahnke et al. (2004a) and for some objects where data is available using Hubble imaging data.

We divide our velocity fields into three main classes:

1. Regular: velocity field with regular rotation pattern and the axis for rotation being the same with major axis from optical image. The velocity dispersion map shows a clear peak near the center of the galaxy from the optical image and velocity field.
2. Distorted: deviation from a regular velocity field can be: asymmetrical features, peculiarities in the inner region or suddenly decreasing velocity in the outer part. The rotation axis is not the same with the major axis from optical image or the position of velocity dispersion peak has an offset from the center of the galaxies. Within this classification we also differentiate whether the distortion is mild or strong depending on the quantity of the distortion (e.g. offset of kinematic center and optical center, decreasing velocity at the outer part). We measure the kinematic center in the spatial XY plane of the image and we set a threshold for the distortion level. We decided to declare offsets which less than our spatial sampling (0.33" and 0.67") to be considered as mild distortions.
3. Unclear: velocity field with not so much structure, the signal for few emission lines being rather faint, we previously assigned a "bad" flag for this velocity field.

Using this main idea we construct a quantitative classification scheme using measurable parameters for our velocity fields and we use it for decision matrix to classify our velocity fields into those three main classes.

RESULTS: BLACK HOLE PARAMETERS AND PHYSICAL CONDITIONS OF THE IONIZED GAS

In this and next chapter 6 we will present the results of the analysis described in the previous chapter 4. We divide the results into information derived from emission line strengths (chapter 5) and kinematic properties (chapter 6).

For these results we can fully exploit our integral field spectroscopy data, allowing us to truly analyze the spatially resolved physical conditions, e.g. of the ionized gas over the full extent of a galaxy, as a difference to e.g. SDSS, which only covers the central 3''

5.1 BLACK HOLE PARAMETERS

Using the broad line fitting procedure for the $H\beta$ system which we described in chapter 4, we determine black hole parameters as a baseline to characterize the mass scale of the galaxies in our analysis. We summarize the derived black hole parameters (line dispersion, bolometric luminosity, mass and Eddington ratio) of our quasars in table 5.1.

5.2 BPT DIAGRAMS

By tracing the physical condition of the ionized gas through its emission line ratios we can investigate the dominating photoionization source. Using the BPT diagram we can distinguish whether the ionized gas is ionized by hot young massive stars in HII regions, shocks, or an AGN. In figures 5.1 - 5.12 we show BPT diagrams of extended emission line regions for quasar host

Table 5.1: Black hole parameters.

Name	H β line dispersion (km/s)	Continuum luminosity at 5100 Å (erg/s)	Log Bolometric luminosity	Log BH mass	Eddington ratio
HE0952-1552	2862	2.88×10^{40}	45.12	8.47	0.04
HE1019-1414	1612	7.10×10^{39}	44.51	7.65	0.06
HE1020-1022 ¹	-	-	-	-	-
HE1029-1401	2500	1.56×10^{41}	45.85	8.73	0.11
HE1043-1346	1791	7.56×10^{39}	44.54	7.76	0.05
HE1110-1910	2145	2.98×10^{40}	45.14	8.22	0.06
HE1201-2409 ²	-	-	-	-	-
HE1228-1637	1479	1.74×10^{40}	44.90	7.78	0.10
HE1237-2252	2507	1.40×10^{40}	44.81	8.19	0.03
HE1239-2426	1435	1.46×10^{40}	44.83	7.72	0.10
HE1254-0934	2674	1.38×10^{41}	45.80	8.76	0.09
HE1300-1325	2321	6.91×10^{39}	44.50	7.96	0.03
HE1310-1051	1790	4.25×10^{39}	44.29	7.63	0.04
HE1315-1028	1970	7.87×10^{39}	44.56	7.85	0.04
HE1335-0847	1092	6.76×10^{39}	44.49	7.30	0.12
HE1338-1423	1300	1.18×10^{40}	44.73	7.58	0.11
HE1405-1545	1445	5.53×10^{40}	45.40	8.02	0.19
HE1416-1256	2225	2.68×10^{40}	45.09	8.23	0.06
HE1434-1600 ²	-	-	-	-	-

Notes: 1 We cannot determine black hole parameters for HE 1020–1022 because bad spectrophotometry condition during the observation. 2 We cannot determine black hole parameters for HE 1201–2409 and HE 1434–1600 due to bad positioning during the observations hence we cannot cover the quasar extension optimally.

galaxies in our sample. We identified for each object distinct knots/regions of emission in $H\beta$ and $H\alpha$ flux maps and show the line ratios for these regions. At this moment we only able to show BPT diagram for 12 objects, the reason where we cannot present for all objects for example due to bad spectrophotometry, low signal (either for $H\beta$ and $H\alpha$ system or only one) so we cannot construct the BPT diagram for those objects.

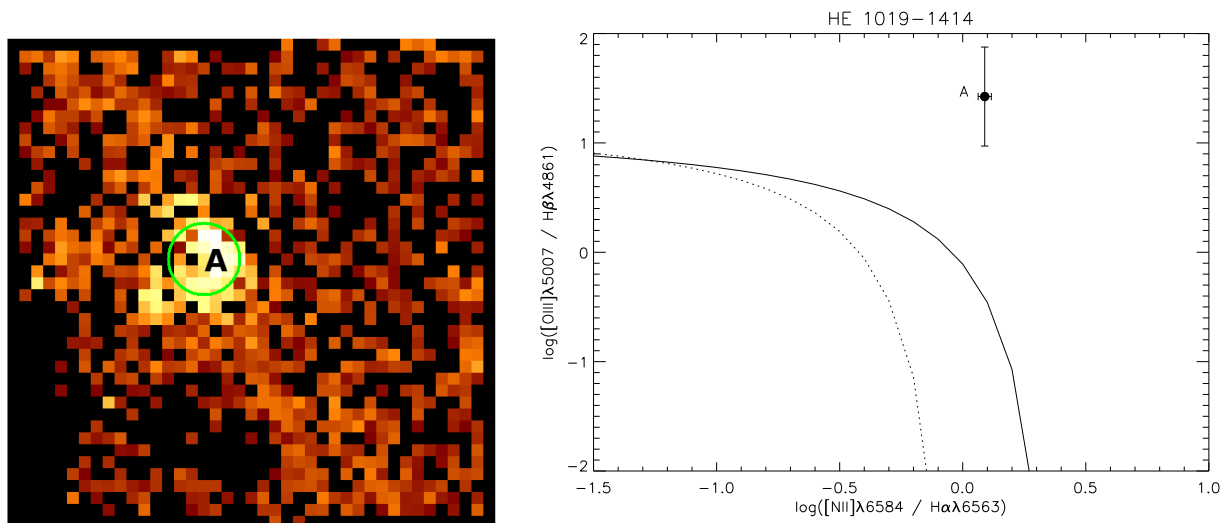


Figure 5.1: Ionization state of HE 1019–1414. **Left:** flux map in $H\beta$ and regions where spectra were coadded before applying our emission line fitting procedure to extract line fluxes to construct the BPT diagram. **Right:** The BPT diagram of the region to the left. The solid line is demarcation line to distinguish between AGN and star forming galaxies from Kewley et al. (2001) and dotted line based on empirical data from the SDSS (Kauffmann et al. 2003). Region A contains the AGN flux which also ionizes the "complete region".

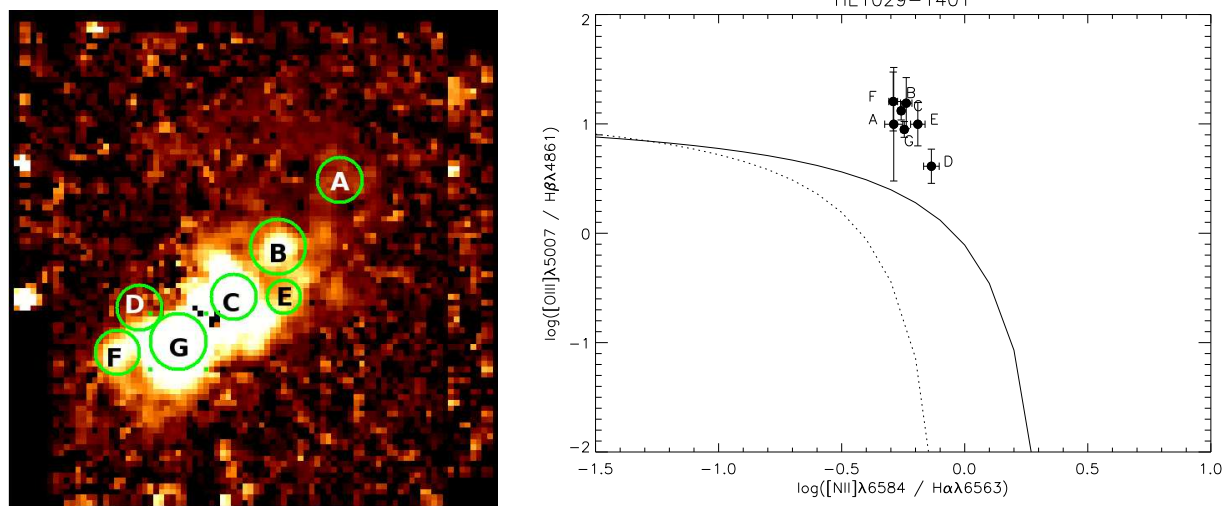


Figure 5.2: Ionization state of HE 1029–1401, for explanation see Fig. 5.1. The ionized gas of this elliptical galaxy is ionized by AGN in the center but we still cannot rule out contribution from young and hot stars.

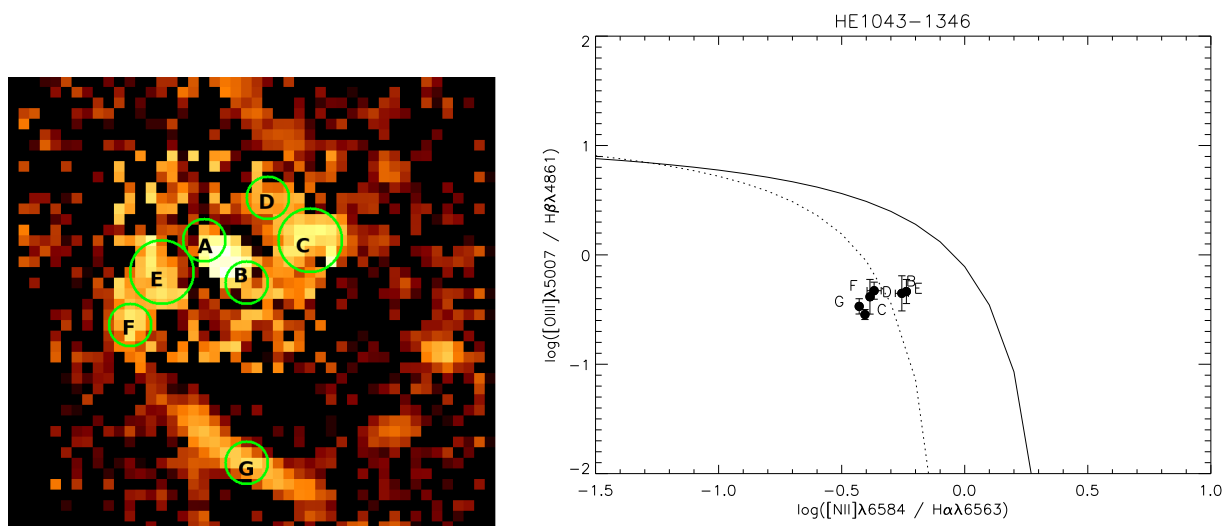


Figure 5.3: Ionization state of HE 1043–1346, for explanation see Fig. 5.1. For this galaxy all regions are dominated by radiation from star formation.

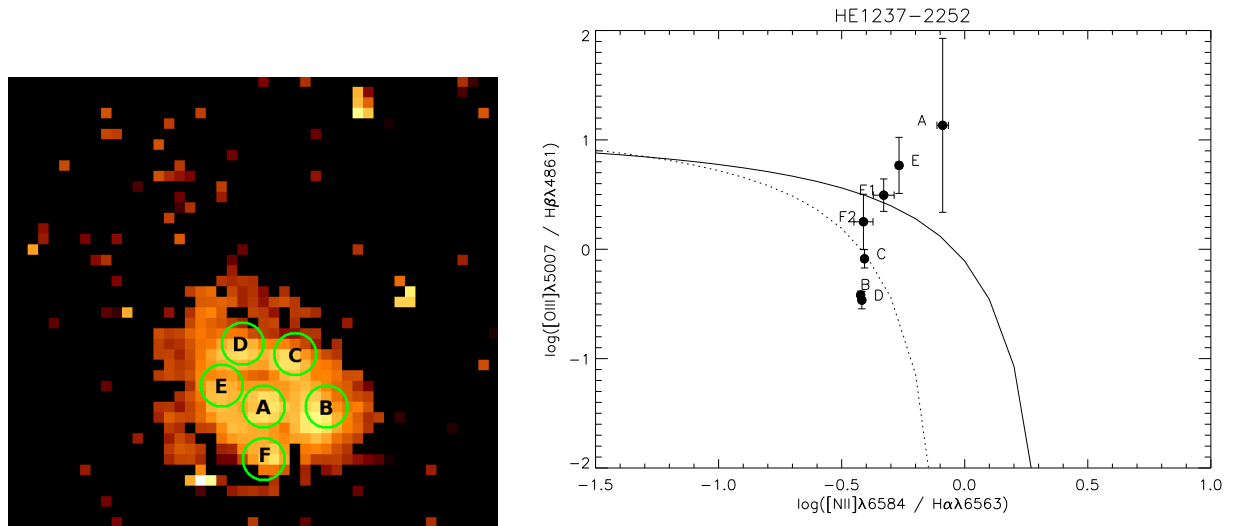


Figure 5.4: Ionization state of HE 1237–2252, for explanation see Fig. 5.1. Here the ionization sources for the extended emission lines regions are a mix of the AGN (in the center, region A) and some parts of its surrounding, as well as star formation.

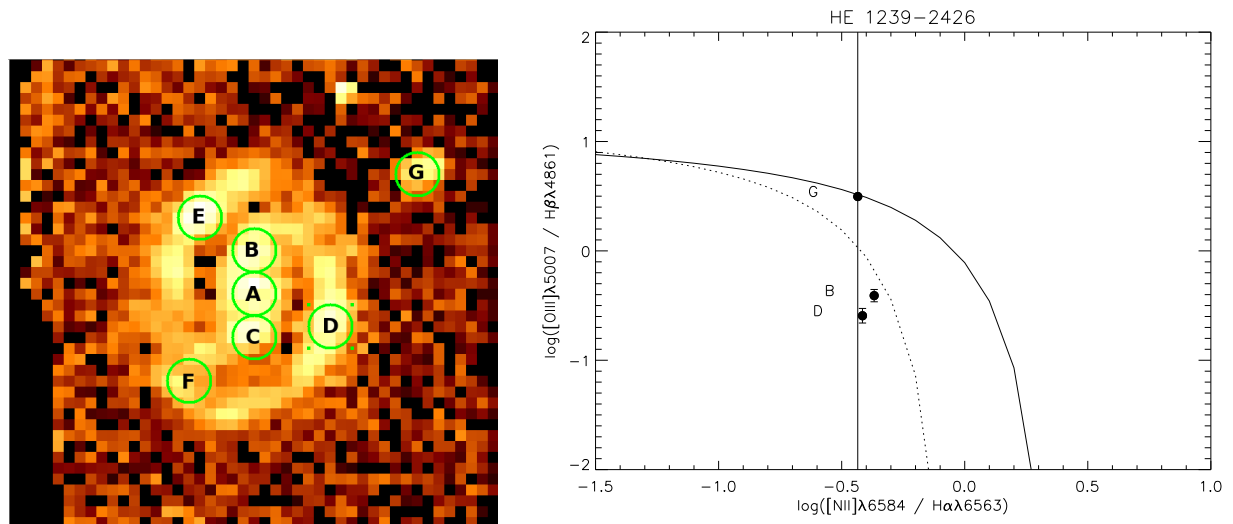


Figure 5.5: Ionization state of HE 1239–2426, for explanation see Fig. 5.1. Here the ionization sources for the extended emission lines regions are a mix of the AGN as well as star formation.

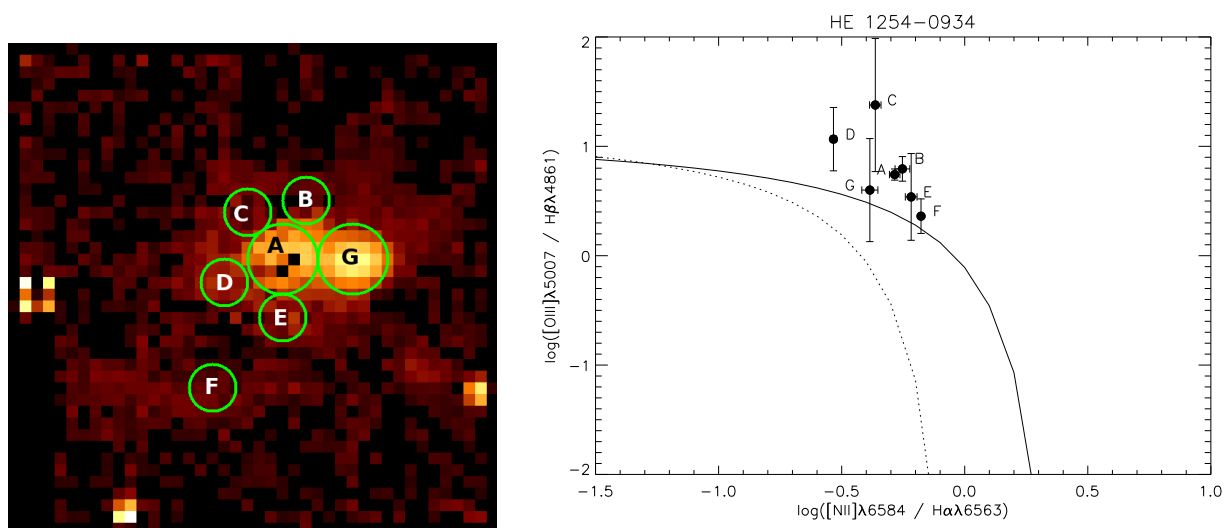


Figure 5.6: Ionization state of HE 1254–0934, for explanation see Fig. 5.1. Here the ionization sources for the extended emission lines regions are the AGN including at the outer region (region F).

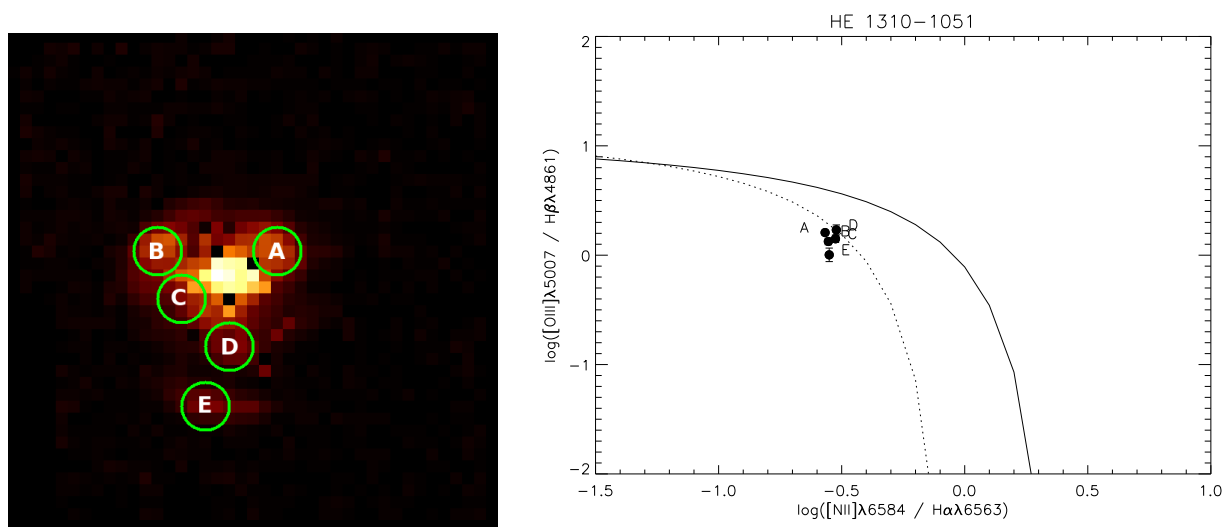


Figure 5.7: Ionization state of HE 1310–1051, for explanation see Fig. 5.1. Here the ionization sources for the extended emission lines regions are the star formation and possible AGN in the center part.

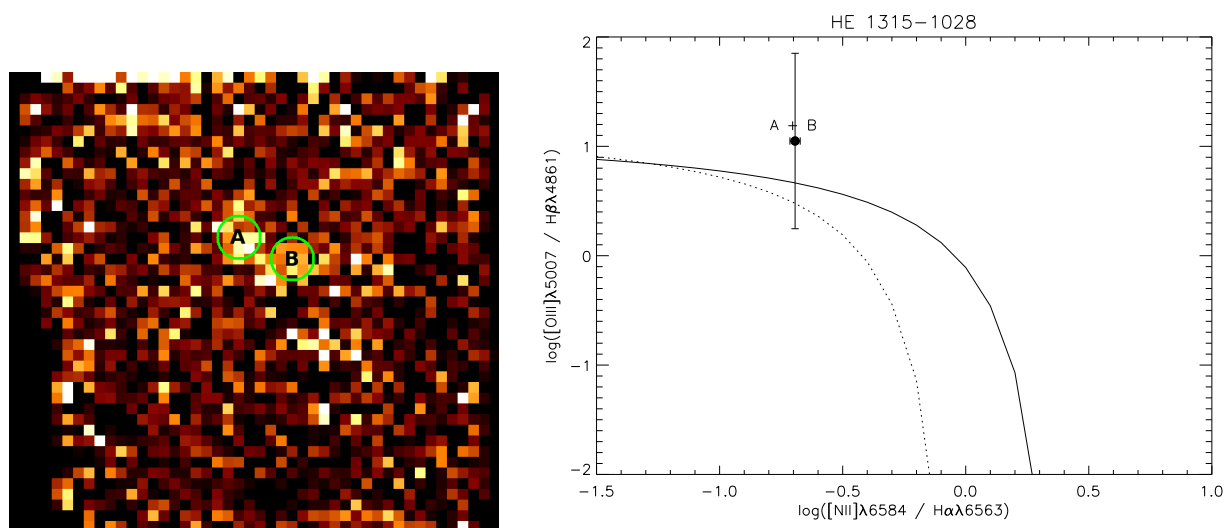


Figure 5.8: Ionization state of HE 1315–1028, for explanation see Fig. 5.1. Here the ionization sources for the extended emission lines regions are the AGN based on combined flux from region A and B.

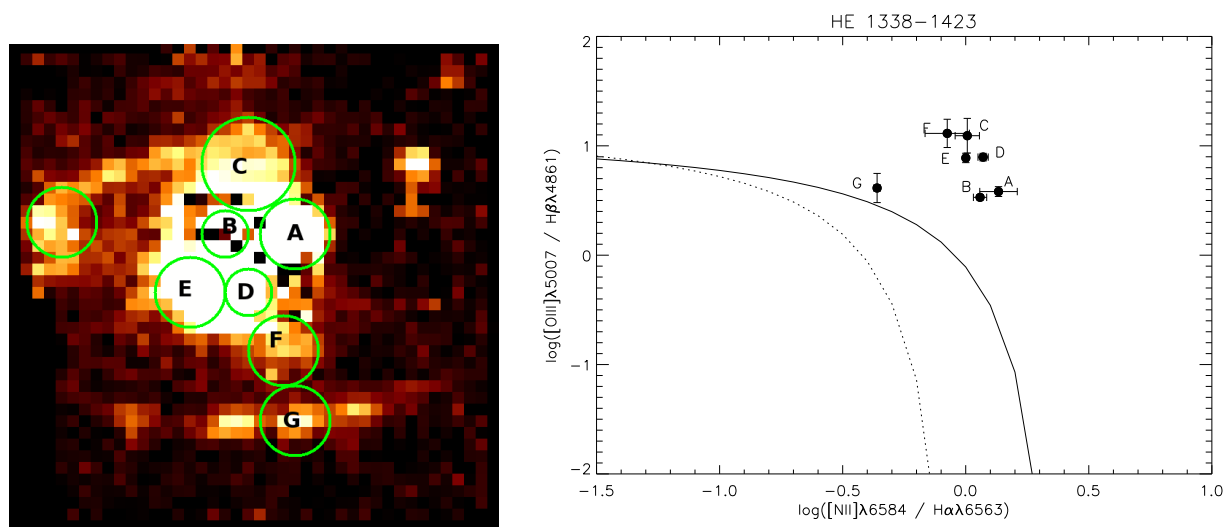


Figure 5.9: Ionization state of HE 1338–1423, for explanation see Fig. 5.1. Here the ionization sources for the extended emission lines regions are the AGN for every region shown in the left figure.

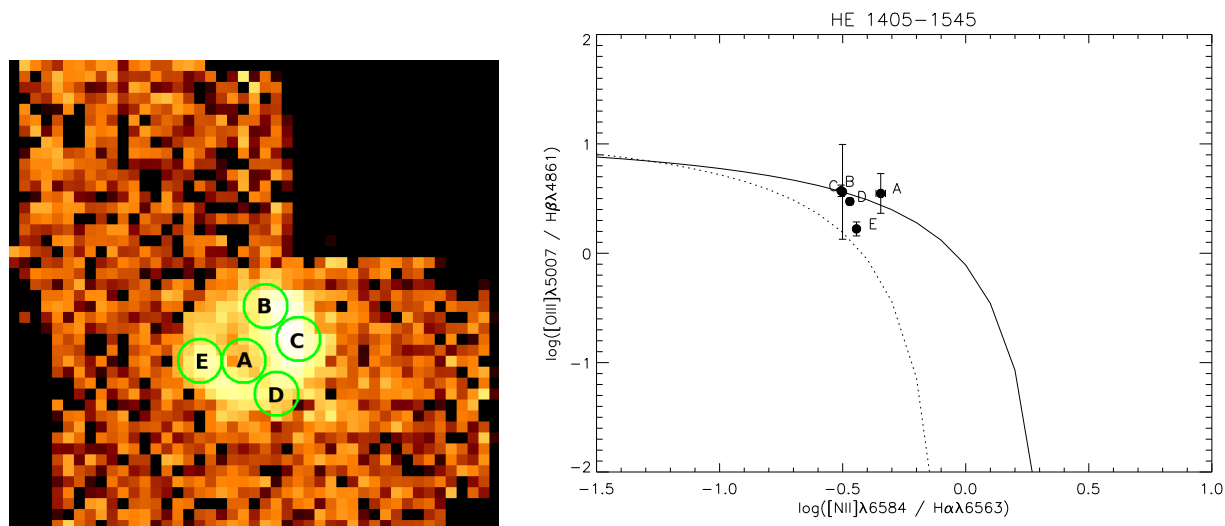


Figure 5.10: Ionization state of HE 1405–1545, for explanation see Fig. 5.1. Here the ionization sources for the extended emission lines regions are mixed between the AGN surrounding the center of this system and star formation in one region (E) far away from the center.

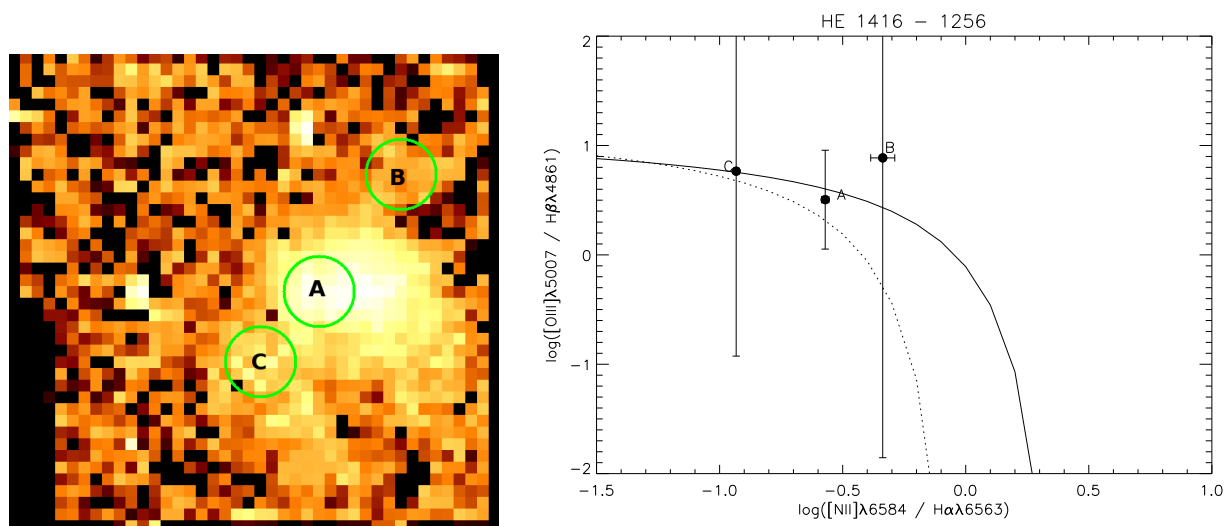


Figure 5.11: Ionization state of HE 1416–1256, for explanation see Fig. 5.1. Here the ionization sources for the extended emission lines regions are mixed between the AGN and star formation.

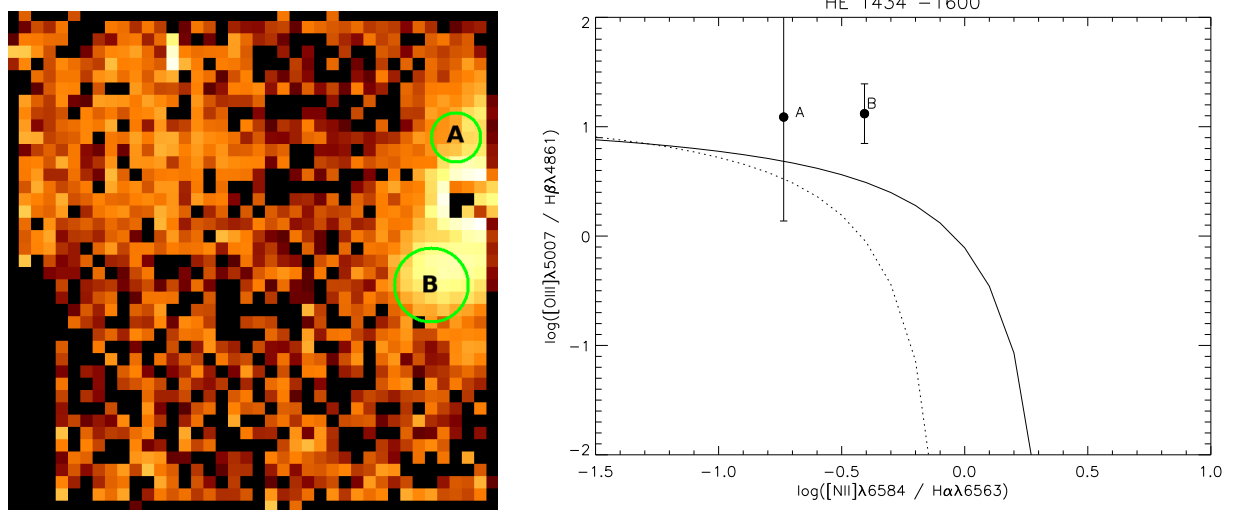


Figure 5.12: Ionization state of HE 1434–1600, for explanation see Fig. 5.1. Here the ionization sources for the extended emission lines regions are the AGN.

RESULTS: KINEMATICS PROPERTIES OF QUASAR HOST GALAXIES

The central analysis and diagnostic of this work is the interpretation of the kinematic properties of the quasar host galaxies in our sample. We put specific emphasis on the presence of mild or strong distortions, as we summarize in section 6.2. Before this, we present the results of the individual kinematical analysis for our sample objects.

6.1 OPTICAL IMAGES AND VELOCITY FIELDS

In the following, we present our emission lines gas velocity fields and velocity dispersion maps, as well as circular velocity and harmonic decomposition models as described in section 4.2. Optical images are also shown as reference. For each object we highlight key properties and features. We summarize information on offset of the kinematic models in table 6.1. in this section.

6.1.1 HE0952 – 1552

In general, the velocity map (Figure 6.1c) shows symmetric rotation structure except for the region with two velocity components at $2''$ to the north of the image center. We categorized this as "mildly disorted" in Table 6.2.

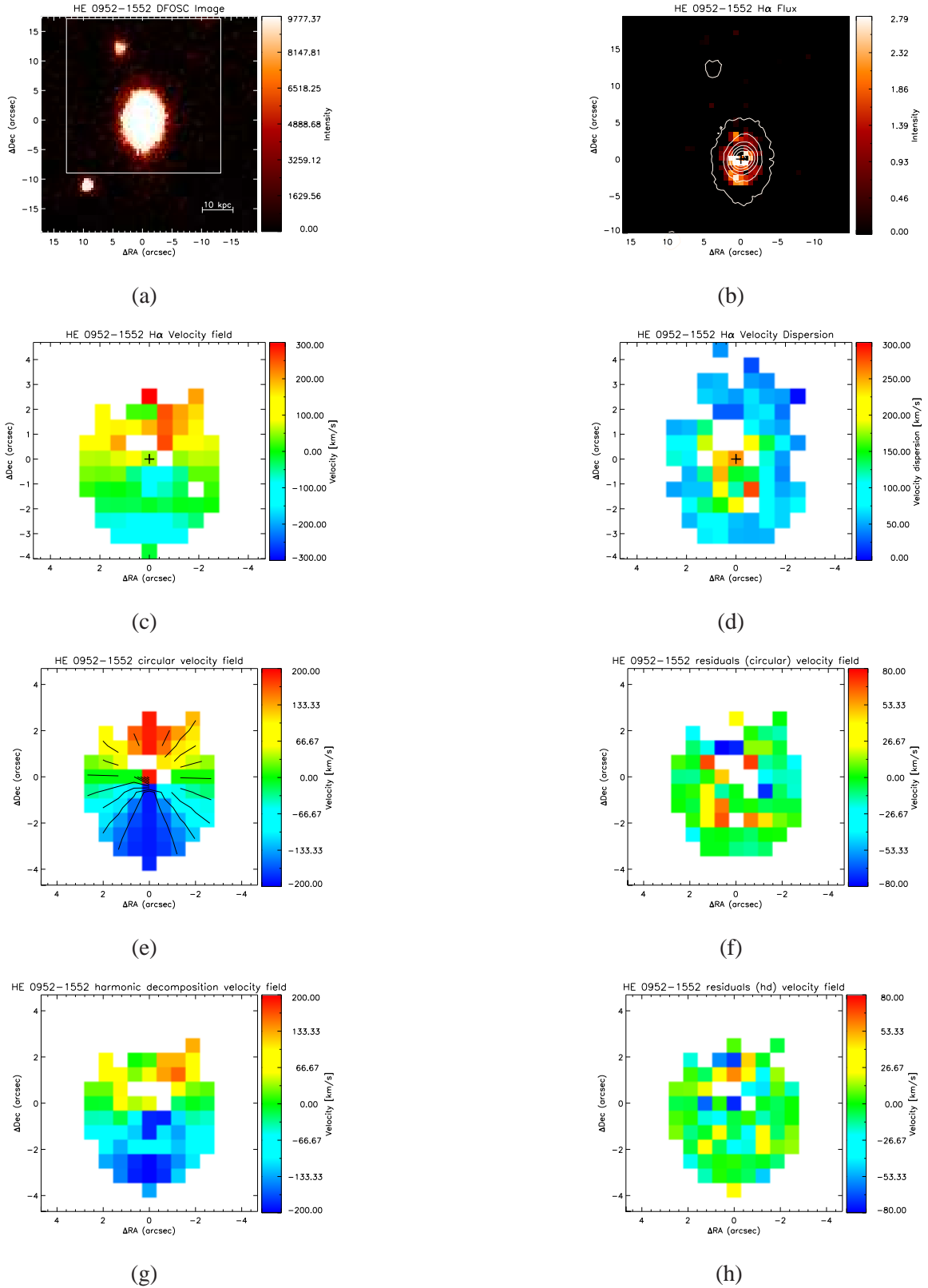


Figure 6.1: Kinematical analysis for HE 0952-1552. Shown are (a) optical broad-band image, (b) H α flux map from VIMOS, (c) H α velocity field, (d) H α velocity dispersion map, (e) best circular velocity model and (f) residuals after subtracting the observed velocity field with circular velocity model, (g) full harmonic decomposition velocity model and (h) residuals after subtracting the observed velocity field with harmonic decomposition velocity model. North is up, East is left.

6.1.2 HE1019 – 1414

A disk galaxy with a clear tidal tail feature to the North and a companion within the tidal tail. Unfortunately, the data is not good enough to trace the tidal tail on our maps. The velocity field shows ordered rotation in the main body of the host galaxy. We see some mild distortions in the velocity field.

6.1.3 HE1020 – 1022

Data for this host galaxy were insufficient for kinematical analysis. We omit this object from further analysis after the quasar–host galaxy decomposition.

6.1.4 HE1029 – 1401

Inner region shows a rotational profile (Fig. 6.3c) and for the harmonic expansion analysis we exclude the tidal tail. The best circular velocity model produces a residual where we can see two arm-like velocity structures with opposite velocities. The one which is blueshifted with respect to the center extends from the South-West to the North-West direction of the quasar position and the other one, which is redshifted extends from the North-East to the South-East. The redshifted arm seems to be connected with the outer tidal tail.

The rotational curve is regular for the inner part and there is a tendency to decreasing velocities toward the outer regions. Since the kinematic center is not offset from the optical center, we still classify this galaxy as being kinematically mildly distorted.

6.1.5 HE1043 – 1346

Very regular velocity field (Fig. 6.4c). Our best circular velocity model suggests some low level decoupled center, but nothing pointing to distortions from a recent interaction.

6.1.6 HE1110 – 1910

An elliptical galaxy with a confirmed companion to the North-West. The host galaxy spectrum produced from our quasar–host galaxy decomposition method is really faint hence we cannot do kinematic analysis for this object. We summarized as "Unclear class".

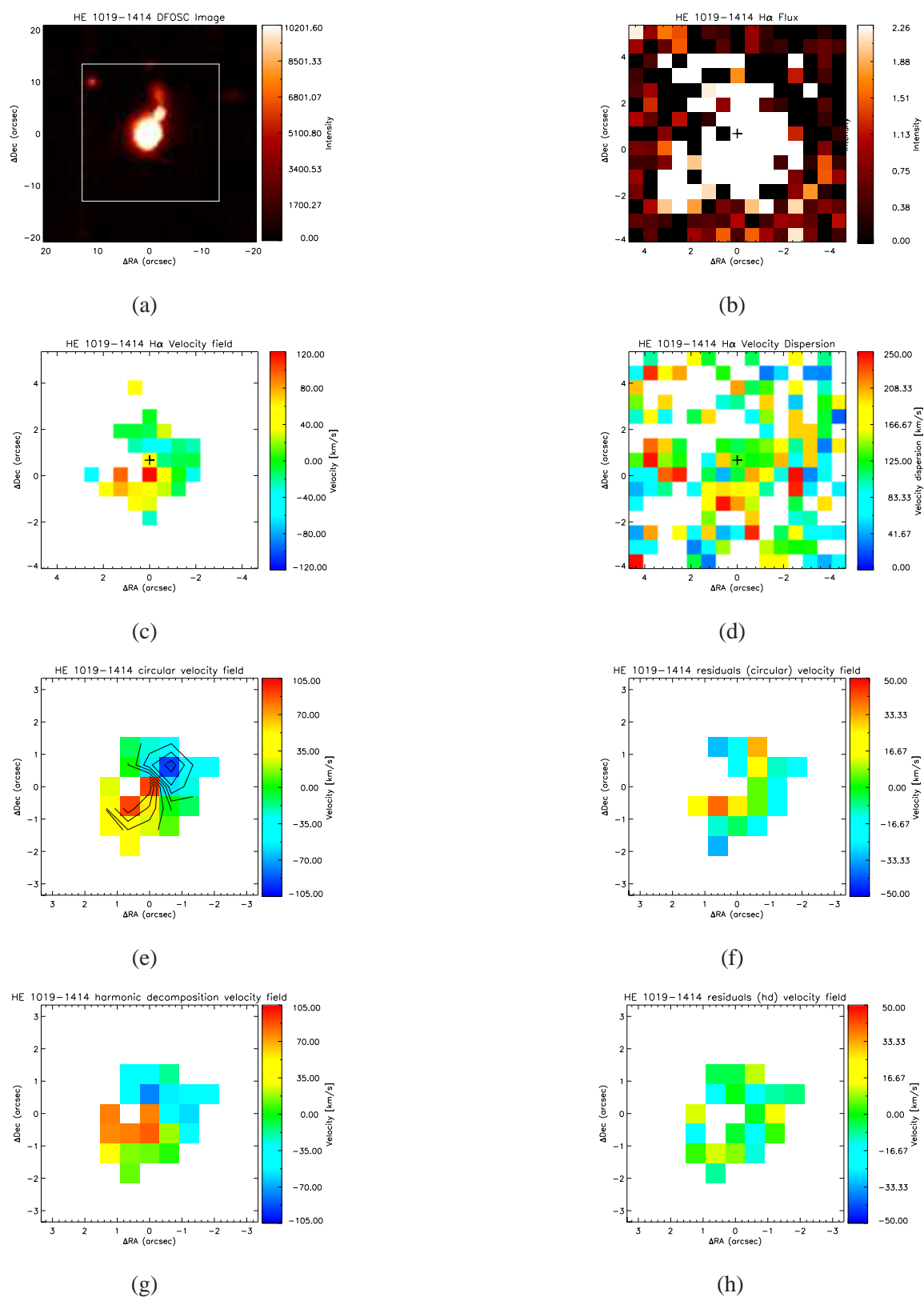


Figure 6.2: Kinematical analysis for HE 1019-1414. Shown are (a) optical broad-band image, (b) H α flux map from VIMOS, (c) H α velocity field, (d) H α velocity dispersion map, (e) best circular velocity model and (f) residuals after subtracting the observed velocity field with circular velocity model, (g) full harmonic decomposition velocity model and (h) residuals after subtracting the observed velocity field with harmonic decomposition velocity model. North is up, East is left.

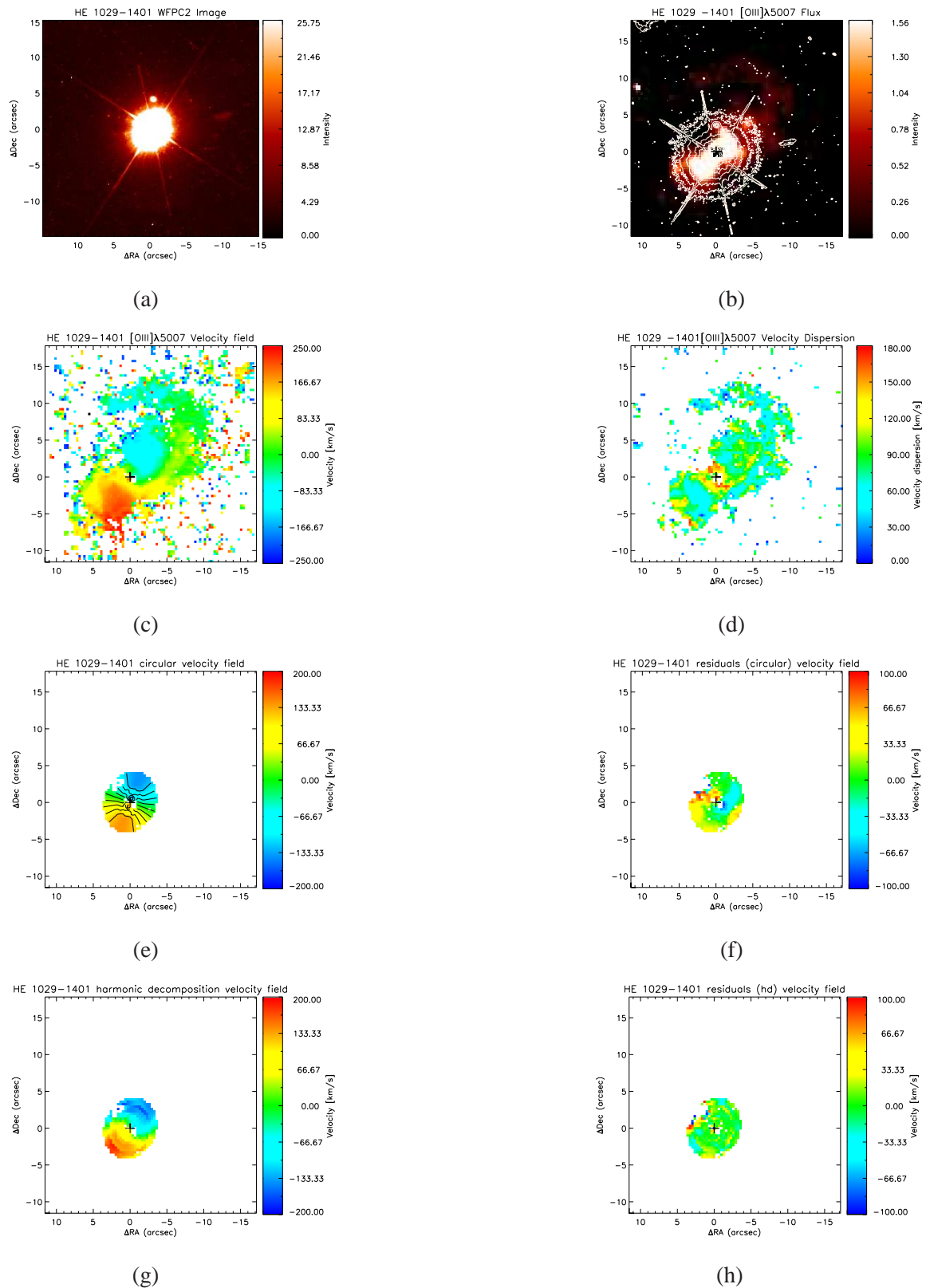


Figure 6.3: Kinematical analysis for HE 1029-1401. Shown are (a) optical broad-band image, (b) [OIII] λ 5007 flux map from VIMOS, (c) [OIII] λ 5007 velocity field, (d) [OIII] λ 5007 velocity dispersion map, (e) best circular velocity model and (f) residuals after subtracting the observed velocity field with circular velocity model, (g) full harmonic decomposition velocity model and (h) residuals after subtracting the observed velocity field with harmonic decomposition velocity model. North is up, East is left.

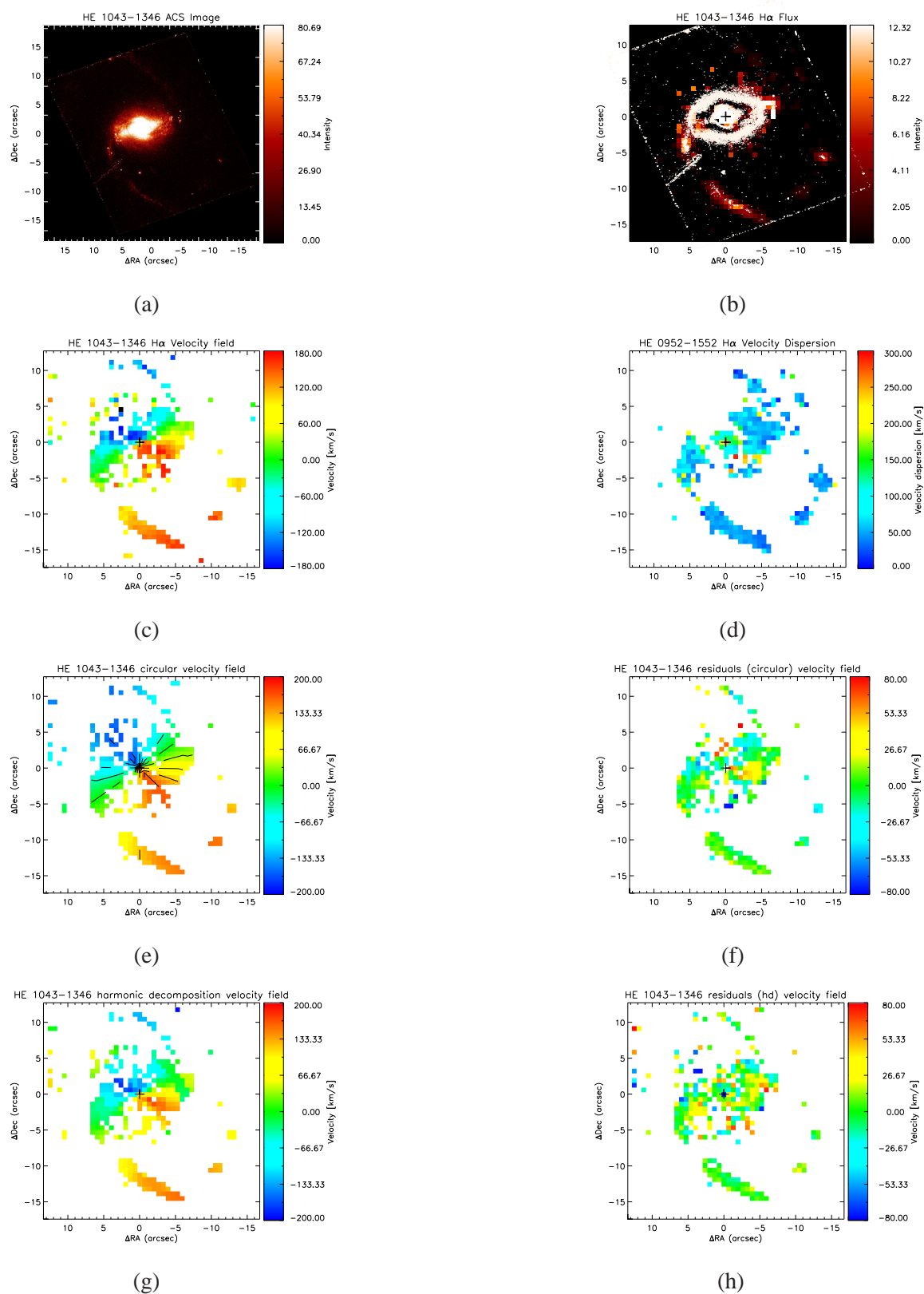


Figure 6.4: Kinematical analysis for HE 1043-1346. Shown are (a) optical broad-band image, (b) H α flux map from VIMOS, (c) H α velocity field, (d) H α velocity dispersion map, (e) best circular velocity model and (f) residuals after subtracting the observed velocity field with circular velocity model, (g) full harmonic decomposition velocity model and (h) residuals after subtracting the observed velocity field with harmonic decomposition velocity model. North is up, East is left.

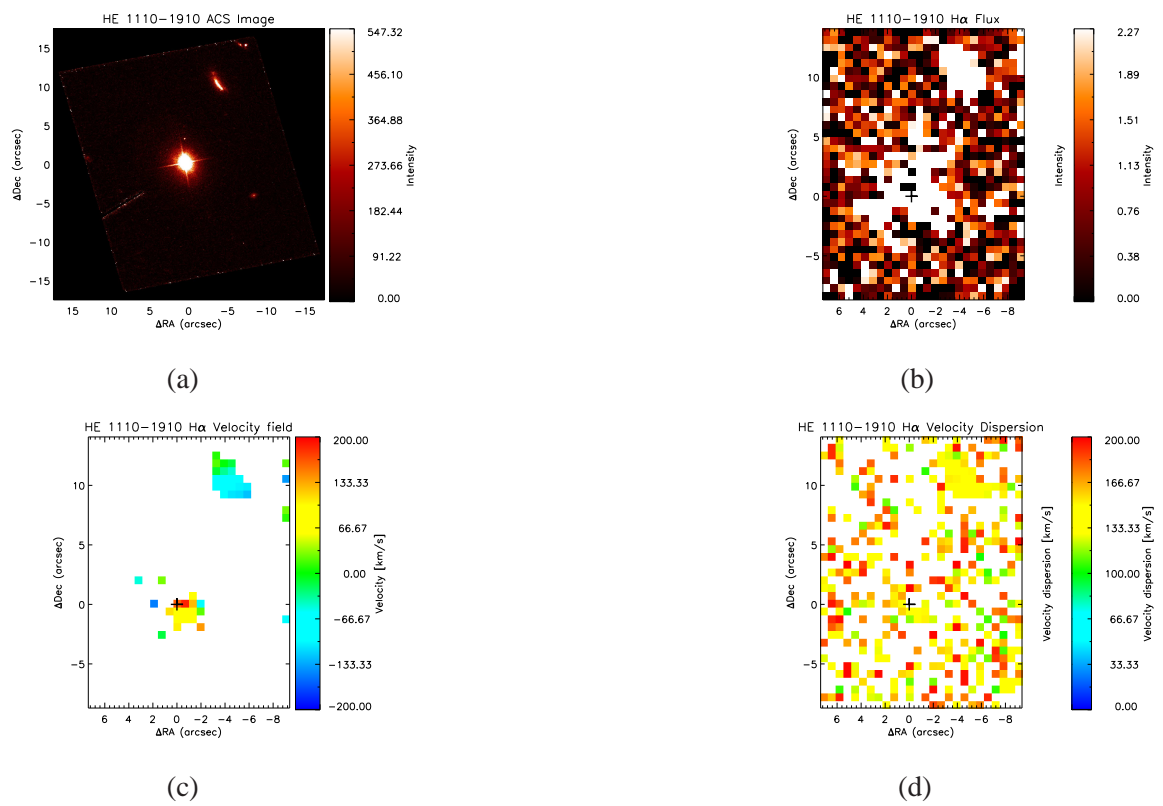


Figure 6.5: Kinematical analysis for HE 1110–1910. Shown are (a) optical broad-band image, (b) H α flux map from VIMOS, (c) H α velocity field, (d) H α velocity dispersion map. North is up, East is left.

6.1.7 HE1201 – 2409

A symmetric elliptical galaxy. Even though our observation covers only half of the host galaxy, the flux map shows no additional structure and the velocity field indicates purely rotational motion (Fig. 6.6c).

6.1.8 HE1228 – 1637

The velocity field shows rotation motion in the inner part and starting from ~ 6.4 kpc, further outside it deviates from pure rotation motion. We classify this as mildly distorted.

This quasar shows both in the image and velocity field ((Fig. 6.8a) and (Fig. 6.8c) respectively) an extra structure to the south. The fit is reasonably well with one component for the other part of the host galaxy except this region. A fit with multiple Gaussians provides two separate velocity components in this region. Kinematically this is still classified as mildly distorted according to our scheme.

6.1.9 HE1237 – 2252

6.1.10 HE1239 – 2426

This host galaxy is one of the best example for kinematic modeling in our sample (Fig. 6.9). The velocity map and rotation curve indicate a simple rotating disk and the velocity dispersion is large (~ 150 km/sec) in the inner region and in the brightest spot in the spiral arm in North-East direction. Both these regions of the host galaxy The latter are two regions of the host galaxy are actually dispersion dominated.

The residual map after subtracting circular velocity field model from the observed velocity map shows only ~ 20 km/sec residuals along the spiral structure. This is clearly kinematically undistorted galaxy.

6.1.11 HE1254 – 0934

The velocity field (Fig. 6.10c) exhibits complex structures with a rotational profile for the first companion to the West, and a tidal tail which is also detected in the optical image. Surprisingly

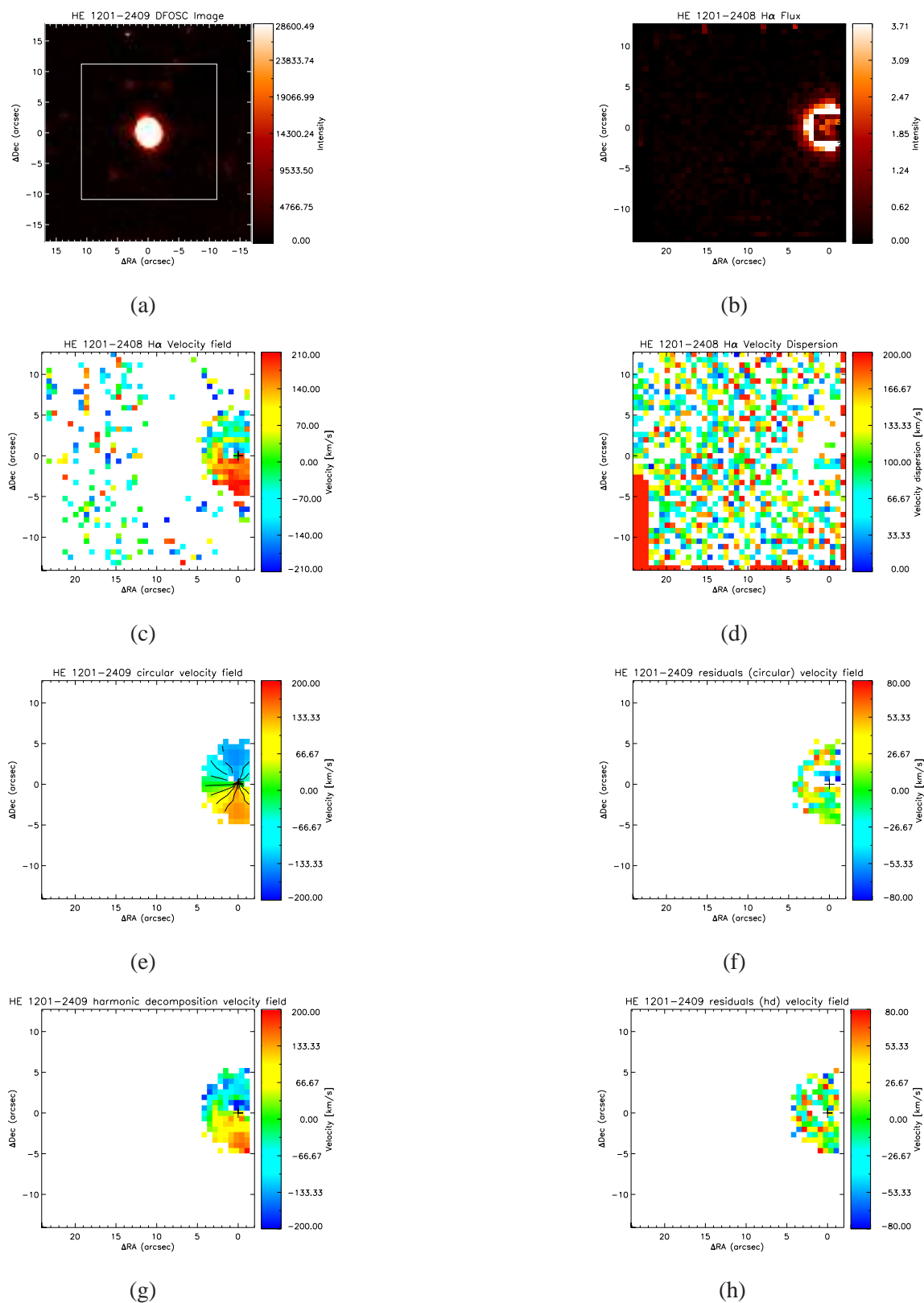


Figure 6.6: Kinematical analysis for HE 1201–2409. Shown are (a) optical broad-band image, (b) H α flux map from VIMOS, (c) H α velocity field, (d) H α velocity dispersion map, (e) best circular velocity model and (f) residuals after subtracting the observed velocity field with circular velocity model, (g) full harmonic decomposition velocity model and (h) residuals after subtracting the observed velocity field with harmonic decomposition velocity model. North is up, East is left.

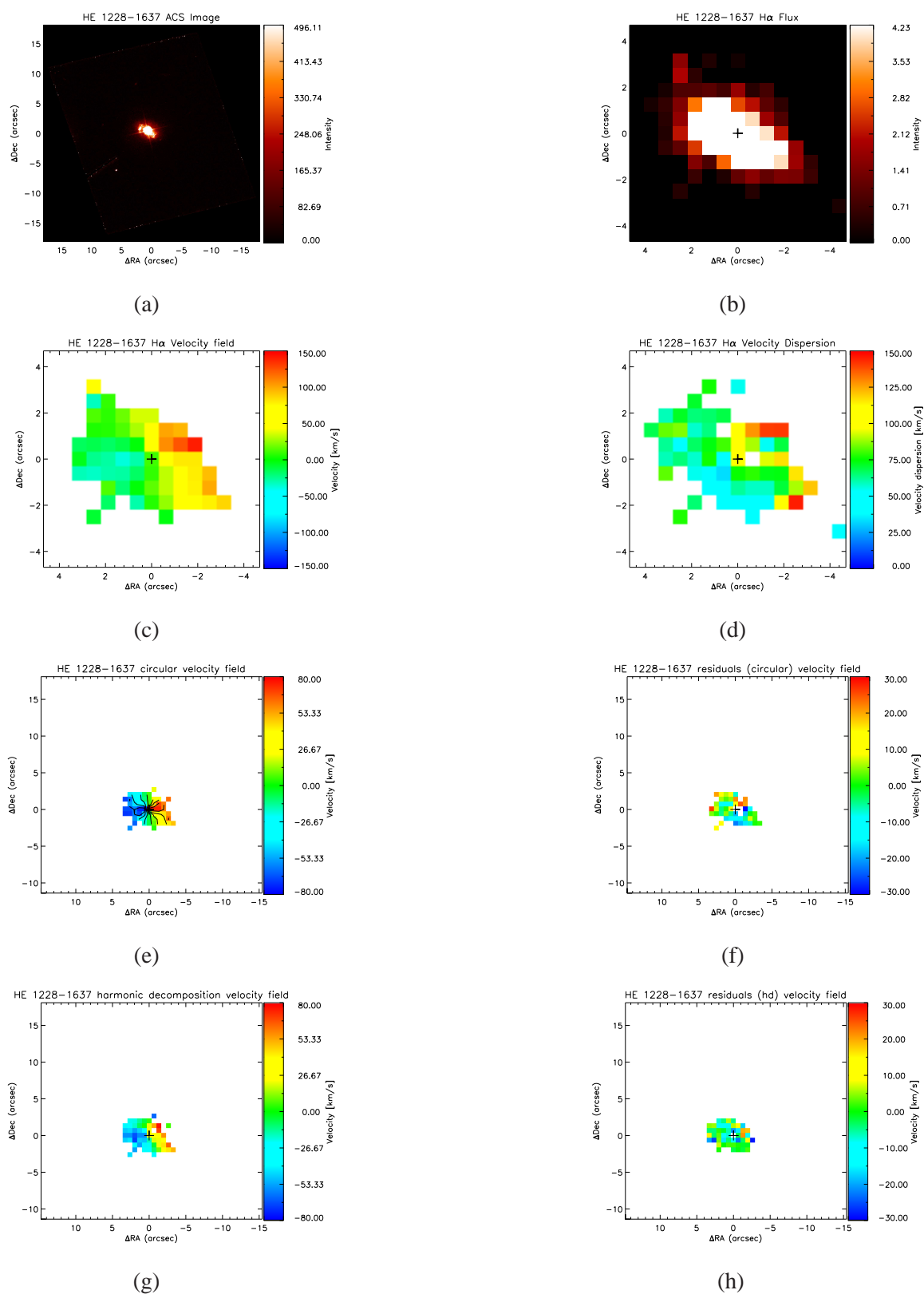


Figure 6.7: Kinematical analysis for HE 1228-1637. Shown are (a) optical broad-band image, (b) H α flux map from VIMOS, (c) H α velocity field, (d) H α velocity dispersion map, (e) best circular velocity model and (f) residuals after subtracting the observed velocity field with circular velocity model, (g) full harmonic decomposition velocity model and (h) residuals after subtracting the observed velocity field with harmonic decomposition velocity model. North is up, East is left.

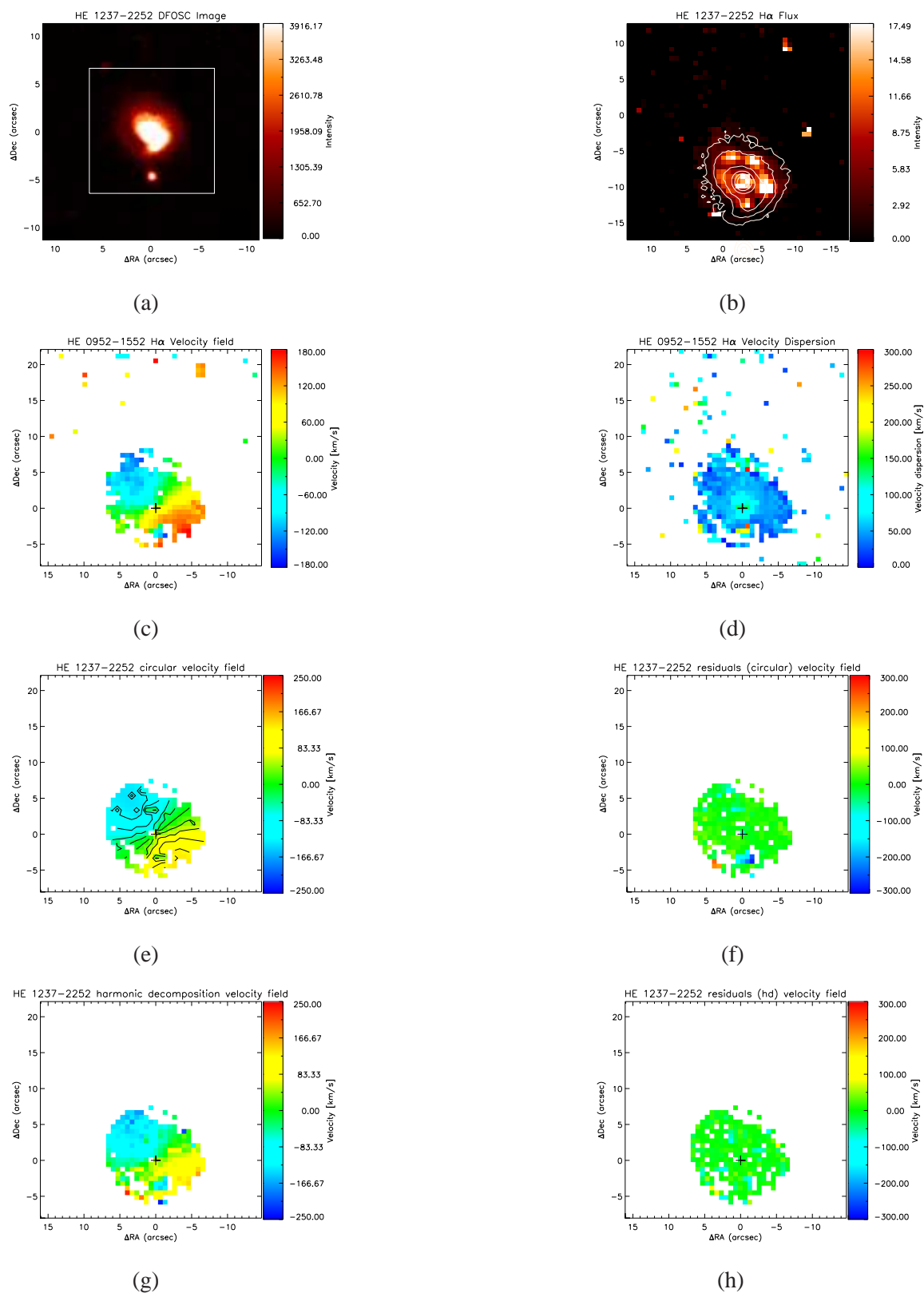


Figure 6.8: Kinematical analysis for HE 1237-1552. Shown are (a) optical broad-band image, (b) H α flux map from VIMOS, (c) H α velocity field, (d) H α velocity dispersion map, (e) best circular velocity model and (f) residuals after subtracting the observed velocity field with circular velocity model, (g) full harmonic decomposition velocity model and (h) residuals after subtracting the observed velocity field with harmonic decomposition velocity model. North is up, East is left.

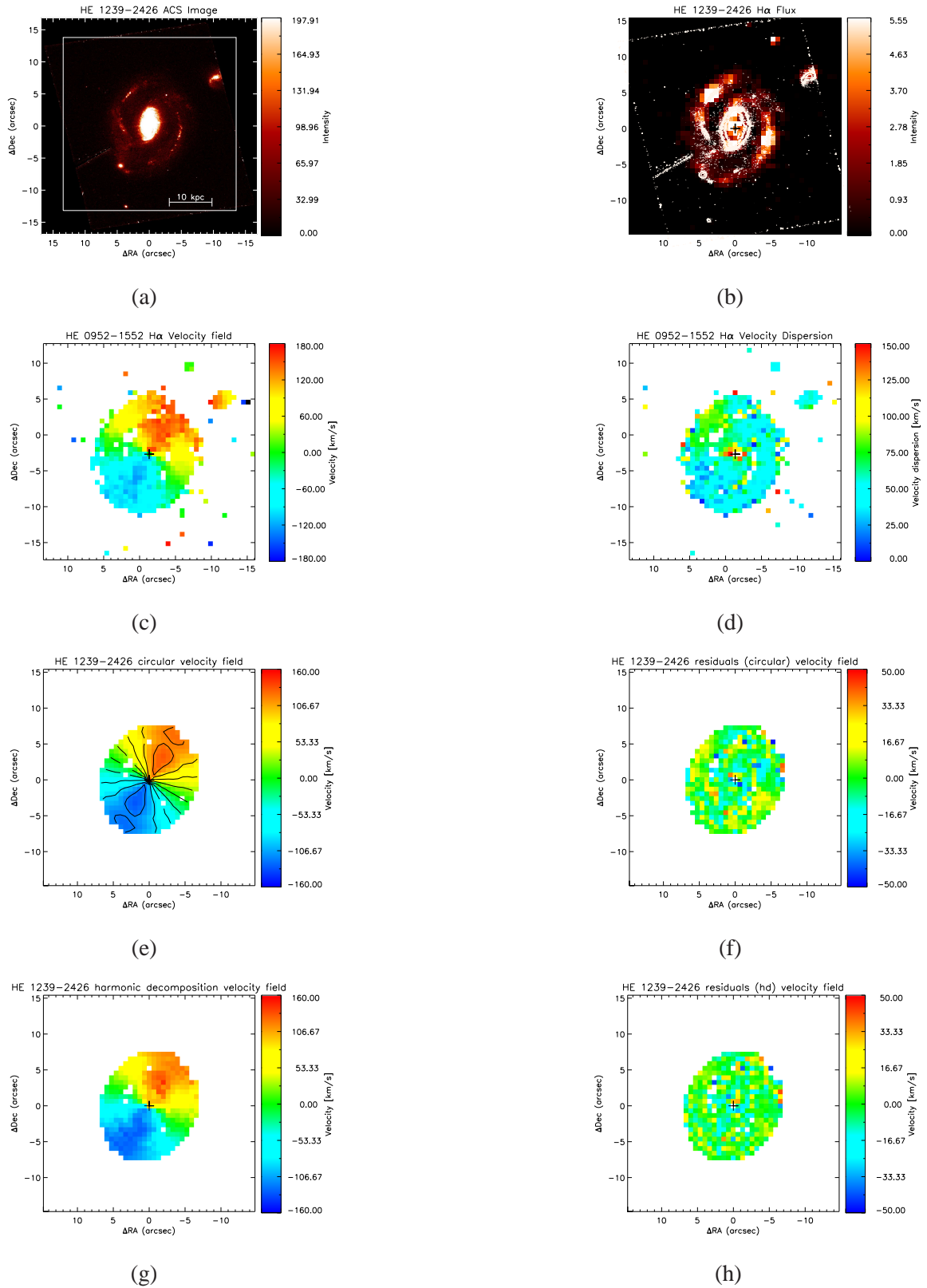


Figure 6.9: Kinematical analysis for HE 1239–2426. Shown are (a) optical broad-band image, (b) H α flux map from VIMOS, (c) H α velocity field, (d) H α velocity dispersion map, (e) best circular velocity model and (f) residuals after subtracting the observed velocity field with circular velocity model, (g) full harmonic decomposition velocity model and (h) residuals after subtracting the observed velocity field with harmonic decomposition velocity model. North is up, East is left.

we detect another tidal tail in the opposite direction which is not detected in the optical image. This galaxy is kinematically very strongly distorted galaxy.

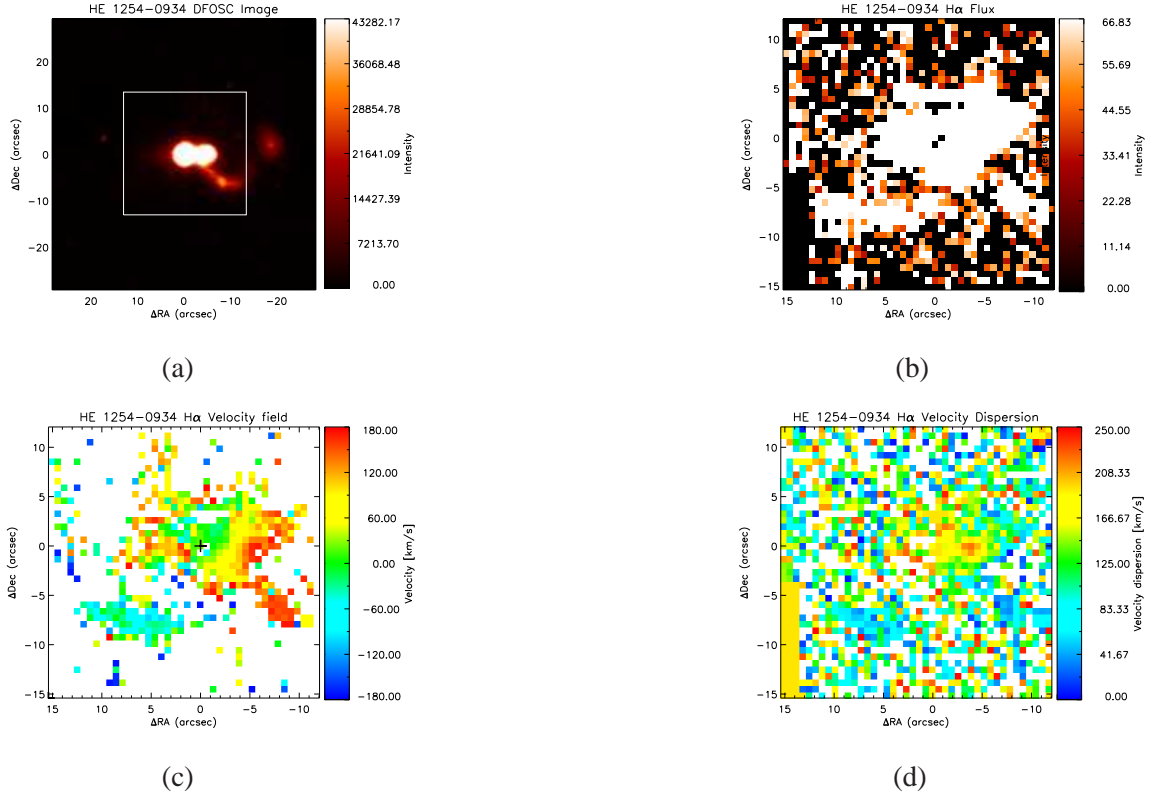


Figure 6.10: Kinematical analysis for HE 1254–0934. Shown are (a) optical broad-band image, (b) H α flux map from VIMOS, (c) H α velocity field, (d) H α velocity dispersion map, (e) best circular velocity model and (f) residuals after subtracting the observed velocity field with circular velocity model, (g) full harmonic decomposition velocity model and (h) residuals after subtracting the observed velocity field with harmonic decomposition velocity model. North is up, East is left.

6.1.12 HE1300 – 1325

The velocity field (Fig. 6.11c) reveals only some coordinated rotation in the host galaxy and it deviates from circular rotation immediately outside the center based from our modeling. Basically, any rotation model is a very poor fit, hence we also classify this galaxy as very distorted.

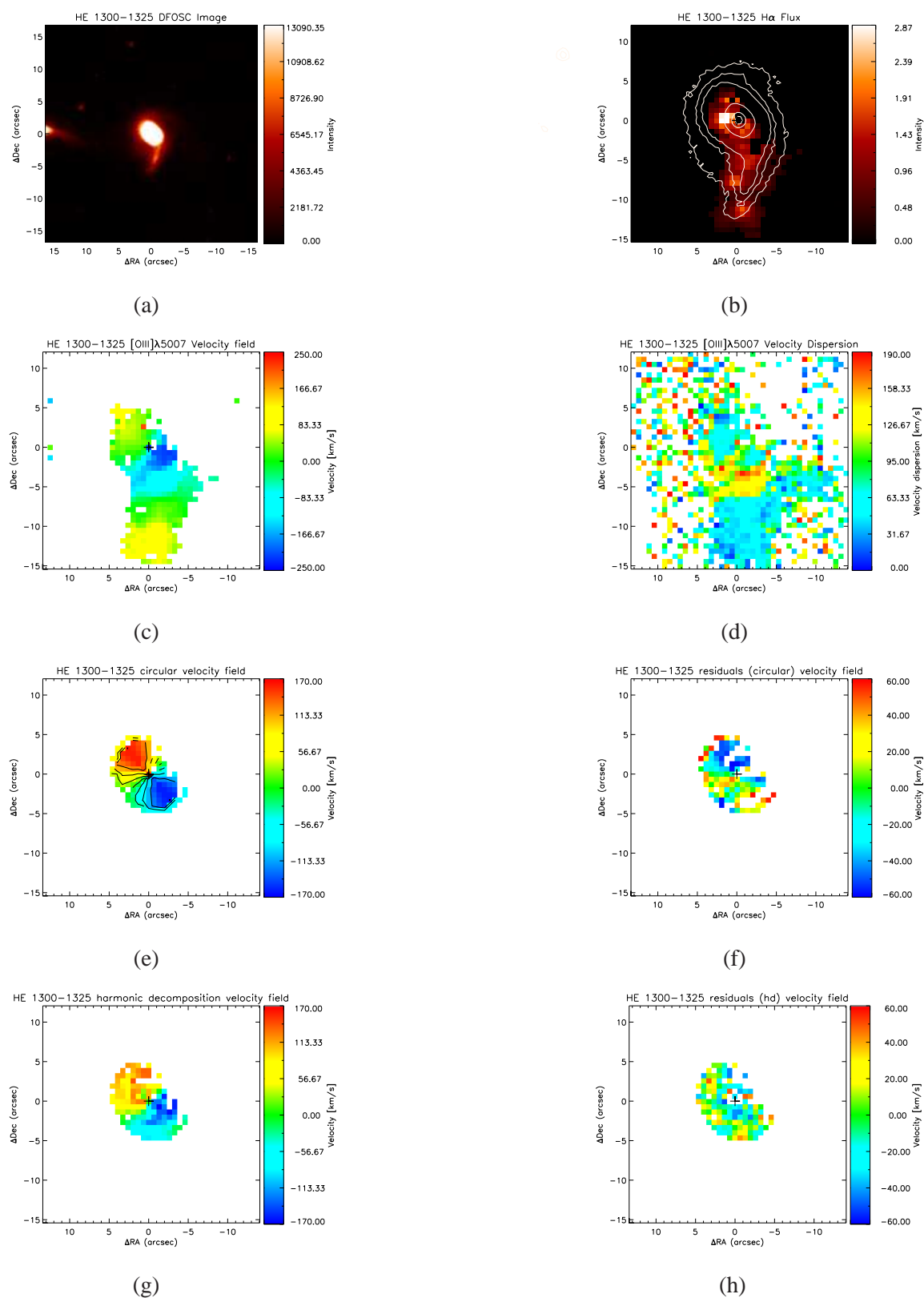


Figure 6.11: Kinematical analysis for HE 1300–1325. Shown are (a) optical broad-band image, (b) [OIII] λ 5007 flux map from VIMOS, (c) [OIII] λ 5007 velocity field, (d) [OIII] λ 5007 velocity dispersion map, (e) best circular velocity model and (f) residuals after subtracting the observed velocity field with circular velocity model, (g) full harmonic decomposition velocity model and (h) residuals after subtracting the observed velocity field with harmonic decomposition velocity model. North is up, East is left.

6.1.13 HE1310 – 1051

From our kinematic modeling, this host galaxy has coordinated rotational motion only inside 4 kpc from the center, outside of this substantial peculiar velocities dominate. This galaxy also qualifies as strongly distorted, fulfilling ("yes") 3 out of 4 distorted kinematic criteria.

6.1.14 HE1315 – 1028

We classify this galaxy as unclear class due to low signal host galaxy (see Fig. 6.13).

6.1.15 HE1335 – 0847

Similar with HE 1315–1028, due to low signal of the host galaxy we classify this object as unclear class.

6.1.16 HE1338 – 1423

The residual from our best circular rotation model (Fig. 6.15f) shows two velocity structures with different velocities. One, in the Eastern part of the host galaxy, being clearly a peculiar extra component. apart from this there is substantial twisting of the velocity field but no strong indicator for substantial distortions.

6.1.17 HE1405 – 1545

Surprisingly for an obviously interacting system, the whole system shows only rotational motion (see Fig. 6.16c), except that the residual shows a second distinct velocity structure. with different velocity. It lies East-West and shows velocities of $\sim + 40$ km/sec and $\sim - 50$ km/sec, respectively, with respect to the quasar. From kinematics alone, this system is only mildly distorted.

6.1.18 HE1416 – 1256

The velocity field (Fig. 6.17c) exhibits rotation in the host galaxy plus a tidal tail, blueshifted near the host galaxy with velocity ~ 40 km/sec. The inner region has circular motion until distance~

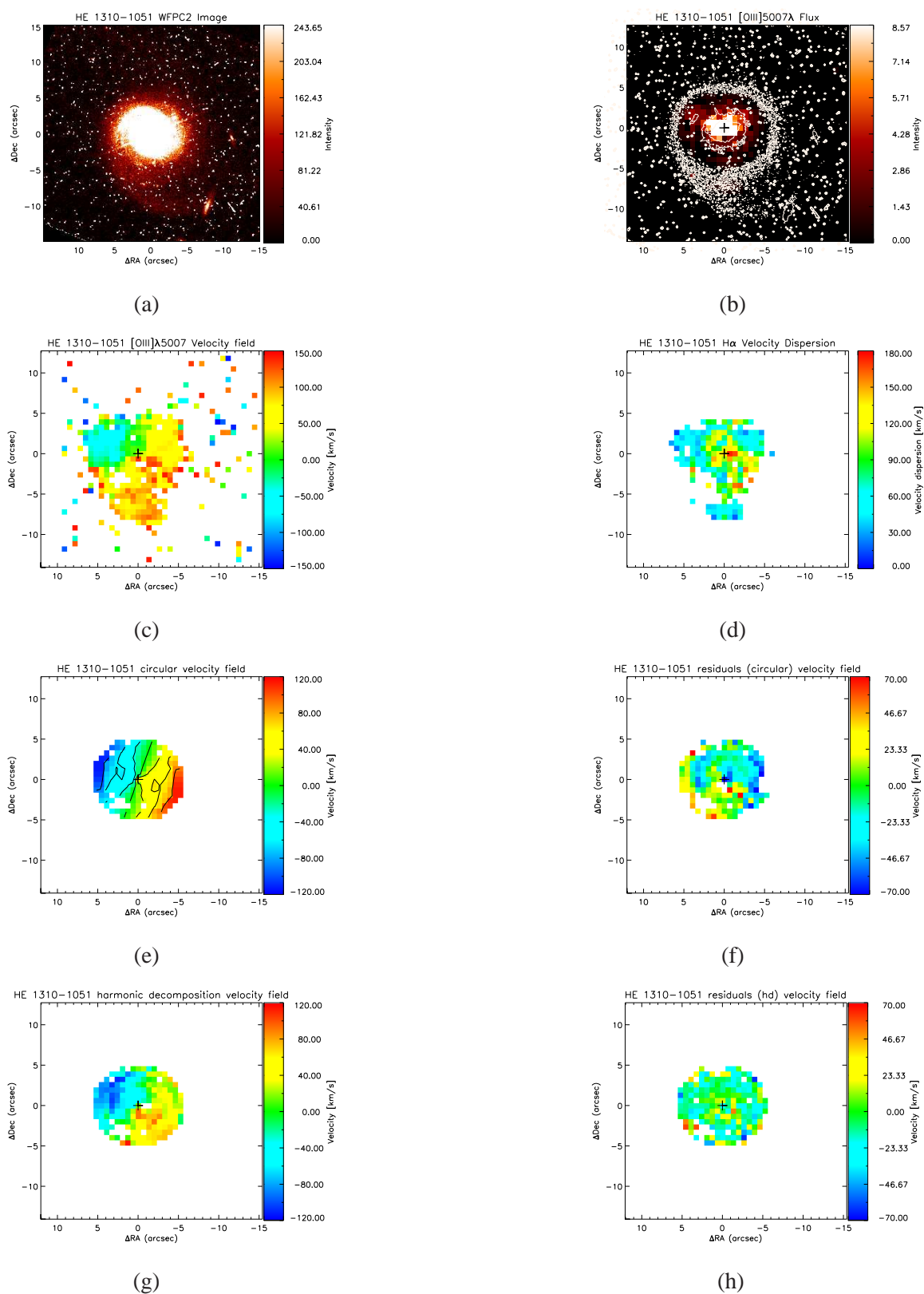


Figure 6.12: Kinematical analysis for HE 1310–1051. Shown are (a) optical broad-band image, (b) [OIII] λ 5007 flux map from VIMOS, (c) [OIII] λ 5007 velocity field, (d) [OIII] λ 5007 velocity dispersion map, (e) best circular velocity model and (f) residuals after subtracting the observed velocity field with circular velocity model, (g) full harmonic decomposition velocity model and (h) residuals after subtracting the observed velocity field with harmonic decomposition velocity model. North is up, East is left.

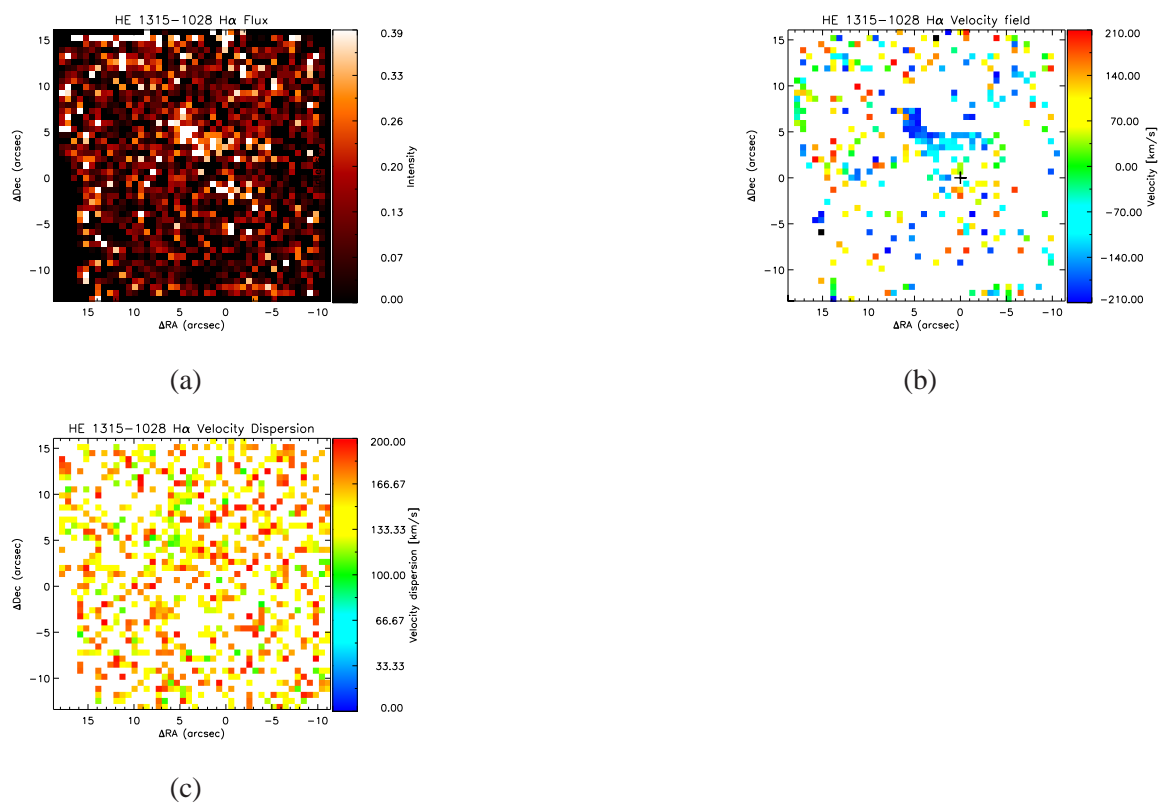


Figure 6.13: Kinematical analysis for HE 1315-1028. Shown are (a) H α flux map from VIMOS, (b) H α velocity field, (c) H α velocity dispersion map. North is up, East is left.

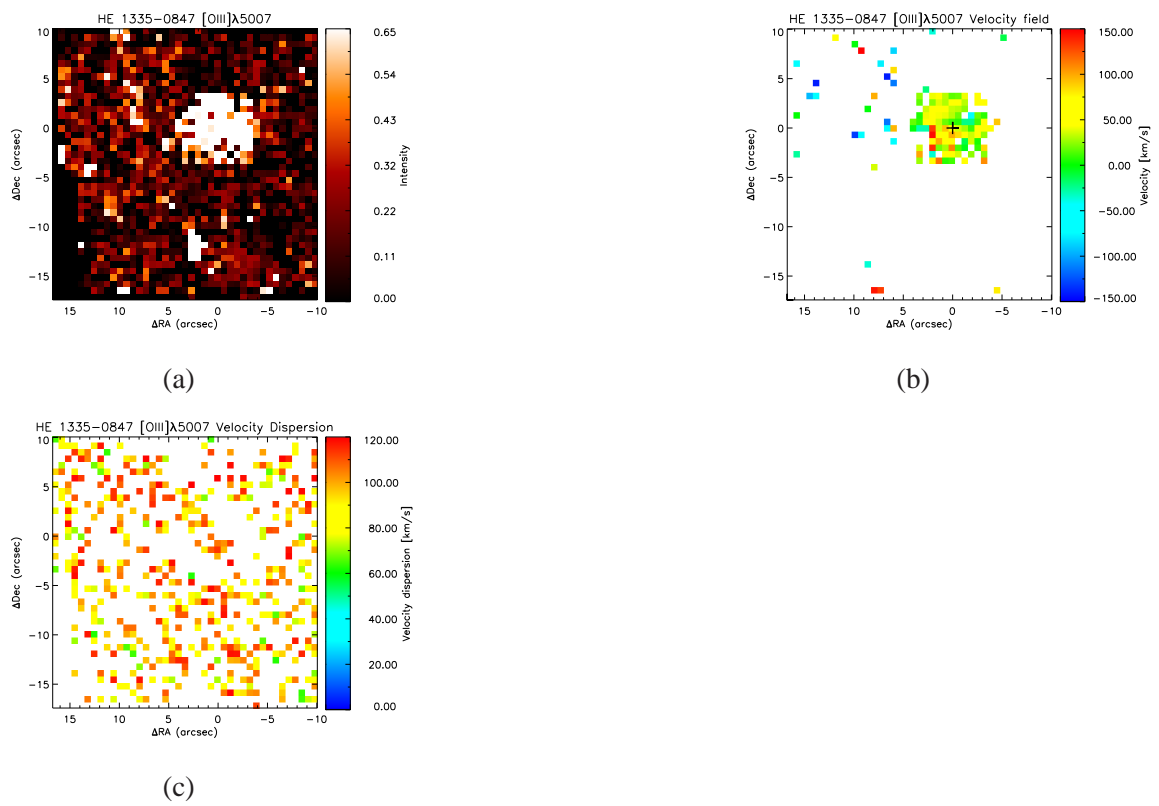


Figure 6.14: Kinematical analysis for HE 1335-0847. Shown are (a) [OIII] λ 5007 flux map from VIMOS, (b) [OIII] λ 5007 velocity field, (c) [OIII] λ 5007 velocity dispersion map. North is up, East is left.

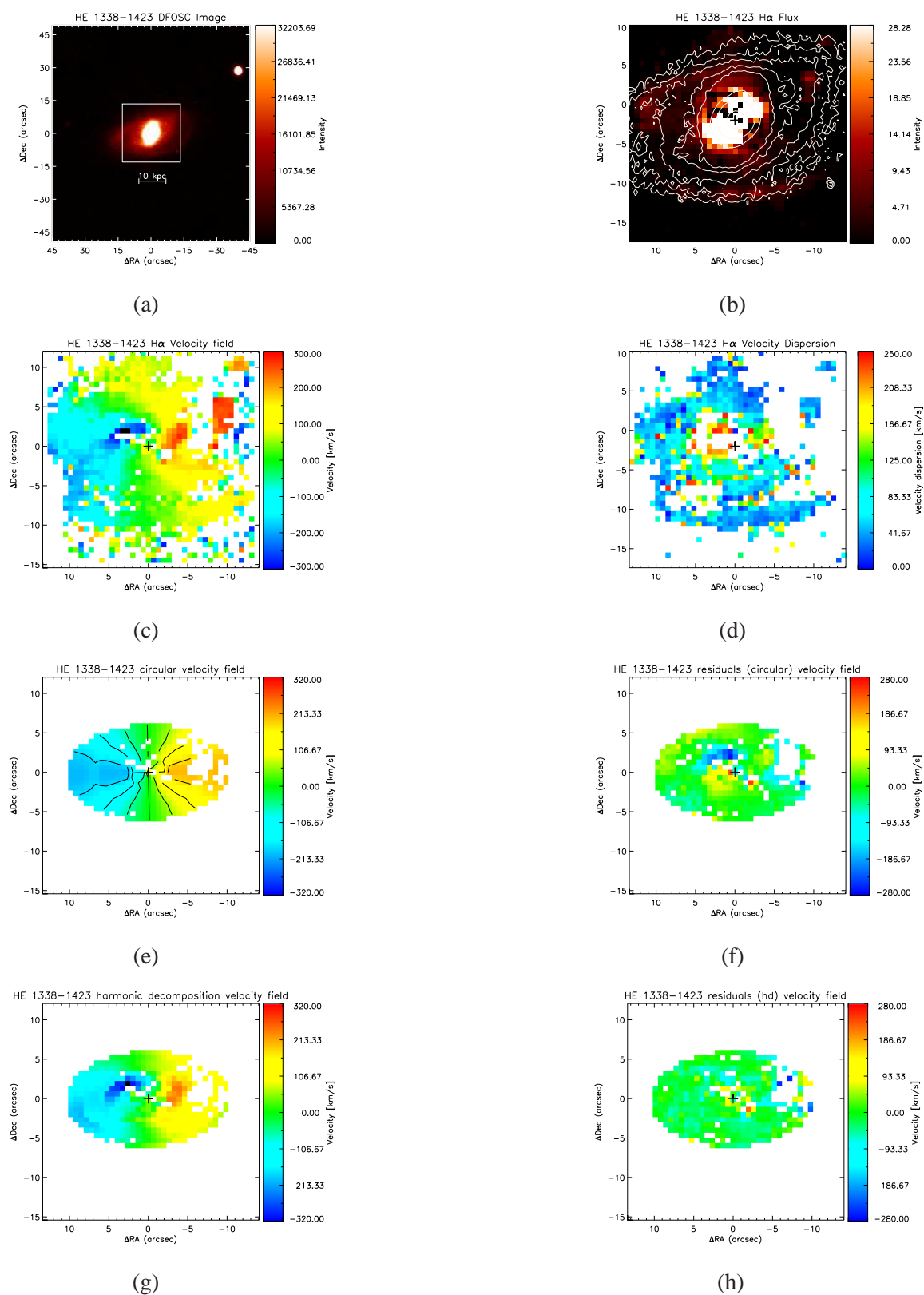


Figure 6.15: Kinematical analysis for HE 1338-1423. Shown are (a) optical broad-band image, (b) H α flux map from VIMOS, (c) H α velocity field, (d) H α velocity dispersion map, (e) best circular velocity model and (f) residuals after subtracting the observed velocity field with circular velocity model, (g) full harmonic decomposition velocity model and (h) residuals after subtracting the observed velocity field with harmonic decomposition velocity model. North is up, East is left.

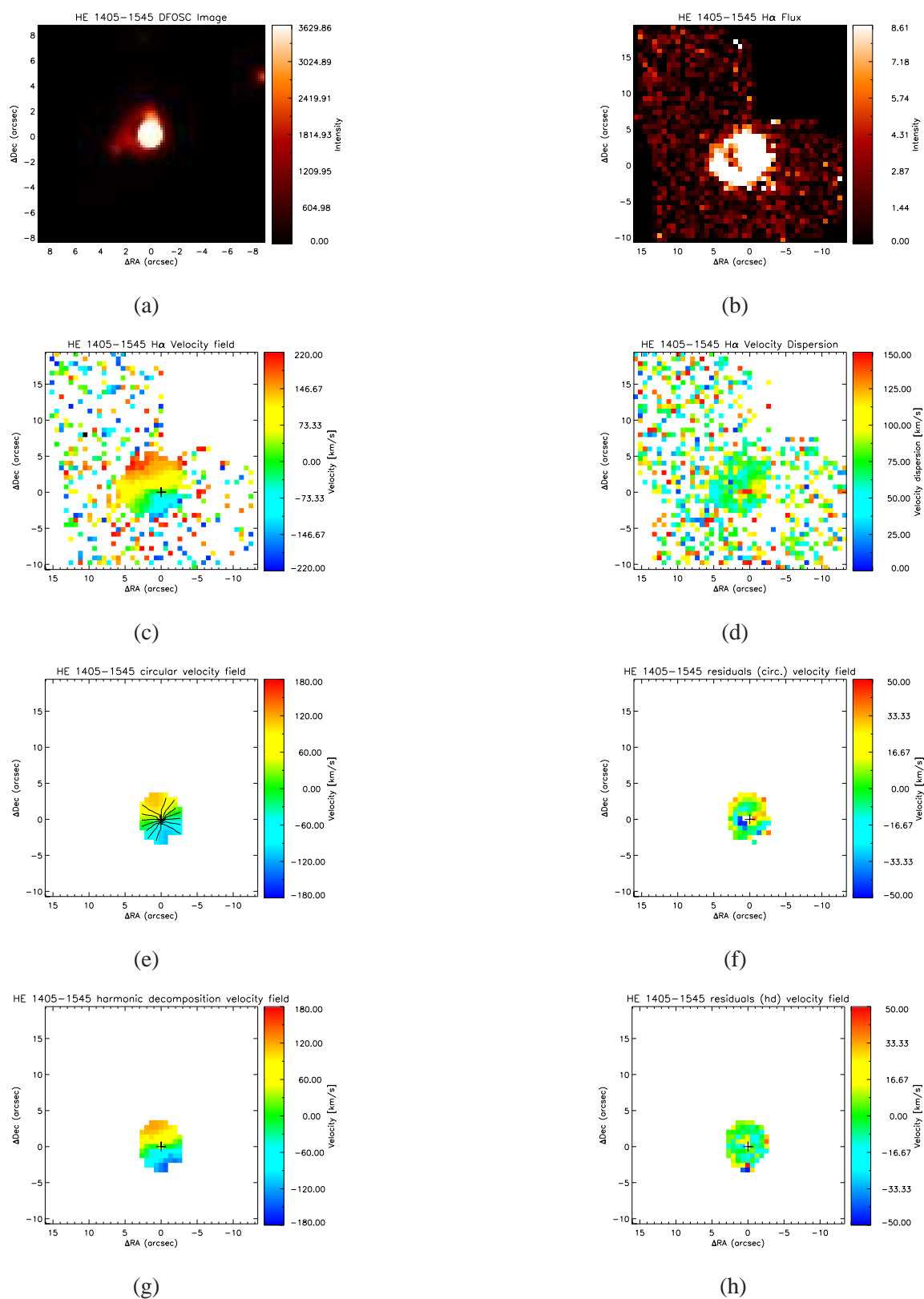


Figure 6.16: Kinematical analysis for HE 1405–1545. Shown are (a) optical broad-band image, (b) H α flux map from VIMOS, (c) H α velocity field, (d) H α velocity dispersion map, (e) best circular velocity model and (f) residuals after subtracting the observed velocity field with circular velocity model, (g) full harmonic decomposition velocity model and (h) residuals after subtracting the observed velocity field with harmonic decomposition velocity model. North is up, East is left.

6.7 kpc from the center. The South-East tail consists of two velocity structures, blueshifted near the host galaxy and redshifted in the remaining part. we consider this system as mildly distorted based on our classification scheme.

6.1.19 HE1434 – 1600

Unfortunately, our observation cannot covers the whole object extension. The velocity field shows rotation motion of the ionized gas (Fig. 6.18c) .

6.2 VELOCITY CLASSIFICATION RESULTS

Here we describe our classification in more detailed. We use these parameter to analyze the velocity fields and to classify the distortion level:

1. Interaction signatures: galaxies interaction can change original morphology of velocity fields and produce additional features for example tidal tail, bridge etc.
2. Kinematics center: interaction also can produce an offset between center of the optical image and center of the velocity field from emission line.
3. Rotation curve irregularity: deviation from regular rotational velocity curve can be a dip or decreasing rotation velocity at the outer part.
4. Dispersion map profile irregularity: distorted dispersion map will not shows a clear peak of dispersion velocity near the kinematic center.

Using those parameters which we describe in section 4.2.2 we classify the state of each host galaxy kinematic as already stated in the description of each object above. We summarize this in Table 6.2 in the shape of a "decision matrix" to classify our velocity fields. The optical classification comes from Jahnke et al. (2004a), who provide a classification for morphological type (disk-, spheroid-dominated) and distortions. We update the latter for those objects with new HST imaging data, which largely confirms the previous classification. If a velocity field does not ("no") satisfy any parameters we classify it as "regular" velocity field. For "distorted" class we divide into two sub-classes: strongly distorted and mildly distorted. If a velocity field 3 or all of the criteria ("yes") then we classify it as "strongly distorted", and one or two of the criteria as "mildly distorted" velocity field. Table 6.2 summarizes our final kinematical classification.

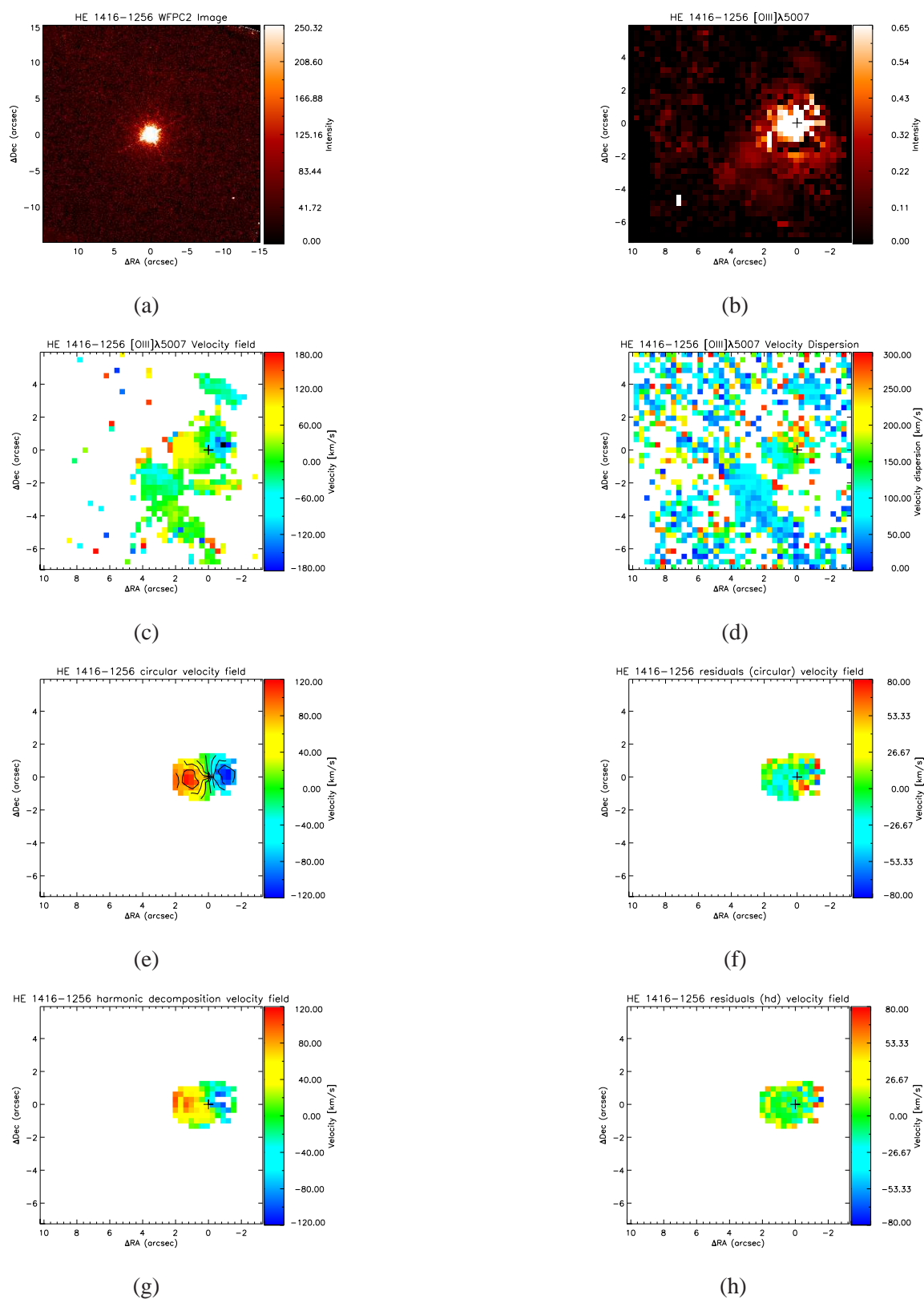


Figure 6.17: Kinematical analysis for HE 1416–1256. Shown are (a) optical broad-band image, (b) [OIII] λ 5007 flux map from VIMOS, (c) [OIII] λ 5007 velocity field, (d) [OIII] λ 5007 velocity dispersion map, (e) best circular velocity model and (f) residuals after subtracting the observed velocity field with circular velocity model, (g) full harmonic decomposition velocity model and (h) residuals after subtracting the observed velocity field with harmonic decomposition velocity model. North is up, East is left.

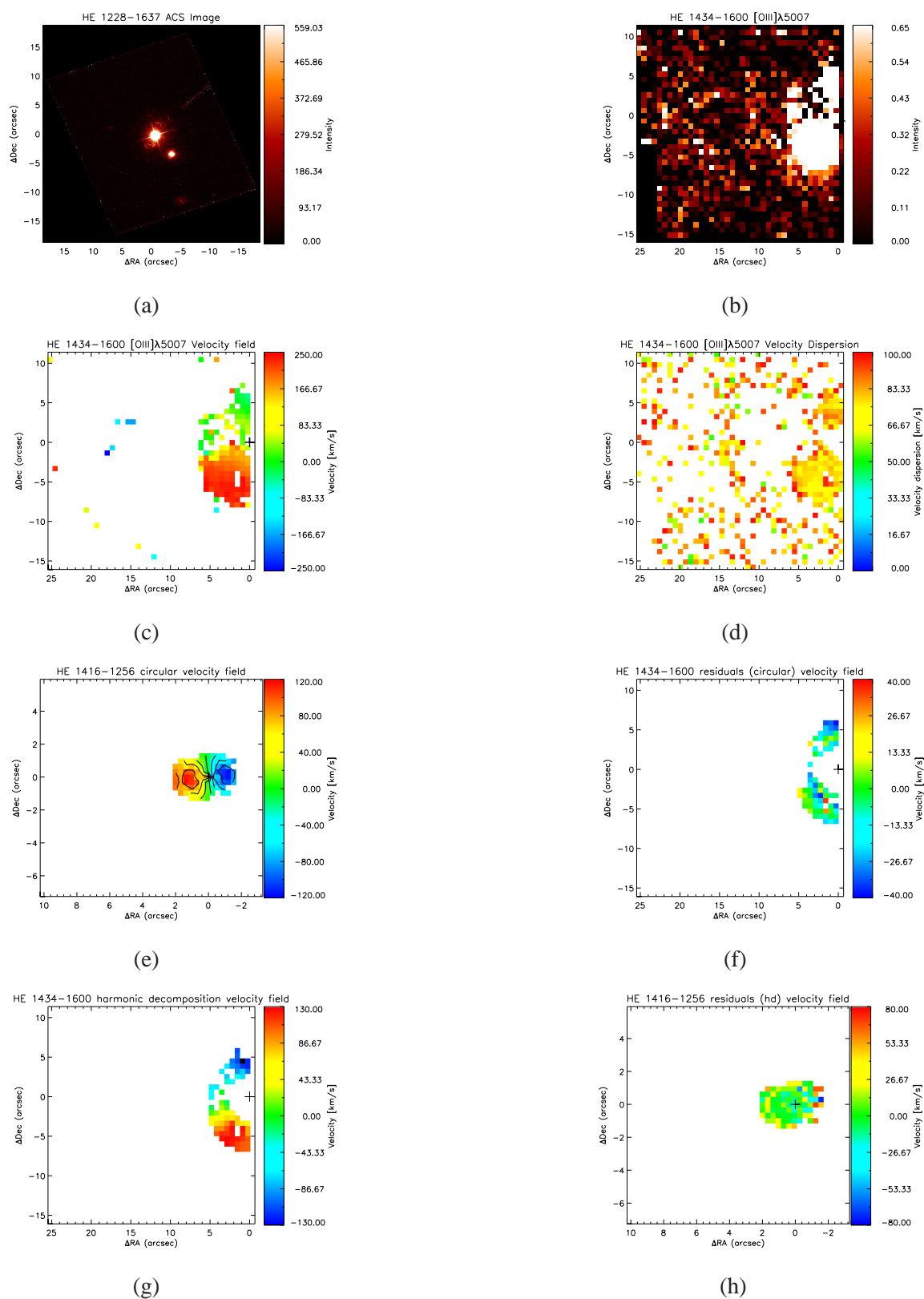


Figure 6.18: Kinematical analysis for HE 1434–1600. Shown are (a) optical broad-band image, (b) [OIII] λ 5007 flux map from VIMOS, (c) [OIII] λ 5007 velocity field, (d) [OIII] λ 5007 velocity dispersion map, (e) best circular velocity model and (f) residuals after subtracting the observed velocity field with circular velocity model, (g) full harmonic decomposition velocity model and (h) residuals after subtracting the observed velocity field with harmonic decomposition velocity model. North is up, East is left.

Table 6.1: Summary of the kinematics parameters.

Name	Offset of the kinematics center (arcsec)	Position Angle (PA) (Degrees)	Inclination (Degrees)	Quality Flag
(1)	(2)	(3)	(4)	
HE 0952–1552	0.243 ^{+0.005} _{-0.038}	0.16 ^{+0.25} _{-0.21}	50.31 ^{+5.35} _{-0.36}	1
HE 1019–1414	0.449 ^{+0.046} _{-0.301}	138.43 ^{+21.83} _{-1.39}	49.56 ^{+2.48} _{-9.93}	1
HE 1020–1022	–	–	–	0
HE 1029–1401	0.038 ^{+0.041} _{-0.048}	160.00 ^{+0.00} _{-0.00}	36.96 ^{+5.21} _{-2.77}	1
HE 1043–1346	0.150 ^{+0.171} _{-0.195}	206.68 ^{+1.30} _{-9.44}	41.80 ^{+0.67} _{-0.74}	1
HE 1110–1901	–	–	–	0
HE 1201–2409	0.292 ^{+0.182} _{0.062}	-188.74 ^{+5.12} _{-2.92}	38.15 ^{+0.96} _{-2.66}	1
HE 1228–1637	0.298 ^{+0.023} _{-0.235}	-80.00 ^{+0.00} _{-0.00}	57.10 ^{+0.00} _{-1.62}	1
HE 1237–3352	0.249 ^{+0.193} _{-0.041}	-136.33 ^{+3.91} _{-3.70}	41.78 ^{+0.63} _{-1.04}	1
HE 1239–2426	0.205 ^{+0.034} _{-0.084}	-30 ^{+0.00} _{-0.00}	36.24 ^{+1.11} _{-2.33}	1
HE 1254–0934	2.661 ^{+0.251} _{-0.209}	-105.69 ^{+4.08} _{-4.74}	51.65 ^{+1.77} _{-2.73}	1
HE 1300–1325	0.639 ^{+0.009} _{-0.521}	40.00 ^{+0.00} _{-0.00}	65.18 ^{+0.11} _{-0.10}	1
HE 1310–1051	0.913 ^{+0.146} _{-0.096}	-110.00 ^{+0.00} _{-0.00}	39.32 ^{+2.82} _{-0.41}	1
HE 1315–1028	–	–	–	0
HE 1335–0847	–	–	–	0
HE 1338–1423	0.234 ^{+0.097} _{-0.458}	-89.59 ^{+2.91} _{-0.43}	57.06 ^{+0.21} _{-0.38}	1
HE 1405–1545	0.278 ^{+0.018} _{-0.023}	20.00 ^{+0.00} _{-0.00}	27.72 ^{+1.90} _{-0.91}	1
HE 1416–1256	0.281 ^{+0.118} _{-0.114}	90.14 ^{+6.69} _{-13.95}	52.73 ^{+9.80} _{-10.44}	1
HE 1434–1600	0.911 ^{+0.219} _{-0.197}	161.29 ^{+10.32} _{-9.88}	49.28 ^{+3.52} _{-2.47}	1

Notes. (1) Name from original catalogue; (2) Offset of the kinematic center of the host galaxies relative to the QSO position; (3) Position angle of the ellipses for the kinematics model, measured from North to East; (4) Inclination of the the ellipses for the kinematics model; (5) Quality flag of the observed velocity field (0= bad and 1=good)

Table 6.2: Summary of velocity field classification.

Name	Interaction signatures	Kinematic center	Rot. curve irregularity	Disp. map irregularity	Kinematics classification	Optical classification
HE0952–1552	no	no	yes	no	Distorted (mild)	Disk - undistorted
HE1019–1414	no	no	yes	yes	Distorted (mild)	Disk - distorted
HE1020–1022	-	-	-	-	Unclear	Spheroid - undistorted
HE1029–1401	yes	no	yes	no	Distorted (mild)	Spheroid - distorted
HE1043–1346	no	no	no	no	Regular	Disk - undistorted
HE1110–1901	-	-	-	-	Unclear	Spheroid - undistorted
HE1201–2409	no	no	yes	yes	Distorted (mild)	Spheroid - undistorted
HE1228–1637	no	no	yes	yes	Distorted (mild)	Spheroid - distorted
HE1237–2252	no	no	yes	yes	Distorted (mild)	Disk - distorted
HE1239–2426	no	no	no	no	Regular	Disk - undistorted
HE1254–0934	yes	yes	yes	yes	Distorted (strong)	Disk - distorted
HE1300–1325	yes	no	yes	yes	Distorted (strong)	Spheroid - distorted
HE1310–1051	yes	yes	yes	no	Distorted (strong)	Disk - distorted
HE1315–1028	-	-	-	-	Unclear	Disk - distorted
HE1335–0847	-	-	-	-	Unclear	Spheroid - undistorted
HE1338–1423	no	no	yes	no	Distorted (mild)	Disk - distorted
HE1405–1545	yes	no	no	no	Distorted (mild)	Disk - distorted
HE1416–1256	yes	no	no	yes	Distorted (mild)	Spheroid - undistorted
HE1434–1600	no	no	yes	yes	Distorted (mild)	Spheroid - distorted

DISCUSSION AND CONCLUSIONS

Galaxy merger has been proposed as one of the effective way to ignite AGN activity due to its efficiency in reducing angular momentum and bring gas to the center region. In this thesis we want to explore and investigate the importance of major merger for quasar fueling mechanism. A galaxy's morphology records the history of the galaxy, from the early time of formation until we observed it today and as a result of how the galaxy was affected by internal and external factors. The optical morphology represents only the distribution of stars within a galaxy. In order to study the gaseous par of the galaxy we have to either use very expensive radio observations for the cold gas or narrow band imaging or spectroscopy to study the warm gas components. With the presented integral-field spectroscopy data we didi the latter. Galaxy interactions can change the distribution of stars and gas. Stars and gas behave differently during an interaction because gas can respond to the pressure and friction not only to gravity as the stars. In order to get a complete picture of a galaxy's (recent) interaction history, it is advised to use imaging and spectroscopy data as two complementary approaches.

Building on our VIMOS IFS data, we complement this spectroscopy with imaging data collected from ground based observation (already analyzed by Jahnke et al. (2004a)) and also new Hubble telescope observations drawn from the HST archive. Main goal of this work is to investigate how to ignite quasar activity and importance of major merger as one of quasar fueling mechanism.

Our results provide preliminary answer to one of the main question on quasar fueling mechanism: Does major merger is the most dominant physical mechanisms to ignite quasar activity? We use advantages of spatially resolved capability of integral filed spectroscopy. We reported our data sample and observation in chapter 2. Data reduction and preparation to produce nuclear data cube and host galaxy data cube separately summarized in Chapter 3. We applied quasar – host galaxy decomposition method by previous study which is used for long slit spectroscopy to our integral field spectroscopy data. We added modification with iterative subtraction of host galaxy

contribution to the quasar spectrum. We checked our decomposition results using quasar host galaxy broad band photometry and examined whether broad line feature still left from quasar host galaxy spectrum. The results enable us to study spatially resolved quasar host galaxy properties for type 1 quasar and determine black hole parameters from quasar data cube.

We summarized our method to determine black hole parameters, physical conditions of the ionized gas and kinematics in chapter 3 and we reported our results into two chapters, black hole parameters and physical conditions of the ionized gas in Chapter 5 and kinematics properties of quasar host galaxies in Chapter 6. In this last chapter, we will elaborate our results and connect with main question which we would like to address as motivation for this work.

7.1 LINKING TOGETHER ALL RESULTS

To summarize, some important results from this work are:

1. We applied a quasar–host galaxy decomposition method to a sample of 19 type 1 quasars observed with the VIMOS IFU on the VLT. This enables us to study their spatially resolved host galaxy properties. We have also measured their supermassive black hole properties (such as black hole mass and Eddington ratio). For this we use as single epoch observation method with the $H\beta$ broad emission line and optical continuum. This allows a proper analysis and interpretation of distortion signatures as a function of black hole mass.
2. We characterized the kinematic properties of the host galaxy velocity field derived from their emission lines. We quantify distortion signatures on velocity field and construct classification scheme to distinguish between distortion classes respectively. Then, we compared distortion signatures between the imaging and kinematic parts of our study. We found that both generally consistent.
3. **Fraction of distorted galaxies in our sample is large.** Based on morphological study by Jahnke et al. (2004a), 62.5 % of our host galaxies classified as distorted galaxies and from our kinematics analysis, 68.75 % classified as distorted galaxies. According to our classification, majority are mildly distorted class and only three objects can be categorized strongly distorted class.
4. **Consistency of imaging data and integral field spectroscopy data.** Our conclusion drawn from comparing numbers and cases of undistorted/mildly/strongly distorted on kinematic side and imaging side. Ionized gas and stellar distribution can be different even though they located in the same gravitational potential. We found a good agreement for that both distributions. For some objects their distribution can be different for example

HE1029-1201 and HE 1416–1256 where from Hubble imaging data using WFPC2 camera we see only elliptical galaxies but from ionized gas maps we can see strong tidal tails. Possible explanations are stellar tidal tails are really faint hence not detected in imaging data. Both information are complementary for large scale perturbation. The difference also manifests on the classification of distorted or undistorted galaxy. As one of main goal of this thesis we construct a classification scheme for kinematics properties of or quasar host galaxies as described in chapter 4 and 6.

5. With the incidence of merger signatures now established, we test a possible relation between interaction state of the host galaxy and level of black hole accretion. **We found no significant impact of a galaxy’s interaction state on the quasar activity in our sample based on both imaging and kinematics analysis, as shown in Fig. 7.1.** We plot Eddington ratios as function of black hole mass with state and level of distortion as third parameter both from imaging and kinematics analysis. We found that in general there is no relation between black hole activity and host galaxies level of distortion within our quasar sample. Two objects at high mass end with high accretion rate are HE1029–1401 and HE1254–0934. HE1029–1401 is most luminous quasar in our sample and has shell-like structure at the outer part. Ionized gas distribution shows complex structure with bi-conic structure and arc structure in the outer part. One possible explanation is this host galaxy experienced minor merger. HE1254–0934 is clearly an ongoing major merger system with tidal features both in the imaging and ionized gas distribution and it has really complex velocity structure.

Comparison with two previous studies we mentioned before shows a difference. First, [Letawe et al. \(2007\)](#) used imaging data and radial velocity curves to characterize gravitational interaction for their sample and they reported that there were difference of quasar activity level due to gravitational interaction. Second study by [Dumas et al. \(2007\)](#) used imaging and a kinematical analysis of 2D velocity field from ionized gas and stellar components. Our quasars sample is located between the samples of [Dumas et al. \(2007\)](#) and [Letawe et al. \(2007\)](#) (in terms of redshift and AGN luminosity, see Fig. 2.1).

[Dumas et al. \(2007\)](#) investigated 7 pairs of Seyfert galaxies and a matched comparison sample inactive galaxy. From their kinematical analysis they reported that two out of seven Seyfert galaxies does not have phase angle misalignment between ionized gas and stellar component, indicates co-rotation behavior for majority. Some distortion features were also detected from velocity fields.

[Letawe et al. \(2007\)](#) sample consists of 20 bright low-redshift quasars. They conclude that the accretion rate is larger for the interacting system. It could be an over interpretation if we compare the accretion rate for interacting and non-interacting system from their sample. We also compare the accretion rates for the three samples. Accretion rate is one indication

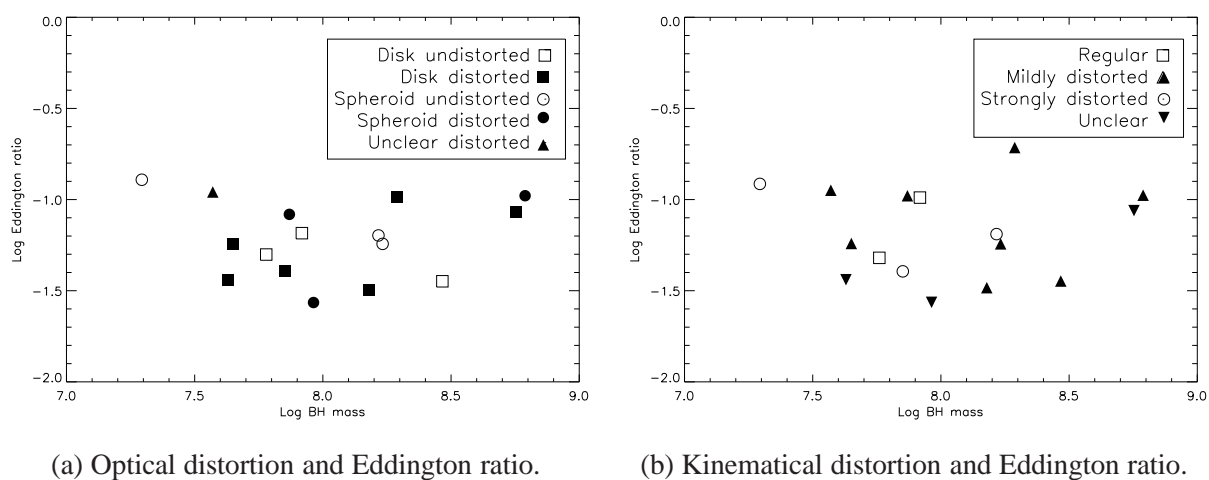


Figure 7.1: Accretion rate vs. distortion state and black hole mass for optical from images (**left**) and kinematical classification (**right**). **Left panel:** Squares represent disk dominated galaxies, circles represent bulge dominated galaxies and triangles for galaxies with unclear morphology. Filled symbols are for host galaxies with distortion signature and empty symbols for undistorted host galaxies. **Right panel:** Squares represents regular velocity fields, triangle distorted velocity fields, where ordinary triangles stand for mildly distorted galaxies and upside down triangles for strongly disturbed galaxies and circles for unclear cases. It is obvious from both classifications that there is no dependency of accretion rate on neither black hole mass nor distortion state. All quasars, independent of their distortion state accrete at a few percent of their Eddington rate.

	Distorted/Interacting	Undistorted/Non-interacting
Dumas et al. (2007)	$1.94 \times 10^{-3} \pm$	$3.78 \times 10^{-6} \pm$
This work	0.34 ± 0.12	0.09 ± 0.03
Letawe et al. (2007)	1.11 ± 0.77	0.67 ± 0.39

Table 7.1: Comparison of accretion rates for interacting and non-interacting system based on our work with Dumas et al. (2007) and Letawe et al. (2007) results.

of black hole activity and we can determine using the following formula:

$$\dot{M} = \frac{L_{bol}}{\eta c^2}, \quad (7.1)$$

Where \dot{M} is mass accretion rate, L_{bol} is bolometric luminosity, c is speed of light and η is efficiency factor. We assume efficiency factor 0.1 same with other two works. We summarize mass accretion rate which we already computed in Table 7.1. Within the error bars accretion rates for Letawe et al. (2007) sample are comparable, the same case also with our sample. Hence, implies there is no dependency of black hole activity with state of interaction of the host galaxy.

The complementary approach to interpret our results is to compare to numerical simulations. Unfortunately we are limited by only a small number of available galaxy merger simulations. This approach in principle requires a large number of simulations which can be modified and followed over cosmological time scales. An example of how successful this approach can be is work by Green et al. (2010) who required to perform ~ 200 simulations to achieved a suitable match for observational data of a binary quasar. From their comparison they can derive the properties of the progenitor galaxies for that particular merging system and followed all physical processes during the merging sequence such as star formation and black hole growth.

For our work, we set a less ambitious goal than Green et al. (2010). We would like to utilize an existing numerical simulation to determine in which phase of a merger sequence our quasar host galaxies could be situated. We adopt the quantitative merger phase classification by Lotz et al. (2008) with their six merger steps: pre-merger, first pass, maximal separation, final merger, post-merger, merger remnant, defining all important phase of the merger process. For this work, It will be impossible to make a direct quantitative assessment of time scales at the moment, hence we divide merger process only into three phases: pre-merger (where two galaxies still separate), final merger (two nuclei merge) and post-merger (relaxation process).

We compare imaging data and kinematic properties which we presented in Chapter 6 with a representative numerical simulation of major merger of two gas rich disc galaxies shown in

Fig. 7.2 below. Under the assumption, that all or quasar would be in a merger process, 18% host galaxies would be classified from their visual and kinematical appearance as pre-merger, 29% as final merger and the remaining 53% as in post-merger phase. This suggests that most of our quasar host galaxies are not in the situation where their nuclei merge to form a more massive black hole and where the simulation claims the quasar activity to be in its most active phase. Most of our quasar host galaxies show less signature of distortion and would be in pre-merger phase or post merger phase. For this interpretation, we have to consider gravitational interaction signature lifetimes. Signature of gravitational interaction can disappear after a few rotation cycles < 1 Gyr (Kronberger et al. 2006), which is long compared to typical quasar life times, hence our interpretation would be unaffected by this disappearance.

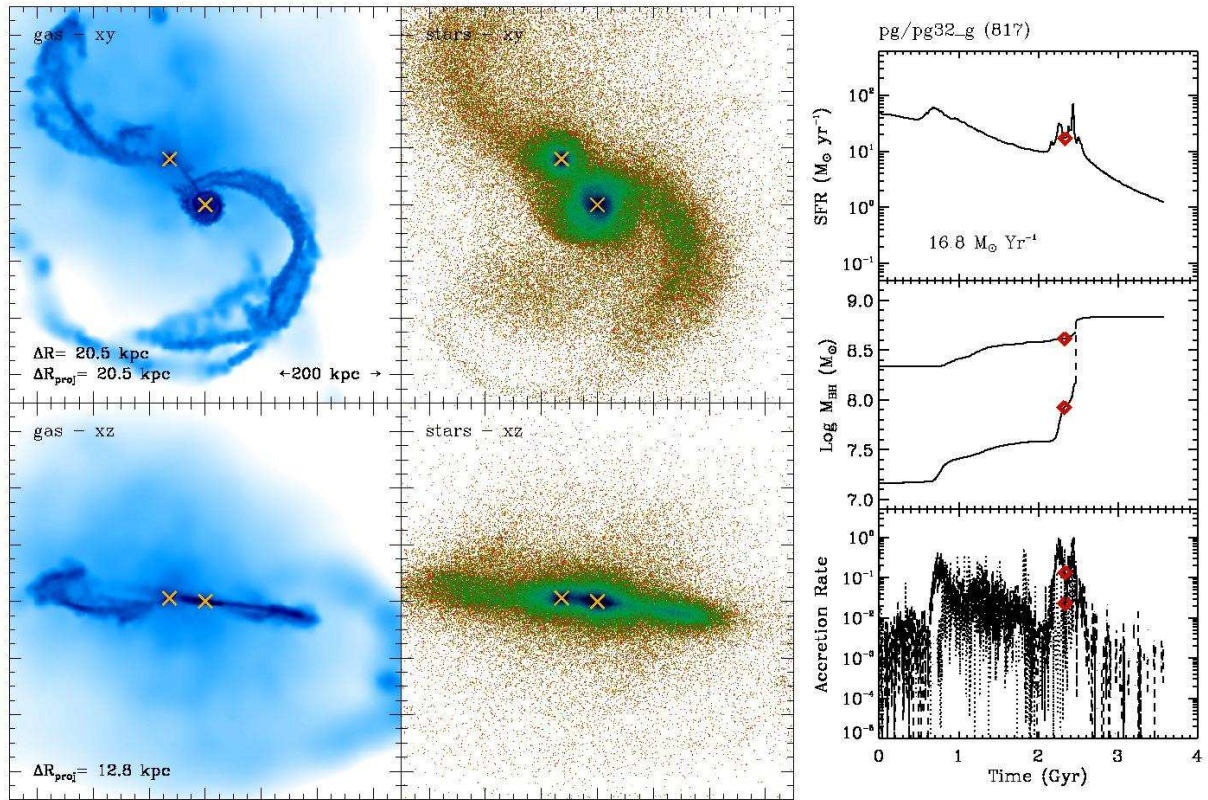


Figure 7.2: One example of matching experiment by (Green et al. 2010). Crosses indicates QSO position. First column displays gas distribution and second column stars distribution. Of this four panels, first row and second row are different in orientation. The last column shows star formation rate, black hole mass and accretion rate as a function of time. Red diamond symbols represent phase where snapshots of previous columns happened.

However, galaxies merging is a complex physical mechanism and observational data only take a "snapshot" image. Ideally, we would like to know the history of a merging or also non-merging

galaxies and how its physical properties change with time. Numerical simulation can in principle provide this insight and there have been rapid development in this field since the famous paper by Toomre & Toomre (1972). Here we list some parameters which centrally shaping the progression of the merger process:

1. Mass ratio of the progenitor galaxies. This defines a merger process as a major merger (mass ratio larger than 1:3) or minor merger (mass ratio less than 1:3).
2. Gas content of progenitor galaxies. Gas is a major component of a galaxy and is dissipational. Gas behaviour during a major merger will be different to pure dark matter and stars which are both collisionless, resulting different physical processes.
3. Progenitor galaxy structure (pure disk galaxy or disk galaxy with bulge).
4. Orbital geometry (prograde or retrograde encounter)
5. Orbital parameters, such as eccentricity

Some caveats of our approach:

1. Merger history of a galaxy. We do not have the record how many merger a galaxy experience since its formation. Merger history and fraction papers.
2. End results of this numerical simulation is an early type galaxy. Disk survival
3. Different regimes of black hole mass and mass accretion rate.
4. Finally, on the empirical side, the available imaging data quality.

Regarding the big picture about how to ignite nuclear activity, our results provides pieces of puzzle because our observation only probe kpc scale whereas to have better understanding of what and how physical mechanisms which can fuel nuclear activity we have to probe until smaller scale (event horizon of the supermassive black hole). Nevertheless, there are (possible) connection for what we observed at large scale with smaller physical scale. Hopkins & Quataert (2010) showed self sustained structure (structure within structure) from numerical simulation. This structure within structure mechanisms can bring gas from kpc scale until 0.1 pc. The ultimate goal is to probe various physical scale and every possible physical mechanisms and following with time if it is possible.

In summary, even the comparison with this single numerical simulations shows that it is highly unlikely that all or majority of our quasars is currently in the most intense part of merger induced

black hole accretion, making a merger-triggering unlikely. Again, this is fully consistent with our finding in number 5 mentioned before. We draw the conclusion: Major mergers are not the dominating trigger for black hole growth in our sample.

7.2 CONCLUDING REMARKS AND FUTURE OUTLOOK

We have presented the analysis of a spatially resolved kinematics study of quasar host galaxies at redshift < 0.2 . We also designed a classification scheme in order to classify velocity field of the host galaxies to distinguish between distorted and regular velocity fields. The study shows that the majority of the sample type 1 quasar host galaxies have distorted velocity field, though mostly mildly distorted, and in general the classification is consistent with the impression from a morphological study for the same objects. But, for some objects there are partially substantial features which are not exist in the optical imaging when compared with emission line flux maps and its velocity fields.

The work presented here immediately suggests future follow up for further investigation and improvement. On the observation side, we suggest to construct a comparison sample of inactive galaxies with similar properties (z , L , M) also to be observed with integral field spectroscopy. Our conclusion here are based only on quasar host galaxies and we still do not know whether the frequency of mergers as indicated by distortion signatures, based on imaging and kinematics data, is similar for a matched inactive galaxy sample. Conclusion drawn from a comparison between quasar host galaxies and inactive galaxies will have a substantially stronger foundation compared to quasar host galaxies studies alone. A beautiful example is shown by (Cisternas et al. 2011) who present a study of type-1 AGNs and their matched comparison sample, using imaging data. They found that there is no significant difference of the merger fractions for active and inactive galaxies with similar physical properties. Their result has an important implication for the physics of AGN fueling mechanism because they showed that major mergers is not the main mechanism to ignite nuclear activity at $0.3 < z < 1.0$. If we only use the merger fraction from active host galaxies alone we cannot directly conclude whether major mergers are an important physical process to ignite AGN or not. In order to achieve firmer conclusions, we suggest to construct our own comparison sample, if publicly available integral field spectroscopy data sets are not sufficient as we assume.

From the numerical simulation side regarding matching experiments of observational data and simulations of merging galaxies. We referred before to the work by (Green et al. 2010) who did a quantitative analysis of galaxy merger and potential black hole growth. At the moment, this would be ideal as the type of comparison data we could use but we have limited resource for our own major merger simulations. In the future, we suggest to use dedicated matching simulations

for every single host galaxy, if it possible, in order to investigate also the time evolution of merging system and the history of our sample objects – at least a potential history.

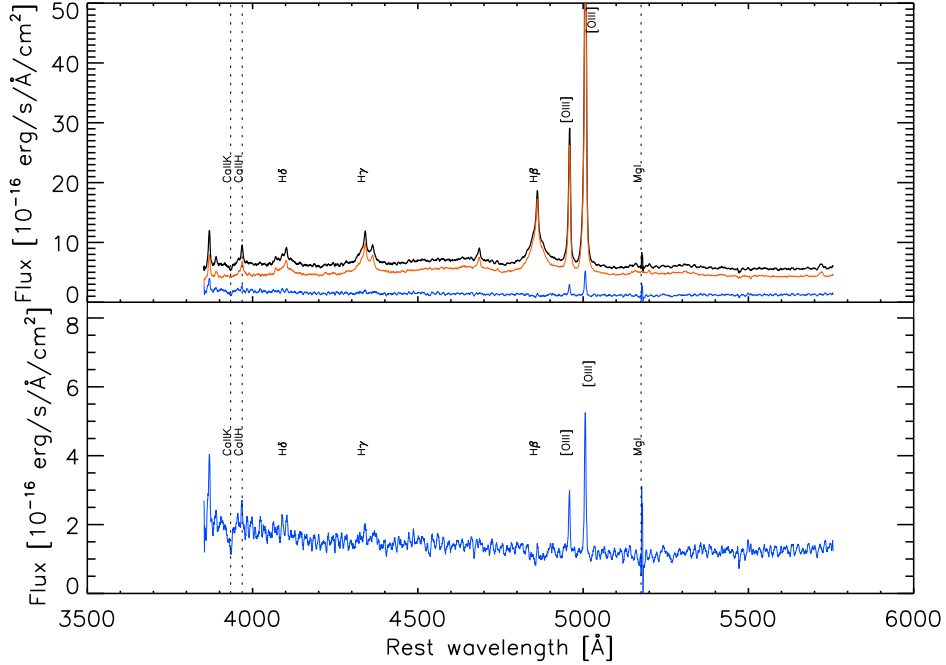
This work is not yet complemented with spatially resolved stellar population information. Stellar population analysis can be important diagnostic for the past development of our galaxies. In theory, age dating of past starburst episodes concurrent with a major merger is possible, however a detailed analysis was, given the data quality and volume, beyond the scope of this work.

Adding and combining the knowledge obtained from this and past work with future studies will allow to contribute for answering some questions which we addressed in the: how do black hole grow inside galaxies and how do they impact to the galaxy evolution? In this work, we have at least shown introduction chapter in order to have a good and better knowledge of active galactic nuclei in particular and galaxies in general.

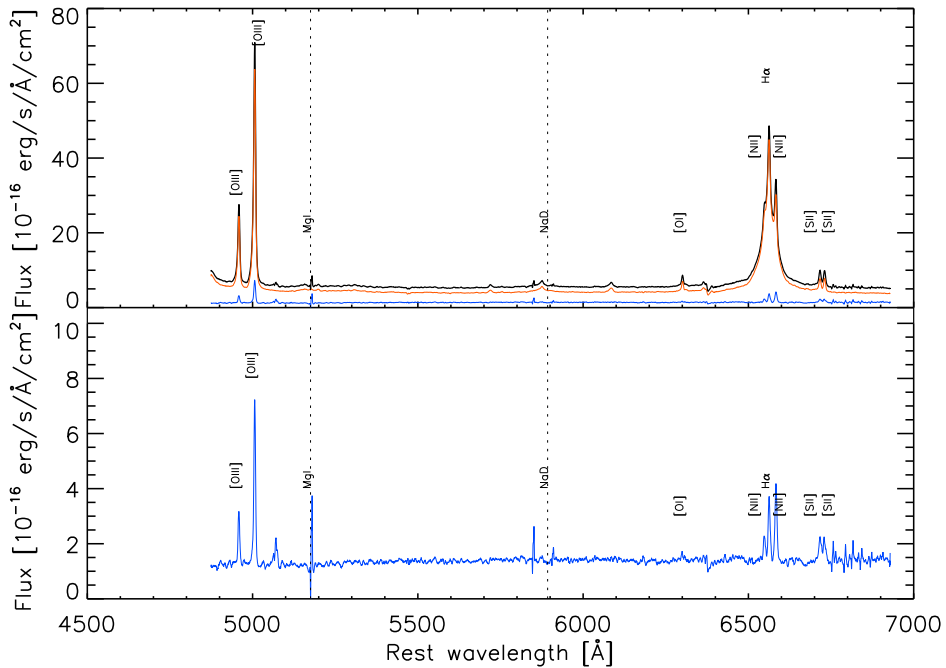
A

APPENDIX A: RESULTS OF THE QUASAR – HOST GALAXY DECOMPOSITION

The following figures document the quality and level of decomposition of quasar and host galaxy light for our sample, as a result of the method described in section 3.3. For each object the coadded spectrum of spaxels within 5 pixels radius is shown. Black: total spectrum, red: nuclear/quasar, blue: host galaxy. The host galaxy is shown again as zoomed-in version in the bottom of each plot.

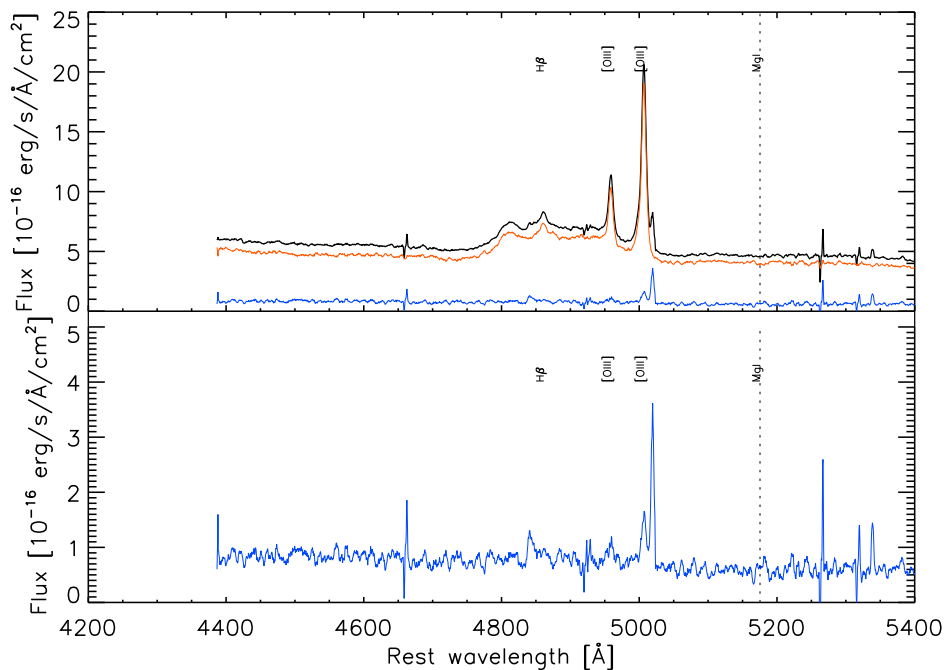


(a) Spectrum of HE1019–1414 shows $H\beta$ and [OIII] complex.

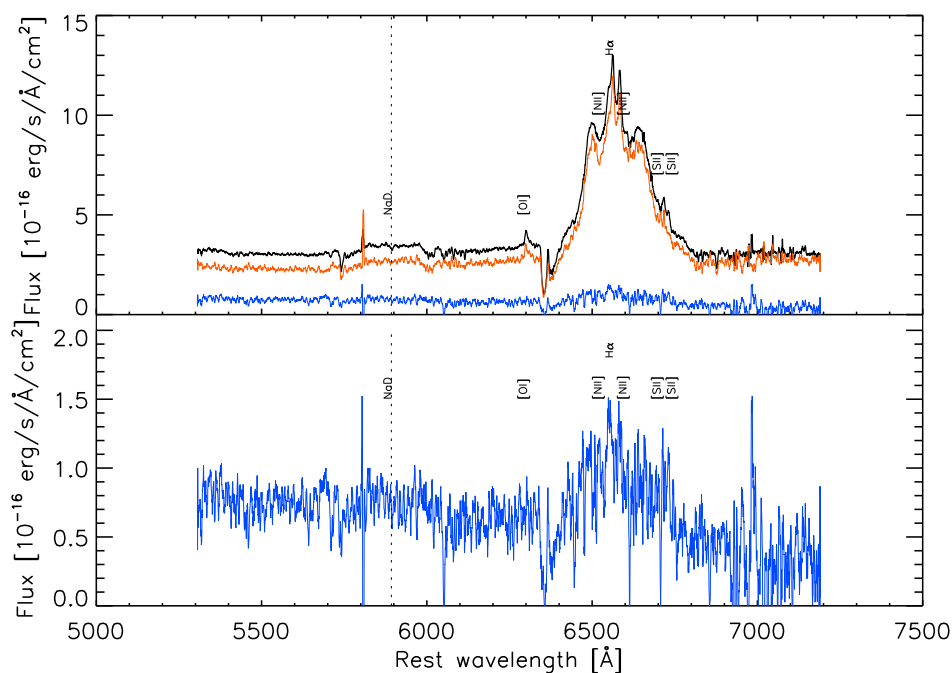


(b) Spectrum of HE1019–1414 shows $H\alpha$ + [N II] complex.

Figure A.1: Quasar – host galaxy decomposition method for HE 1019–1414. (a) Spectrum with $H\beta$ and [OIII] complex. (b) spectrum with $H\alpha$ + [N II] complex. Black: original spectrum, red: scaled nucleus spectrum, blue: host galaxy spectrum without broad-line emission. We show the host galaxy spectrum alone in the bottom panel for each figure for clarity.

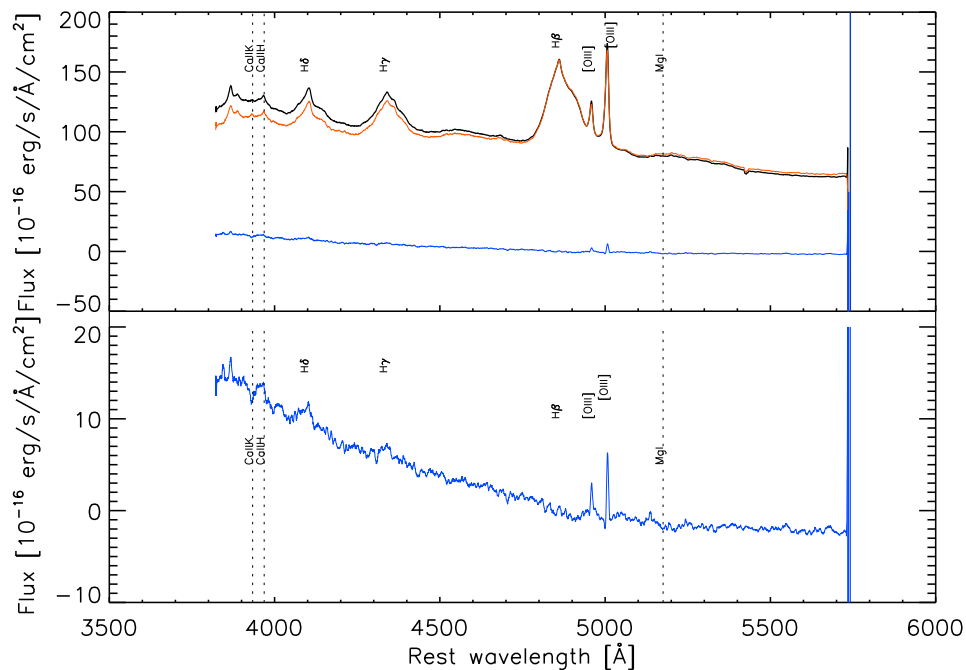


(a) Spectrum of HE 1020–1022 shows $H\beta$ and [OIII] complex.

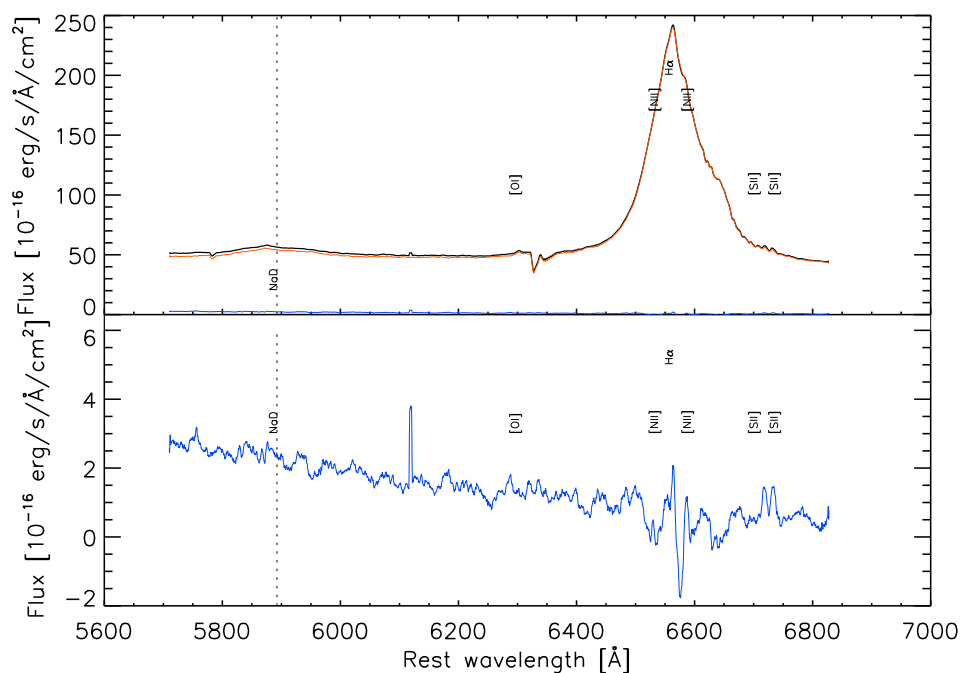


(b) Spectrum of HE 1020–1022 shows $H\alpha$ + [N II] complex.

Figure A.2: Quasar – host galaxy decomposition method for HE 1020–1022. (a) Spectrum with $H\beta$ and [OIII] complex. (b) spectrum with $H\alpha$ + [N II] complex. Black: original spectrum, red: scaled nucleus spectrum, blue: host galaxy spectrum without broad-line emission. We show the host galaxy spectrum alone in the bottom panel for each figure for clarity.

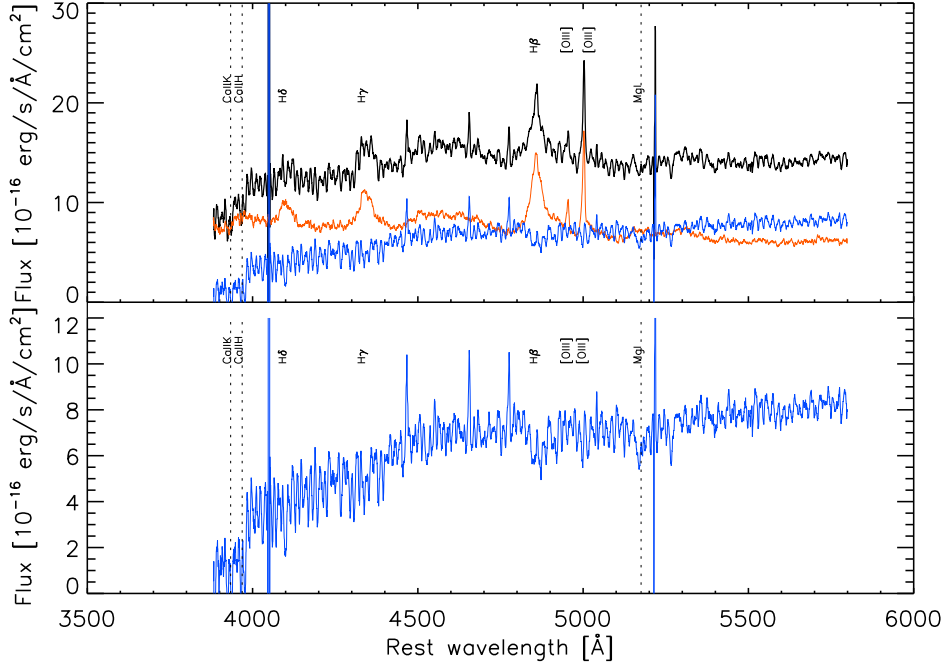


(a) Spectrum of HE 1029–1401 shows H β and [OIII] complex.

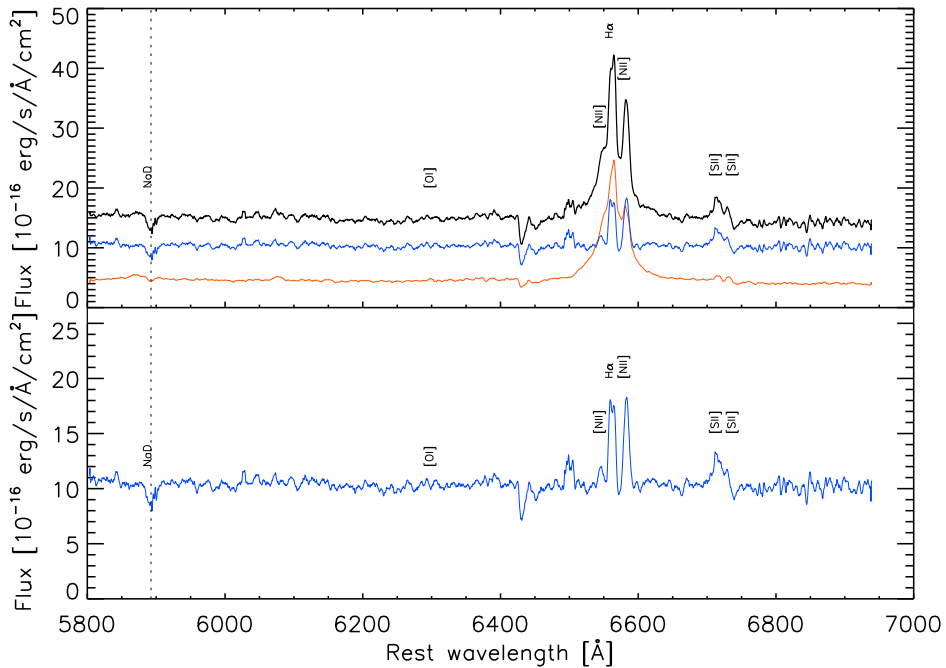


(b) Spectrum of HE HE 1029–1401 shows H α + [N II] complex.

Figure A.3: Quasar – host galaxy decomposition method for HE 1029–1401. (a) Spectrum with H β and [OIII] complex. (b) spectrum with H α + [N II] complex. Black: original spectrum, red: scaled nucleus spectrum, blue: host galaxy spectrum without broad-line emission. We show the host galaxy spectrum alone in the bottom panel for each figure for clarity.

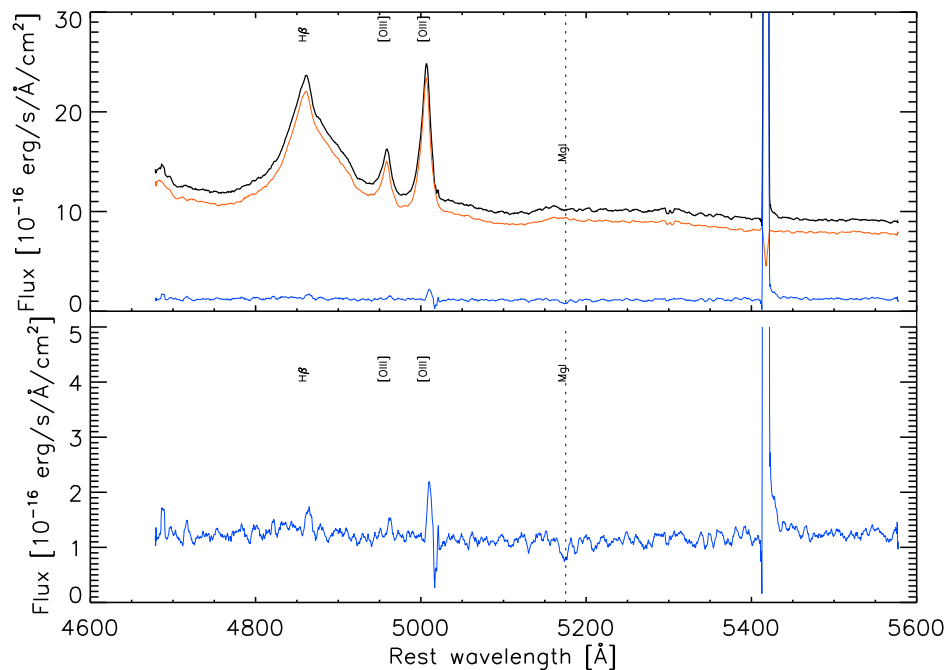


(a) Spectrum of HE 1043–1346 shows $H\beta$ and [OIII] complex.

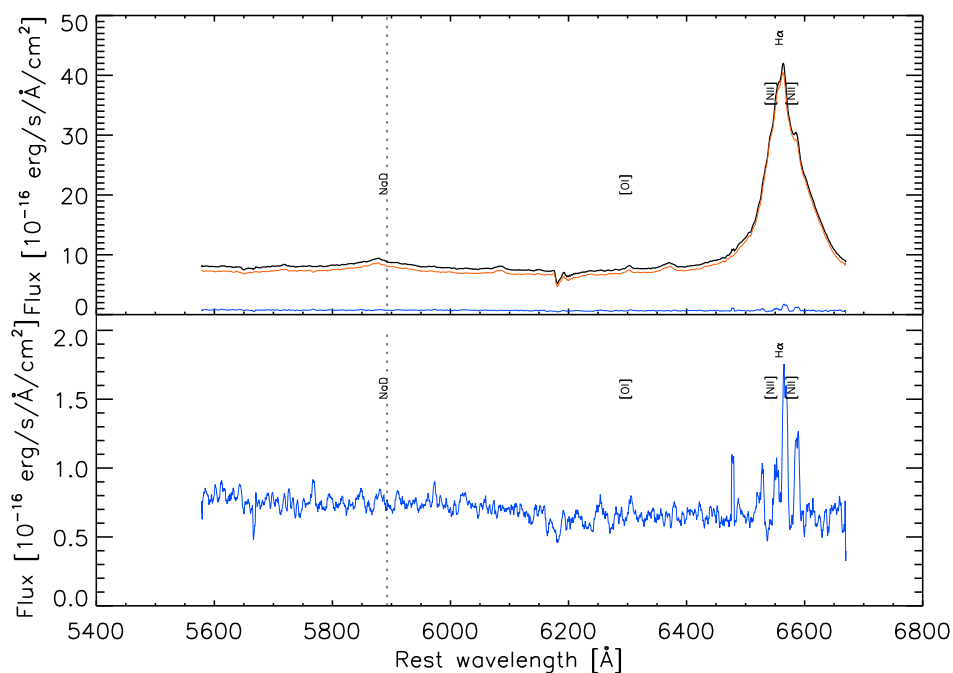


(b) Spectrum of HE 1043–1346 shows $H\alpha$ + [N II] complex.

Figure A.4: Quasar – host galaxy decomposition method for HE 1043–1346. (a) Spectrum with $H\beta$ and [OIII] complex. (b) spectrum with $H\alpha$ + [N II] complex. Black: original spectrum, red: scaled nucleus spectrum, blue: host galaxy spectrum without broad-line emission. We show the host galaxy spectrum alone in the bottom panel for each figure for clarity.

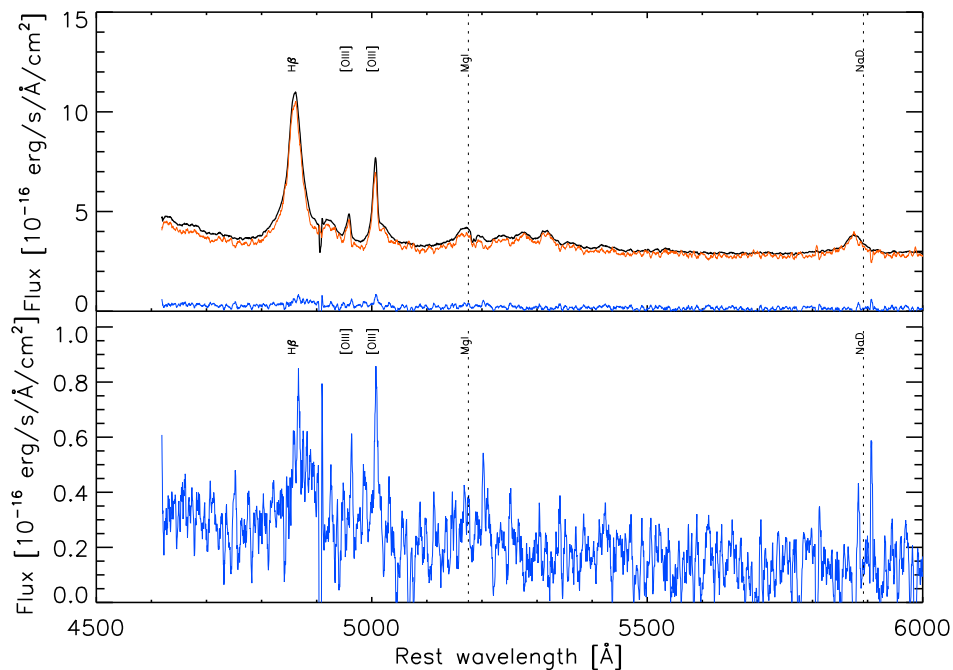


(a) Spectrum of HE 1110–1910 shows $H\beta$ and [OIII] complex.

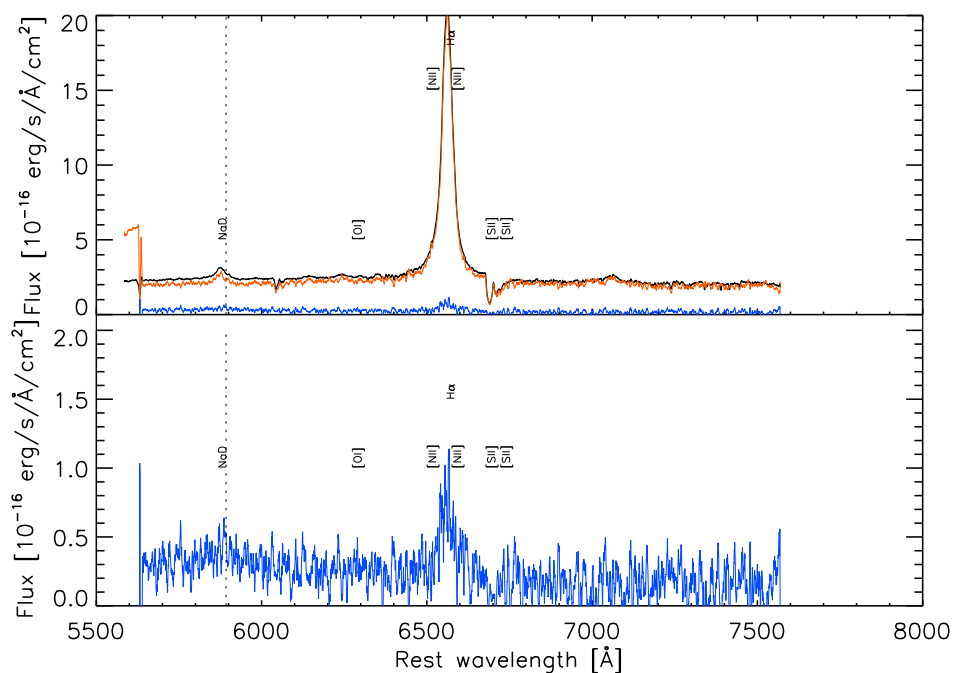


(b) Spectrum of HE 1110–1910 shows $H\alpha$ + [N II] complex.

Figure A.5: Quasar – host galaxy decomposition method for HE 1110–1910. (a) Spectrum with $H\beta$ and [OIII] complex. (b) spectrum with $H\alpha$ + [N II] complex. Black: original spectrum, red: scaled nucleus spectrum, blue: host galaxy spectrum without broad-line emission. We show the host galaxy spectrum alone in the bottom panel for each figure for clarity.

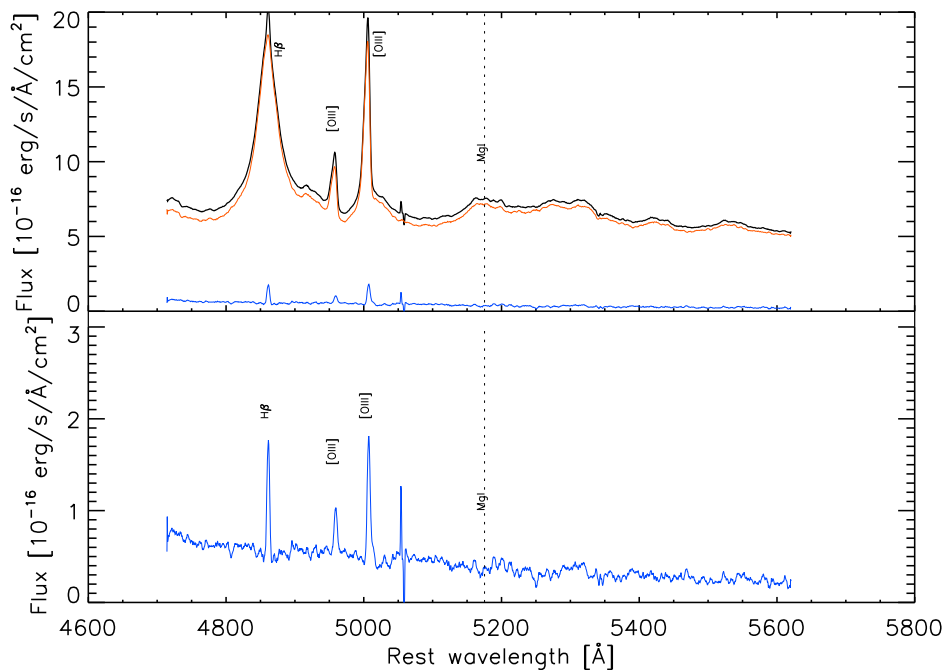


(a) Spectrum of HE 1201–2408 shows $H\beta$ and [OIII] complex.

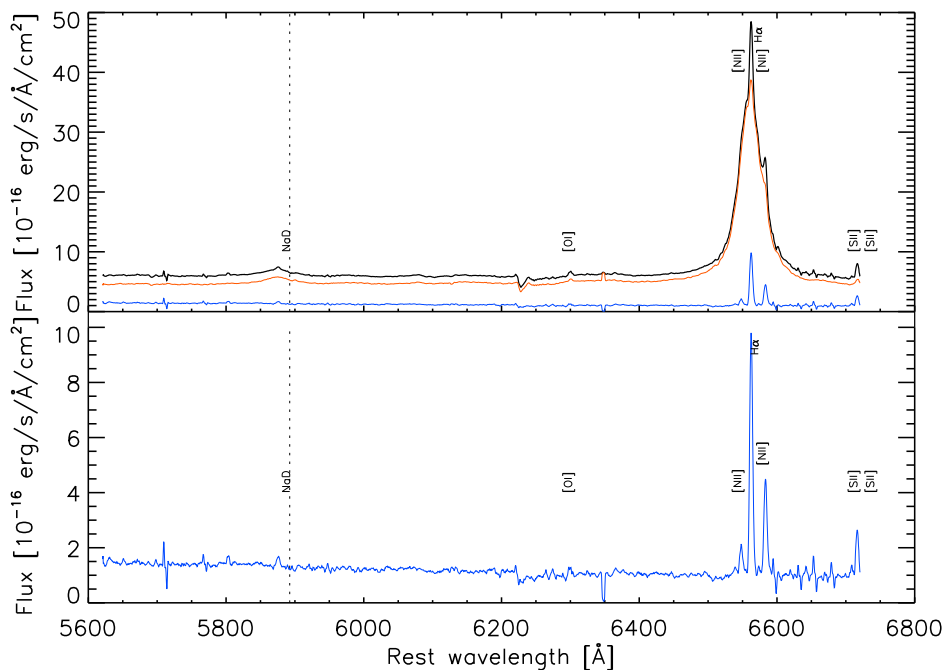


(b) Spectrum of HE 1201–2408 shows $H\alpha$ + [N II] complex.

Figure A.6: Quasar – host galaxy decomposition method for HE 1201–2408. (a) Spectrum with $H\beta$ and [OIII] complex. (b) spectrum with $H\alpha$ + [N II] complex. Black: original spectrum, red: scaled nucleus spectrum, blue: host galaxy spectrum without broad-line emission. We show the host galaxy spectrum alone in the bottom panel for each figure for clarity.

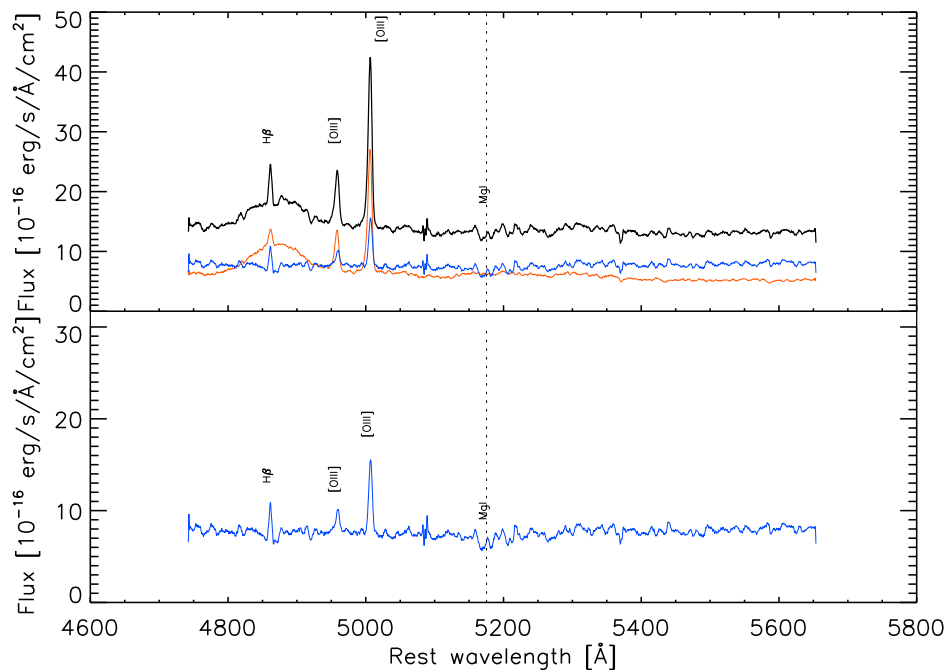


(a) Spectrum of HE 1228–1637 shows $H\beta$ and [OIII] complex.

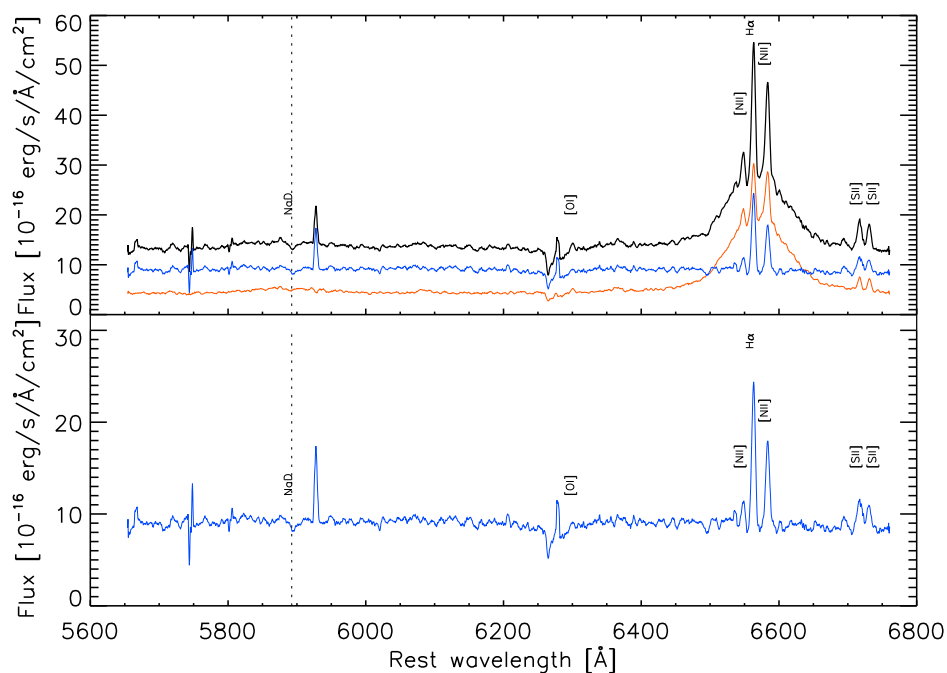


(b) Spectrum of HE 1228–1637 shows $H\alpha$ + [N II] complex.

Figure A.7: Quasar – host galaxy decomposition method for HE 1228–1637. (a) Spectrum with $H\beta$ and [OIII] complex. (b) spectrum with $H\alpha$ + [N II] complex. Black: original spectrum, red: scaled nucleus spectrum, blue: host galaxy spectrum without broad-line emission. We show the host galaxy spectrum alone in the bottom panel for each figure for clarity.

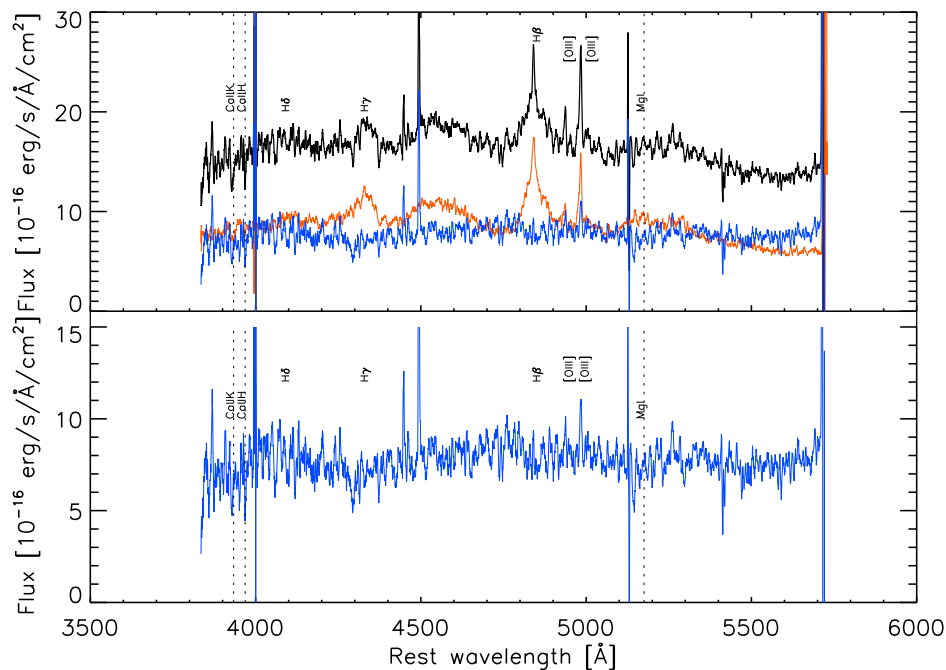


(a) Spectrum of HE 1237–2252 shows $H\beta$ and [OIII] complex.

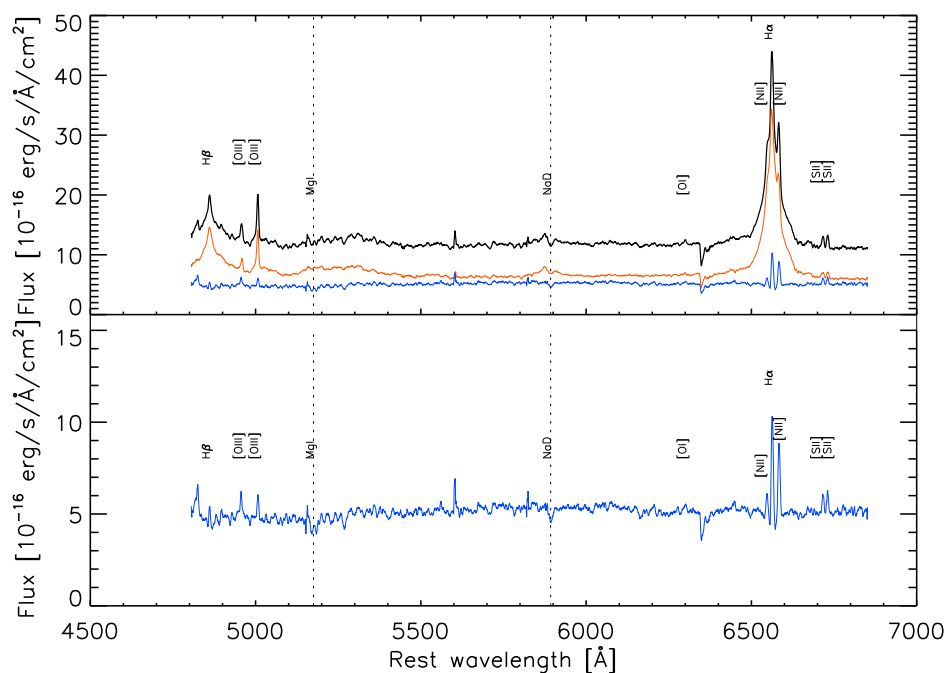


(b) Spectrum of HE 1237–2252 shows $H\alpha$ + [N II] complex.

Figure A.8: Quasar – host galaxy decomposition method for HE 1237–2252. (a) Spectrum with $H\beta$ and [OIII] complex. (b) spectrum with $H\alpha$ + [N II] complex. Black: original spectrum, red: scaled nucleus spectrum, blue: host galaxy spectrum without broad-line emission. We show the host galaxy spectrum alone in the bottom panel for each figure for clarity.

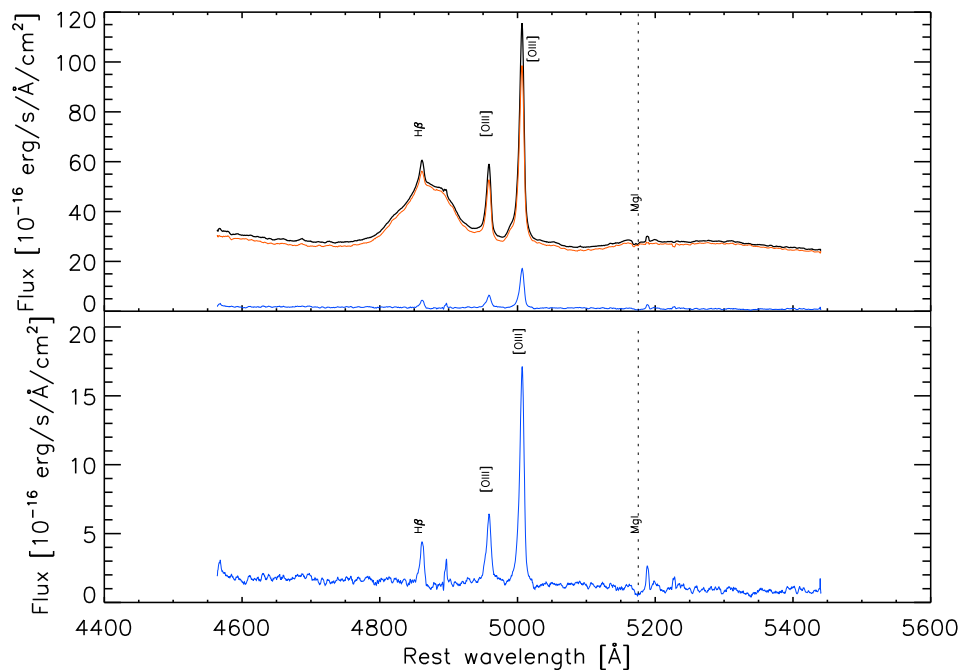


(a) Spectrum of HE 1239–2426 shows $H\beta$ and [OIII] complex.

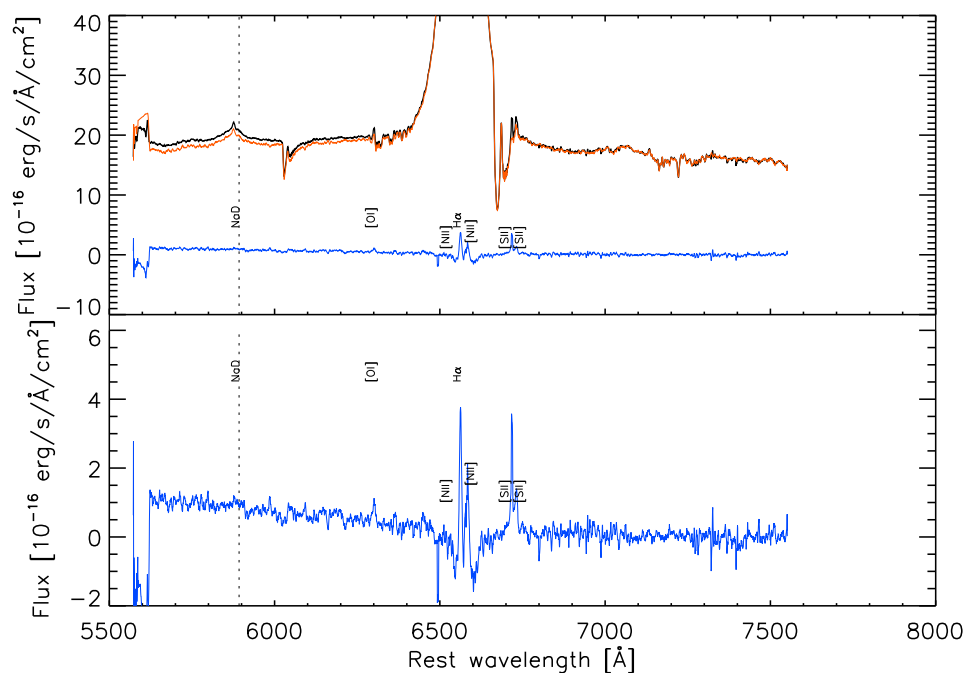


(b) Spectrum of HE 1239–2426 shows $H\alpha$ + [N II] complex.

Figure A.9: Quasar – host galaxy decomposition method for HE 1239–2426. (a) Spectrum with $H\beta$ and [OIII] complex. (b) spectrum with $H\alpha$ + [N II] complex. Black: original spectrum, red: scaled nucleus spectrum, blue: host galaxy spectrum without broad-line emission. We show the host galaxy spectrum alone in the bottom panel for each figure for clarity.

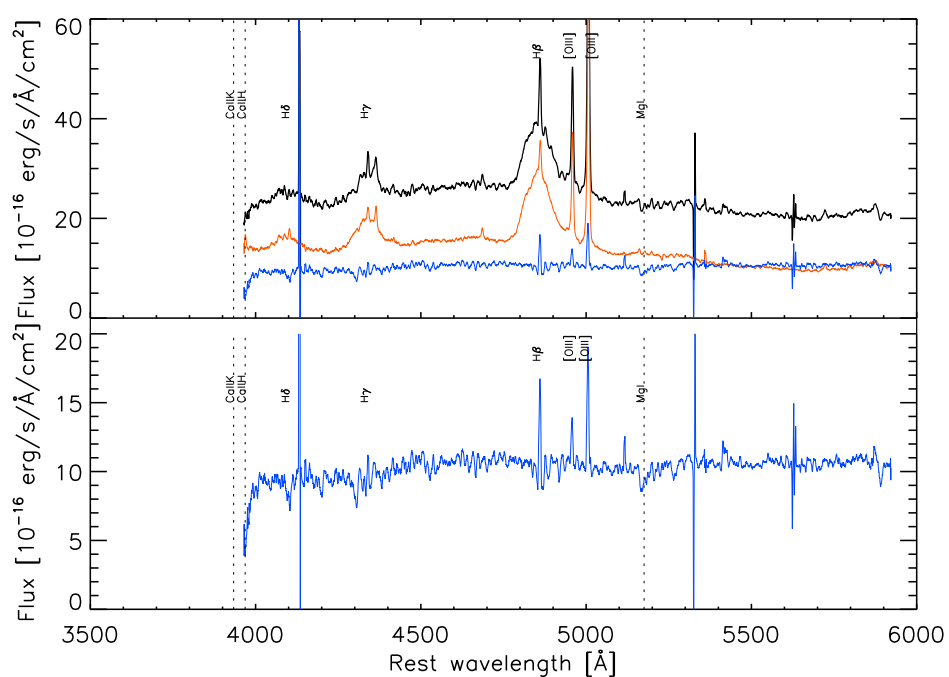


(a) Spectrum of HE 1254–0934 shows $H\beta$ and [OIII] complex.



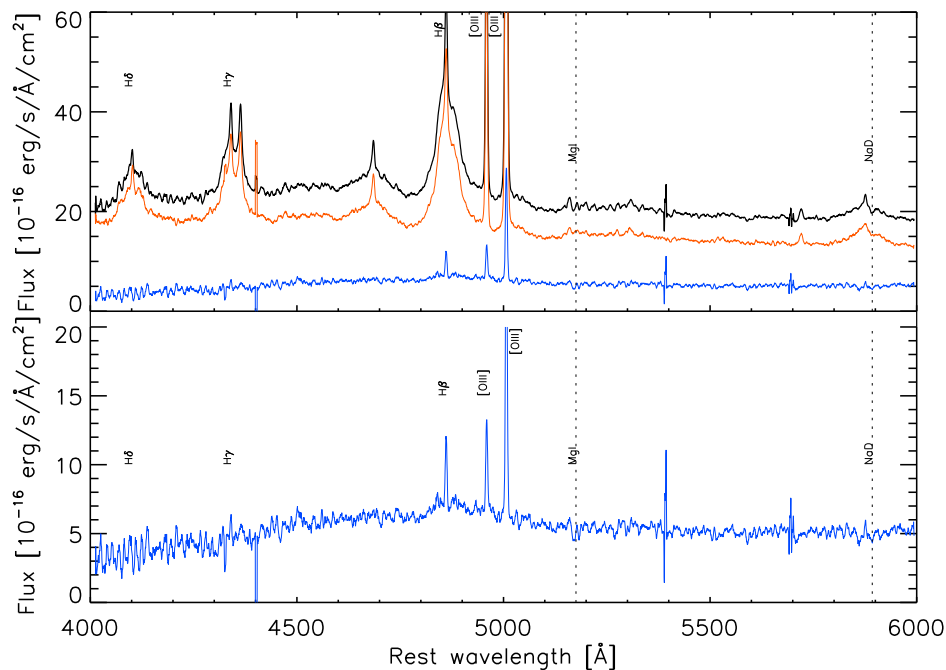
(b) Spectrum of HE 1254–0934 shows $H\alpha$ + [N II] complex.

Figure A.10: Quasar – host galaxy decomposition method for HE 1254–0934. (a) Spectrum with $H\beta$ and [OIII] complex. (b) spectrum with $H\alpha$ + [N II] complex. Black: original spectrum, red: scaled nucleus spectrum, blue: host galaxy spectrum without broad-line emission. We show the host galaxy spectrum alone in the bottom panel for each figure for clarity.

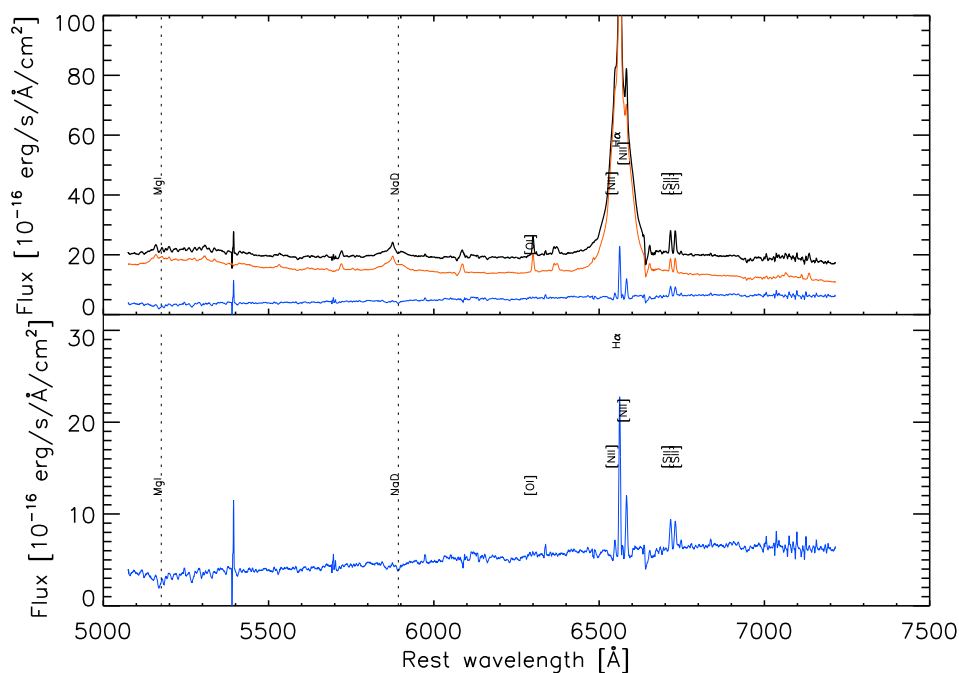


(a) Spectrum of HE1300–1325 shows H β and [OIII] complex.

Figure A.11: Quasar – host galaxy decomposition method for HE1300–1325. (a) Spectrum with H β and [OIII] complex. (b) spectrum with H α + [N II] complex. Black: original spectrum, red: scaled nucleus spectrum, blue: host galaxy spectrum without broad-line emission. We show the host galaxy spectrum alone in the bottom panel for each figure for clarity.

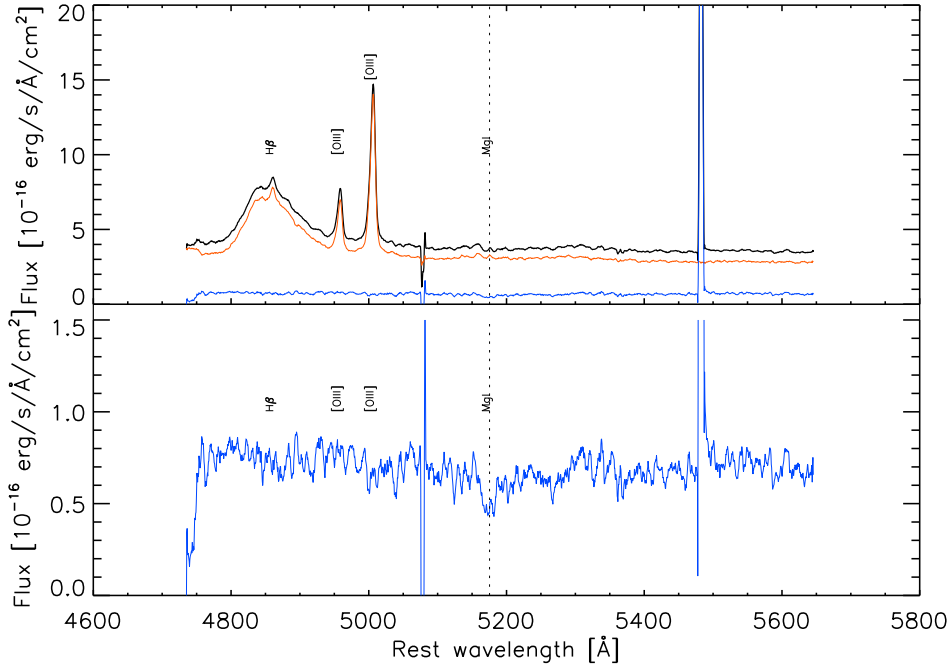


(a) Spectrum of HE 1310–1051 shows $H\beta$ and [OIII] complex.

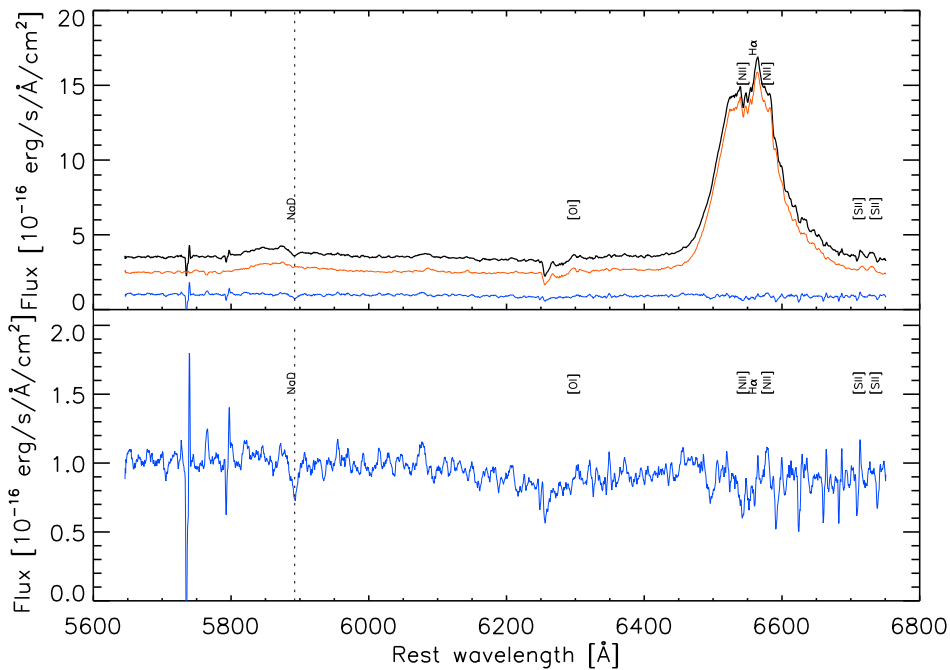


(b) Spectrum of HE 1310–1051 shows $H\alpha$ + [N II] complex.

Figure A.12: Quasar – host galaxy decomposition method for HE 1310–1051. (a) Spectrum with $H\beta$ and [OIII] complex. (b) spectrum with $H\alpha$ + [N II] complex. Black: original spectrum, red: scaled nucleus spectrum, blue: host galaxy spectrum without broad-line emission. We show the host galaxy spectrum alone in the bottom panel for each figure for clarity.

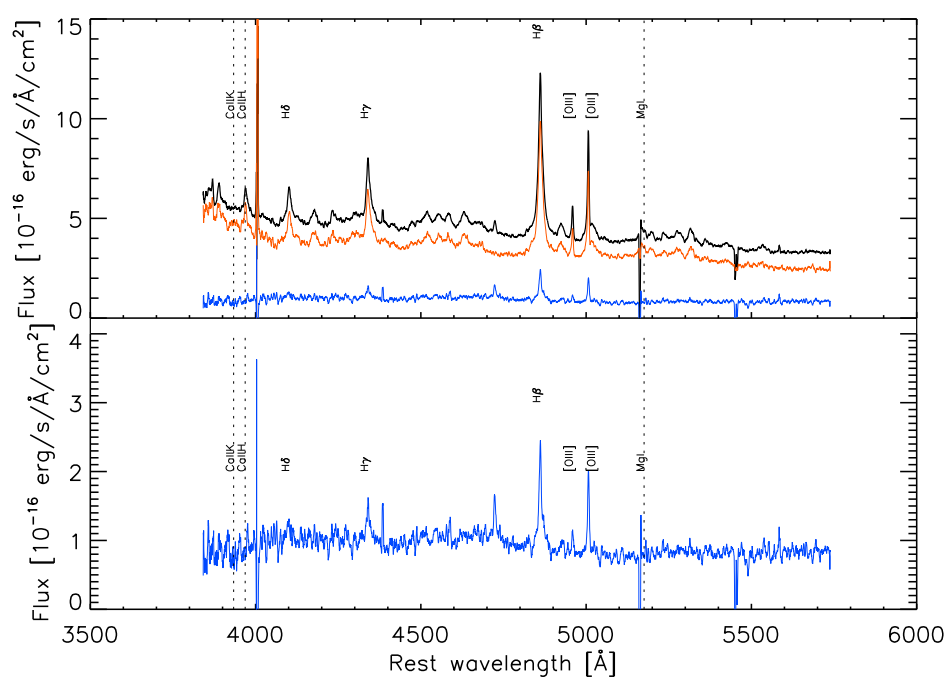


(a) Spectrum of HE 1315–1028 shows $H\beta$ and [OIII] complex.



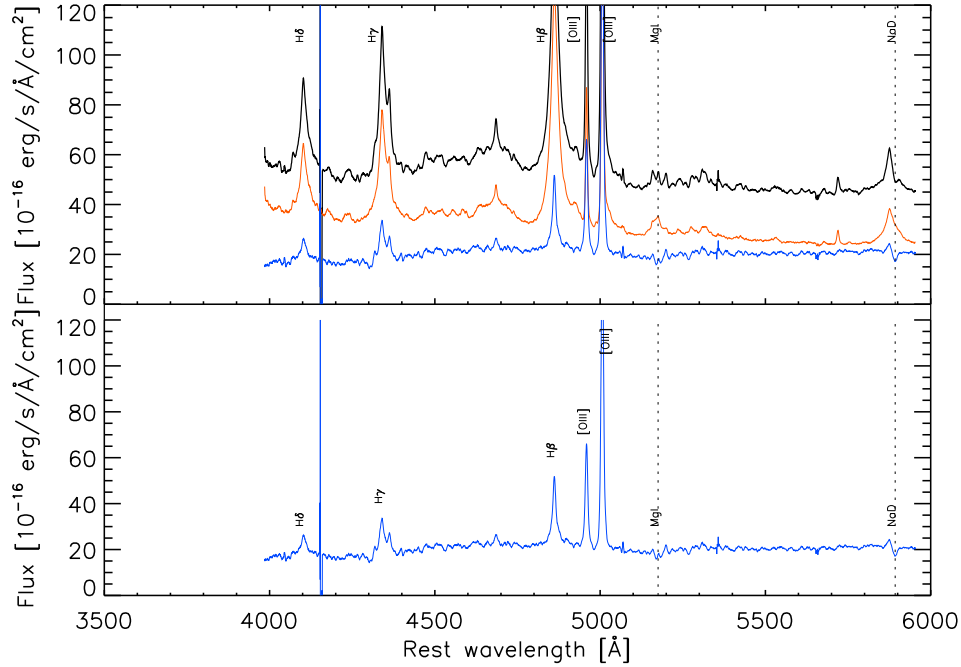
(b) Spectrum of HE 1315–1028 shows $H\alpha$ + [N II] complex.

Figure A.13: Quasar – host galaxy decomposition method for HE 1315–1028. (a) Spectrum with $H\beta$ and [OIII] complex. (b) spectrum with $H\alpha$ + [N II] complex. Black: original spectrum, red: scaled nucleus spectrum, blue: host galaxy spectrum without broad-line emission. We show the host galaxy spectrum alone in the bottom panel for each figure for clarity.

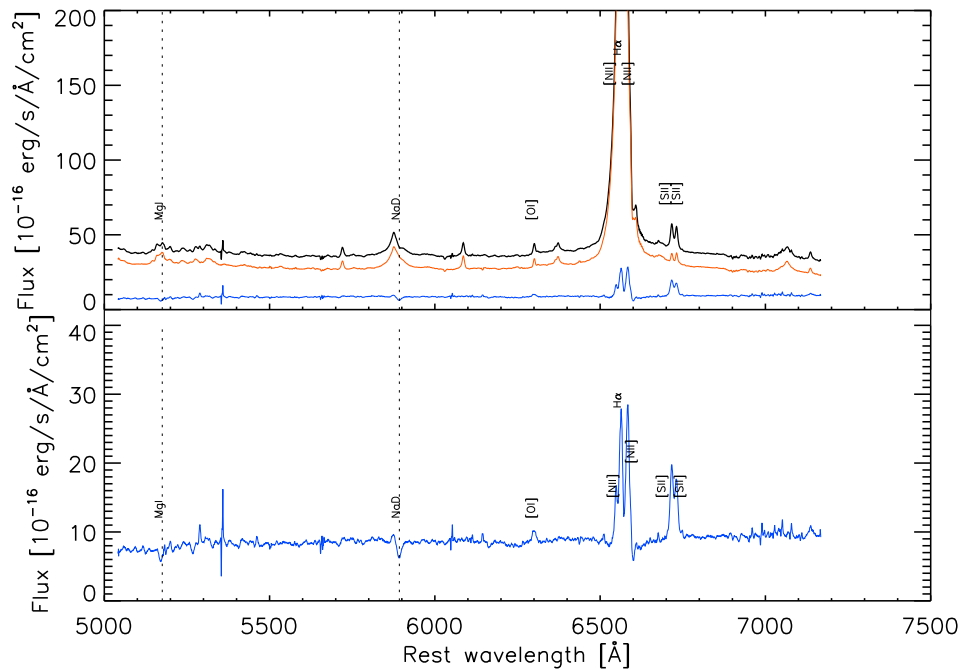


(a) Spectrum of HE 1335–0847 shows H β and [OIII] complex.

Figure A.14: Quasar – host galaxy decomposition method for HE 1335–0847. (a) Spectrum with H β and [OIII] complex. (b) spectrum with H α + [N II] complex. Black: original spectrum, red: scaled nucleus spectrum, blue: host galaxy spectrum without broad-line emission. We show the host galaxy spectrum alone in the bottom panel for each figure for clarity.

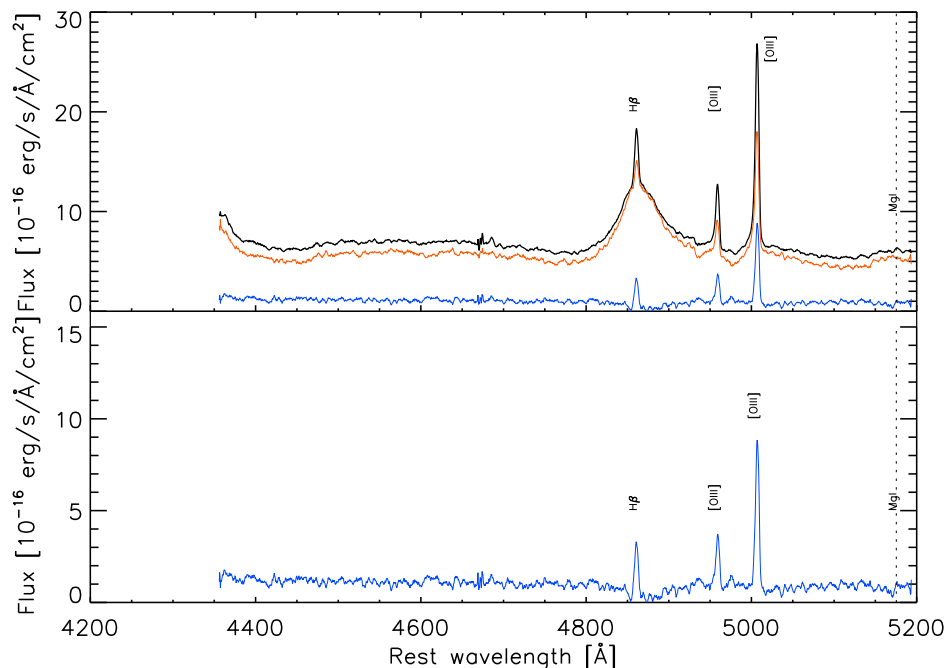


(a) Spectrum of HE 1338–1423 shows $H\beta$ and [OIII] complex.

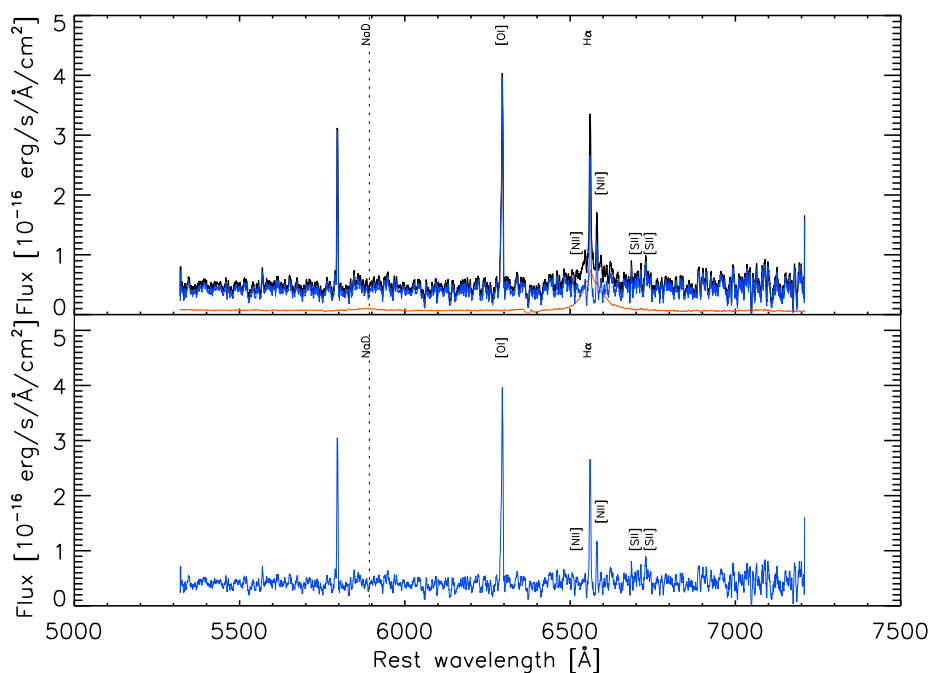


(b) Spectrum of HE 1338–1423 shows $H\alpha$ + [N II] complex.

Figure A.15: Quasar – host galaxy decomposition method for HE 1335–0847. (a) Spectrum with $H\beta$ and [OIII] complex. (b) spectrum with $H\alpha$ + [N II] complex. Black: original spectrum, red: scaled nucleus spectrum, blue: host galaxy spectrum without broad-line emission. We show the host galaxy spectrum alone in the bottom panel for each figure for clarity.

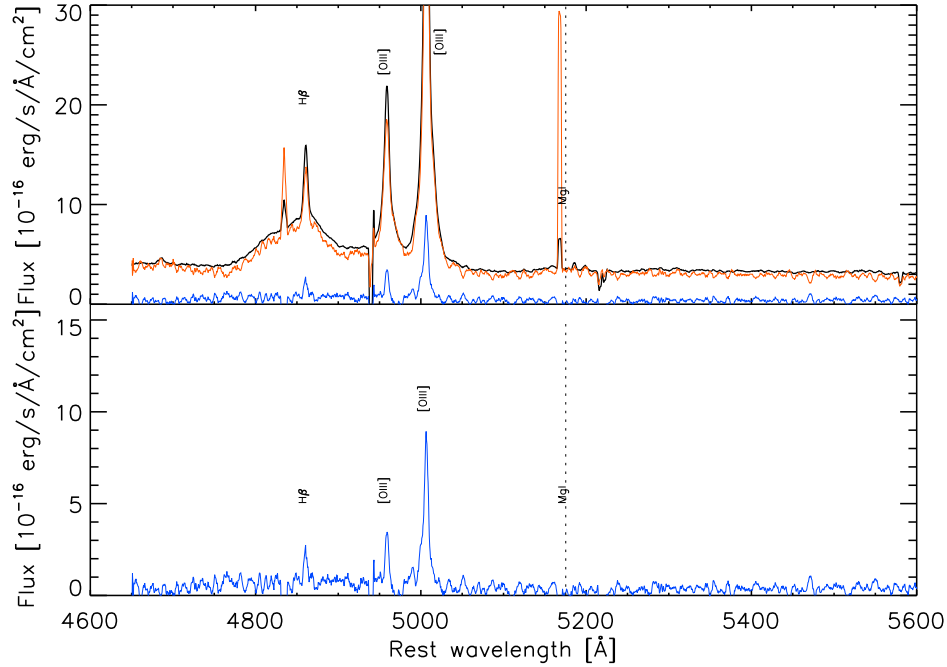


(a) Spectrum of HE 1405–1545 shows H β and [OIII] complex.

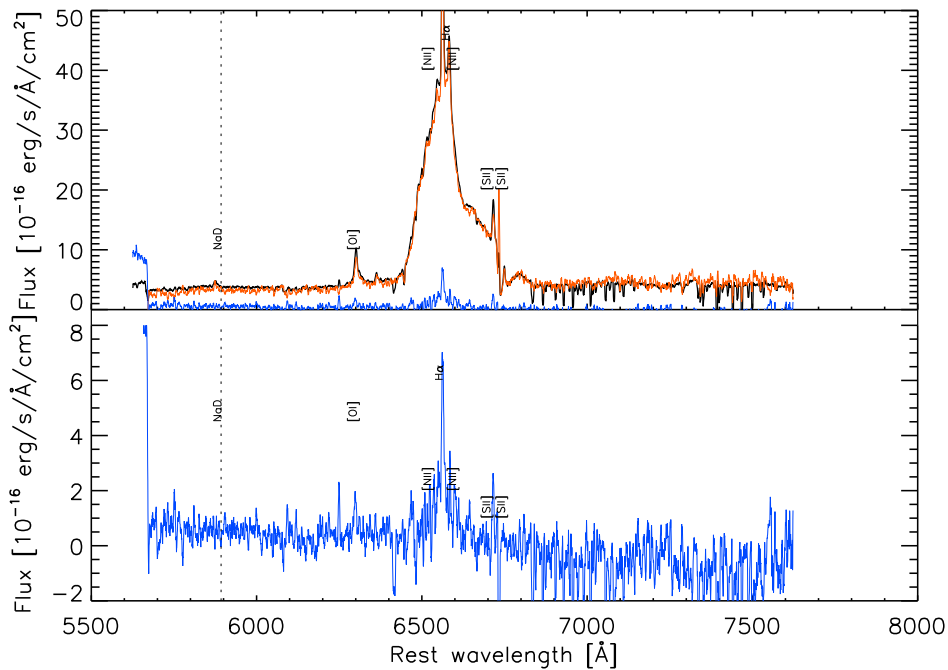


(b) Spectrum of HE 1405–1545 shows H α + [N II] complex.

Figure A.16: Quasar – host galaxy decomposition method for HE 1405–1545. (a) Spectrum with H β and [OIII] complex. (b) spectrum with H α + [N II] complex. Black: original spectrum, red: scaled nucleus spectrum, blue: host galaxy spectrum without broad-line emission. We show the host galaxy spectrum alone in the bottom panel for each figure for clarity.

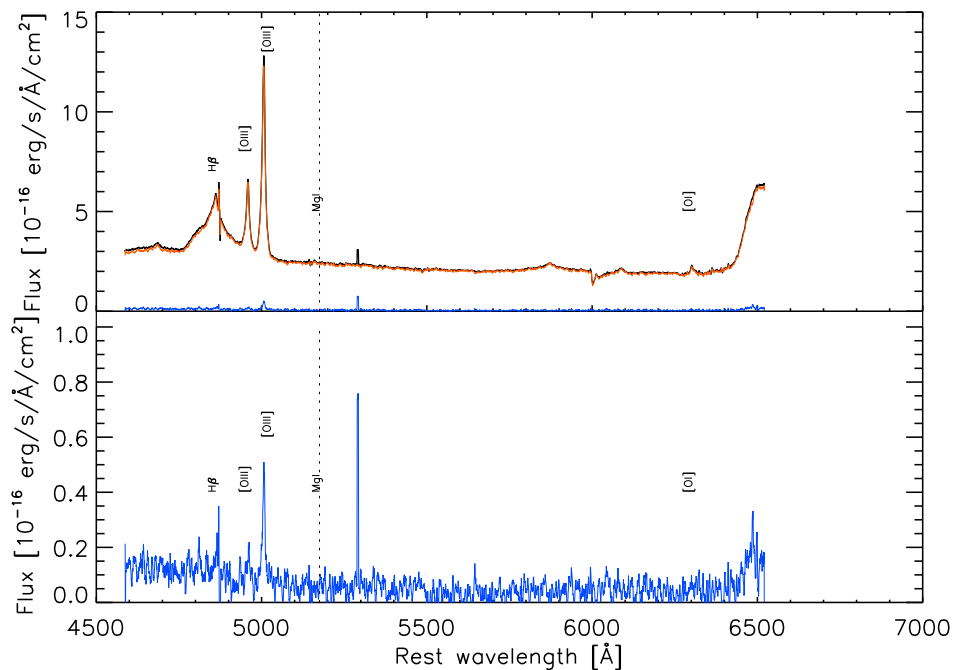


(a) Spectrum of HE 1416–1256 shows H β and [OIII] complex.

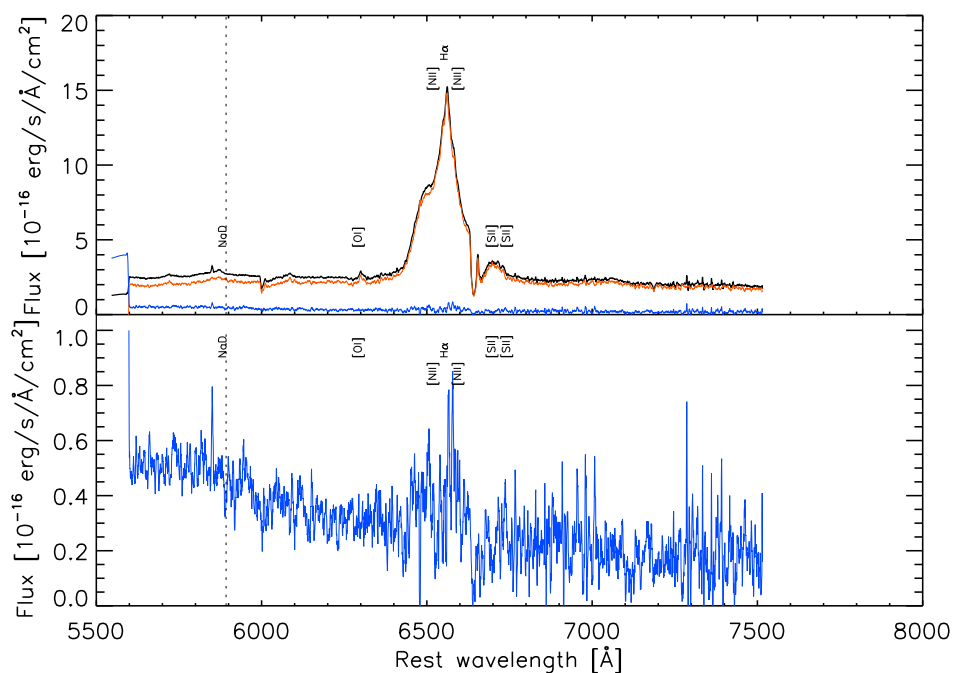


(b) Spectrum of HE 1416–1256 shows H α + [N II] complex.

Figure A.17: Quasar – host galaxy decomposition method for HE 1416–1256. (a) Spectrum with H β and [OIII] complex. (b) spectrum with H α + [N II] complex. Black: original spectrum, red: scaled nucleus spectrum, blue: host galaxy spectrum without broad-line emission. We show the host galaxy spectrum alone in the bottom panel for each figure for clarity.



(a) Spectrum of HE 1434–1600 shows $H\beta$ and [OIII] complex.



(b) Spectrum of HE 1434–1600 shows $H\alpha$ + [N II] complex.

Figure A.18: Quasar – host galaxy decomposition method for HE 1434–1600. (a) Spectrum with $H\beta$ and [OIII] complex. (b) spectrum with $H\alpha$ + [N II] complex. Black: original spectrum, red: scaled nucleus spectrum, blue: host galaxy spectrum without broad-line emission. We show the host galaxy spectrum alone in the bottom panel for each figure for clarity.



APPENDIX B: BLACK HOLE PARAMETER MEASUREMENTS

We describe the fitting method for black hole parameters determination from $H\beta$ and $[OIII]$ system for our quasar sample in Chapter 4 section 1.1.3. We present the best fit for each object in this Appendix. Black line is the original spectrum, Gaussian profiles in blue color are the best fit for $H\beta$ narrow line components, $[OIII]\lambda\lambda 4959, 5007$ lines and possible Fe complex. Gaussian profiles are different for each object depending on the shape of $[OIII]$ lines and strength of the Fe complex. Black line is nuclear spectrum, gaussian profiles in blue color are best fit for $H\beta$ narrow line components, $[OIII]\lambda\lambda 4959, 5007$ lines and possible Fe complex. The straight line is continuum determination and red filled circle shows the continuum flux at 5100\AA . As mentioned in section 1.1.3. we determine the line dispersion of $H\beta$ line from the green spectrum, produced from subtraction of gaussian profiles from the original nuclear spectrum.

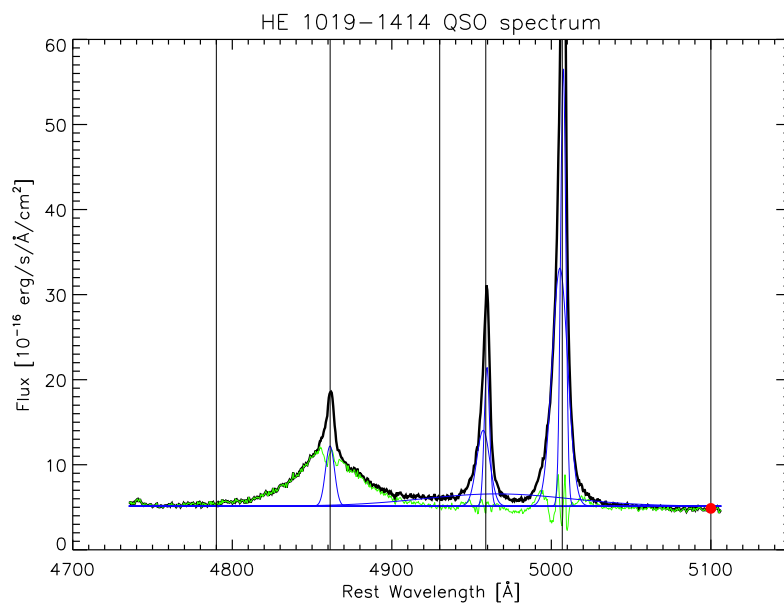


Figure B.1: Gaussians fitting for black hole parameter determination: HE 1019-1414.

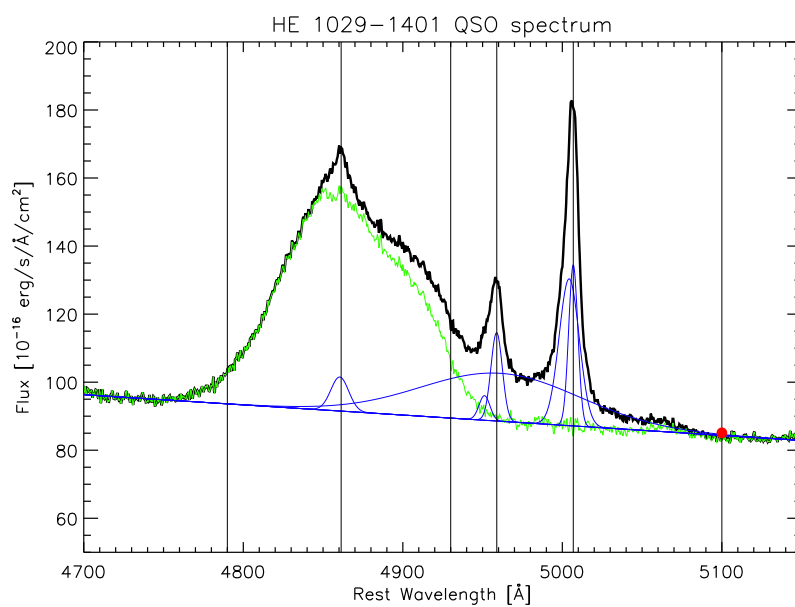


Figure B.2: Gaussians fitting for black hole parameter determination: HE 1029-1401.

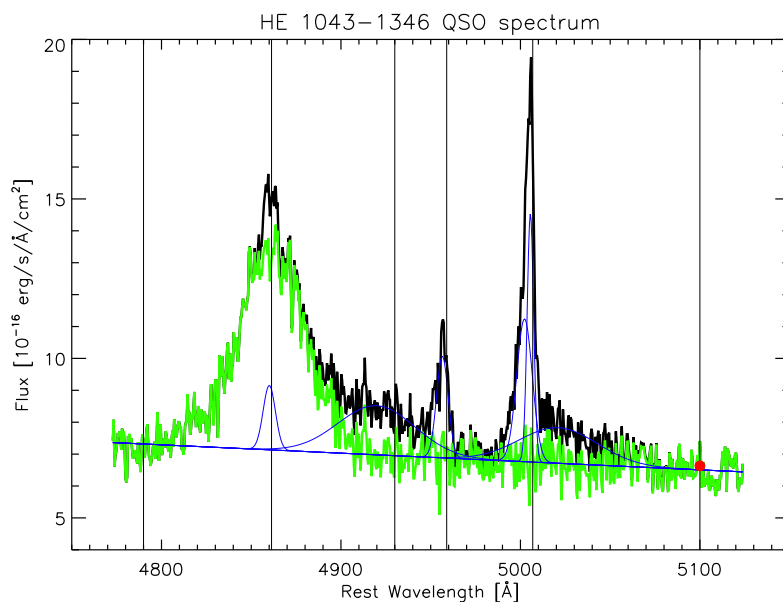


Figure B.3: Gaussians fitting for black hole parameter determination: HE 1043-1346.

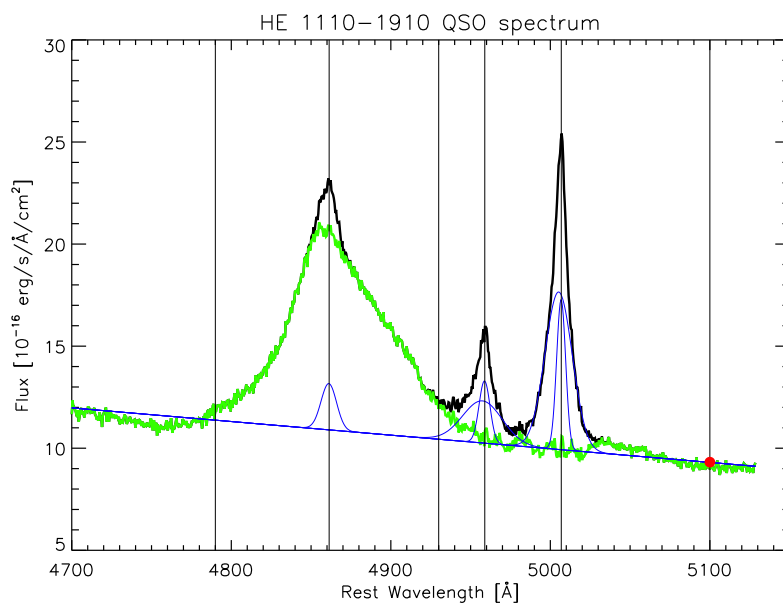


Figure B.4: Gaussians fitting for black hole parameter determination: HE 1110-1910.

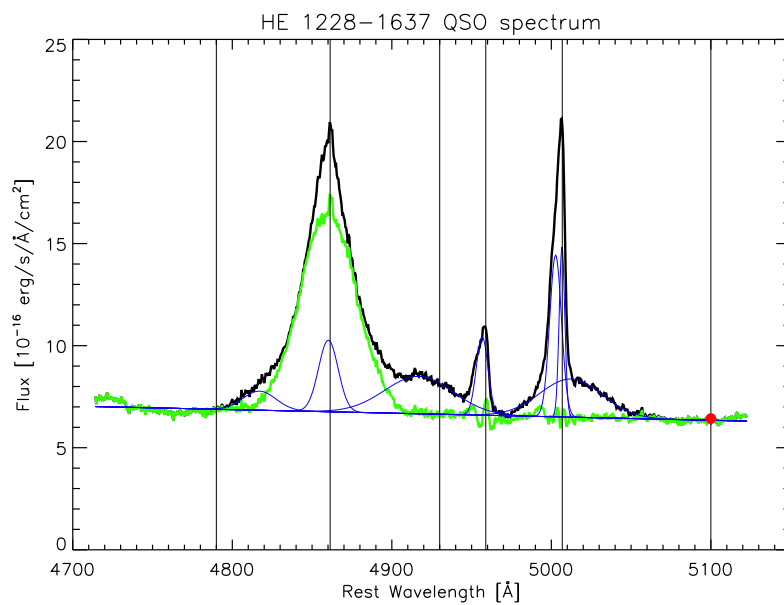


Figure B.5: Gaussians fitting for black hole parameter determination: HE 1228-1637.

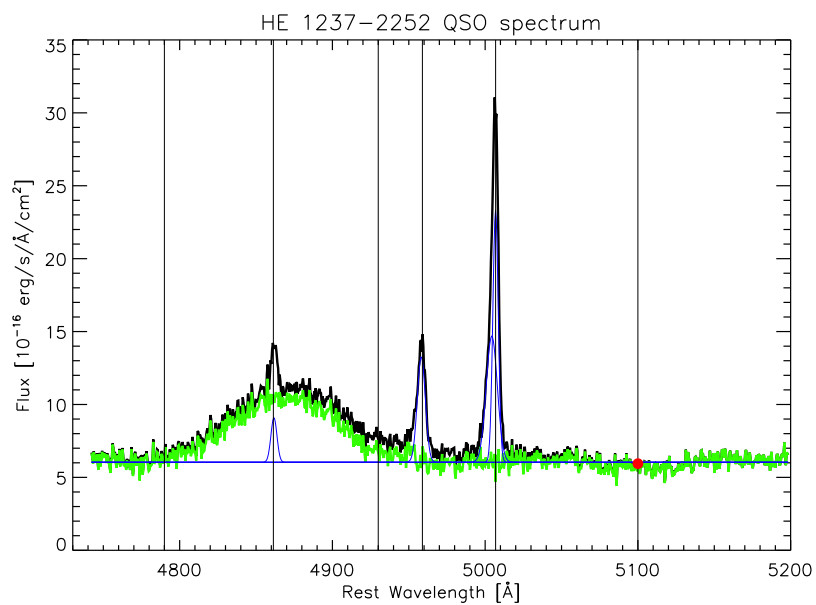


Figure B.6: Gaussians fitting for black hole parameter determination: HE 1237-2252.

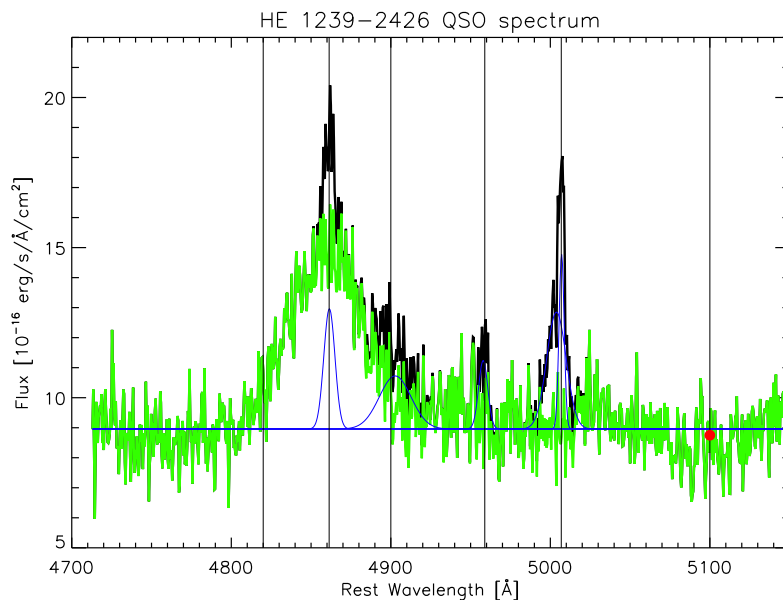


Figure B.7: Gaussians fitting for black hole parameter determination: HE 1239-2426.

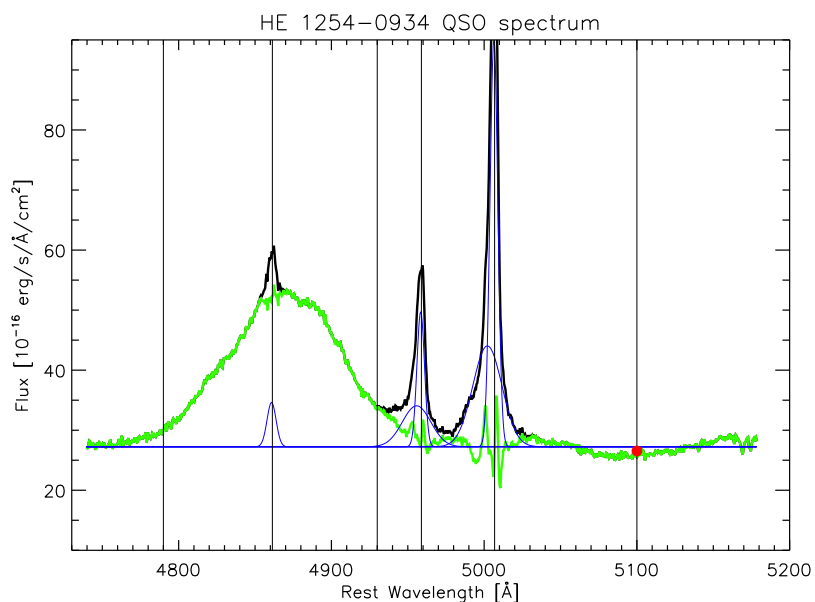


Figure B.8: Gaussians fitting for black hole parameter determination: HE 1254-0934.

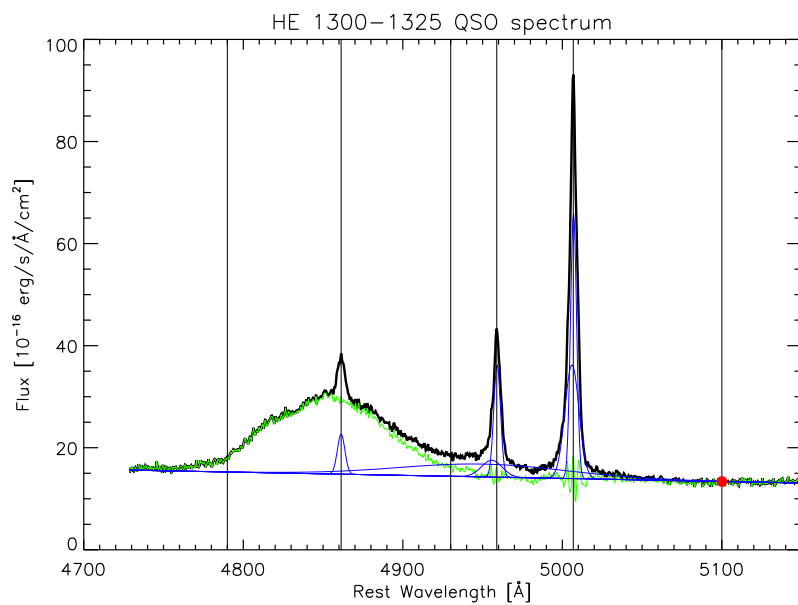


Figure B.9: Gaussians fitting for black hole parameter determination: HE 1300-1325.

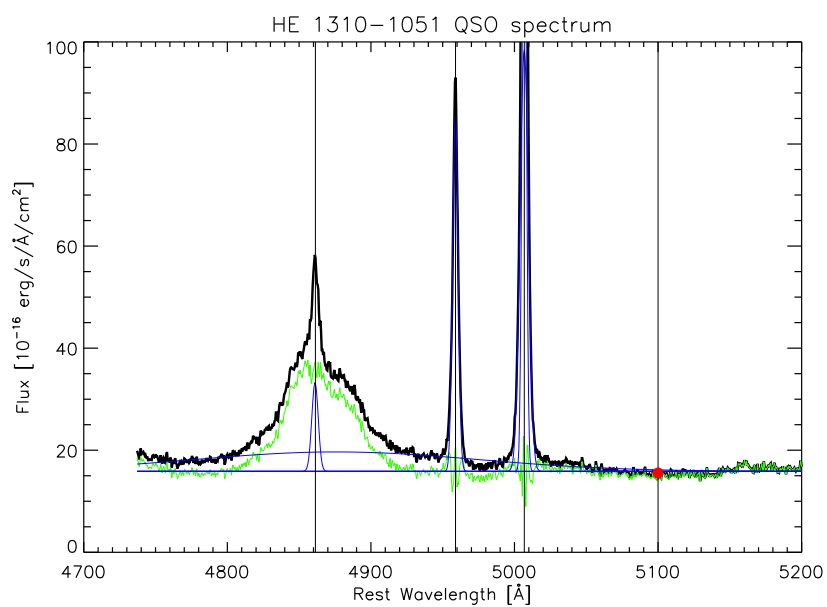


Figure B.10: Gaussians fitting for black hole parameter determination: HE 1310-1051.

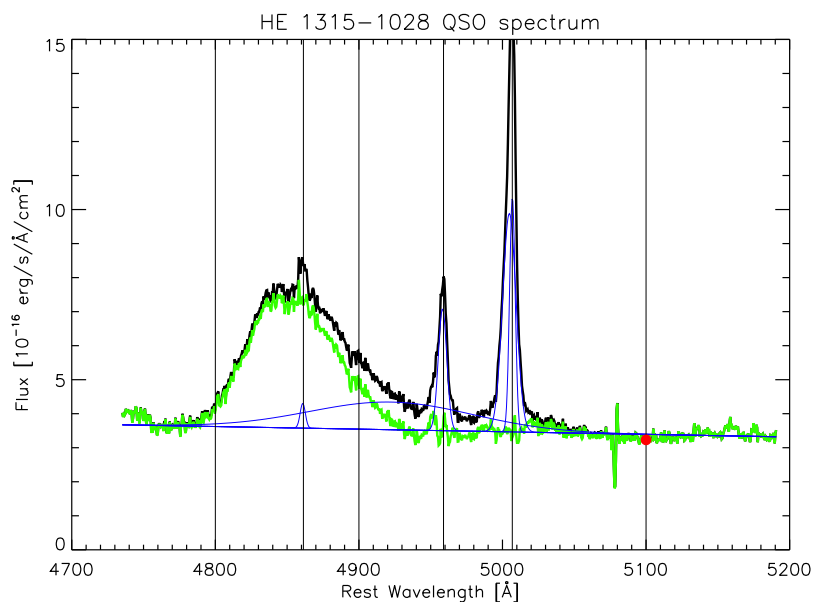


Figure B.11: Gaussians fitting for black hole parameter determination: HE 1315-1028.

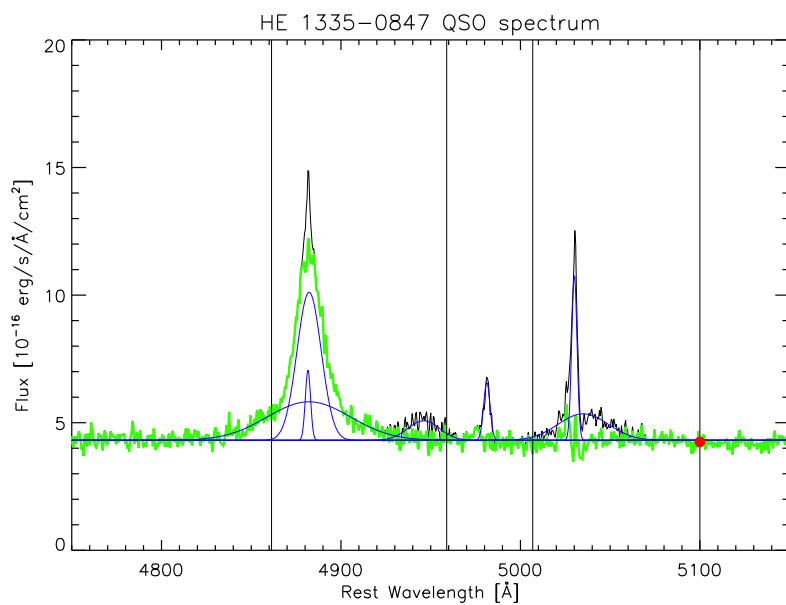


Figure B.12: Gaussians fitting for black hole parameter determination: HE 1335-0847.

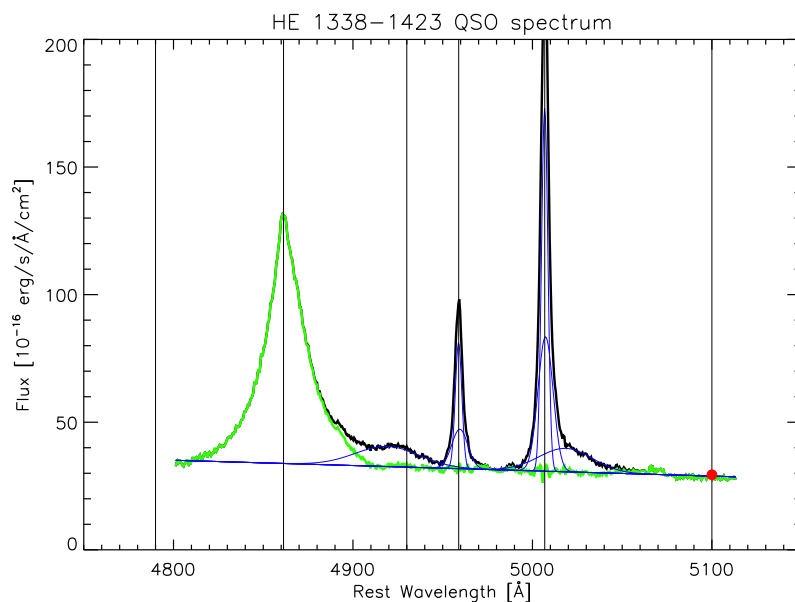


Figure B.13: Gaussians fitting for black hole parameter determination: HE 1338-1423.

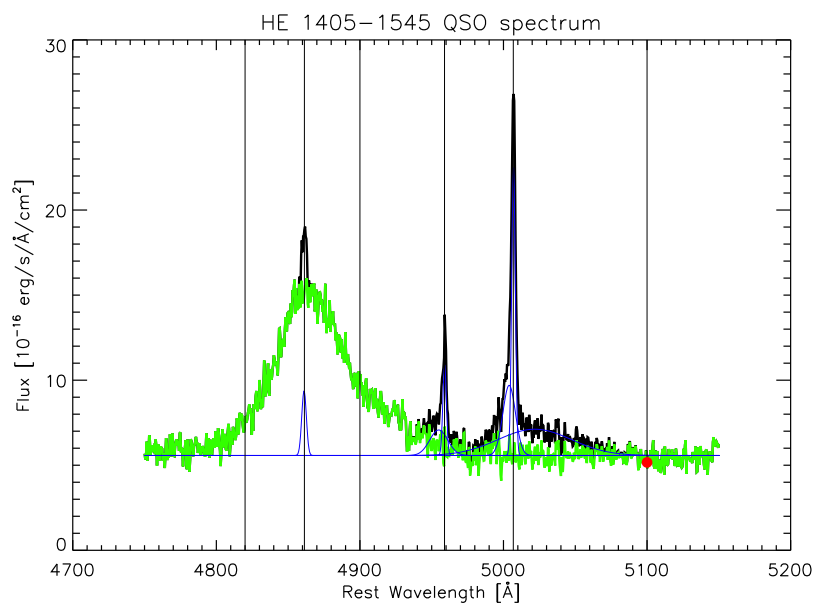


Figure B.14: Gaussians fitting for black hole parameter determination: HE 1405-1423.

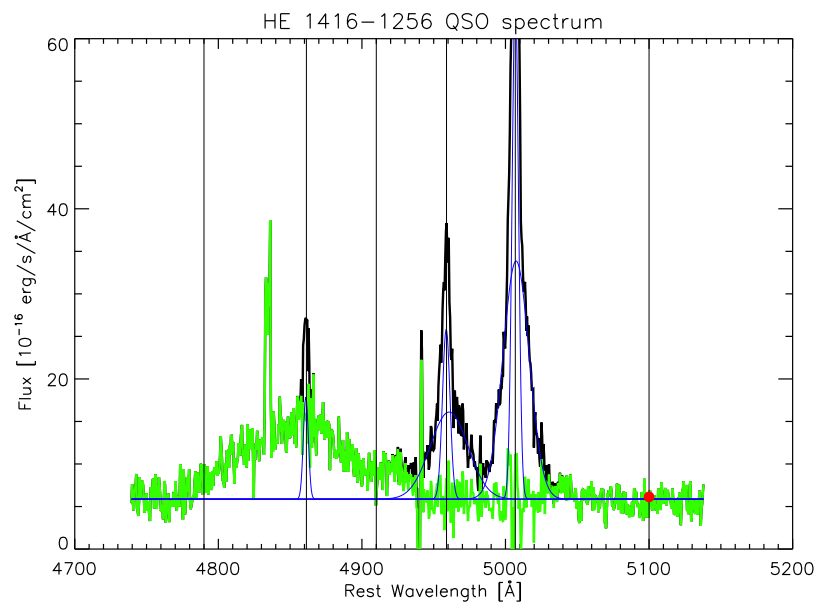


Figure B.15: Gaussians fitting for black hole parameter determination: HE 1416–1256.

BIBLIOGRAPHY

- Allington-Smith, J., & Content, R. 1998, *PASP*, 110, 1216
- Ambartsumian, V. A. 1971, in *Study Week on Nuclei of Galaxies*, ed. D. J. K. O'Connell, 9
- Bahcall, J. N., Kirhakos, S., Saxe, D. H., & Schneider, D. P. 1997, *ApJ*, 479, 642
- Baldry, I. K., Glazebrook, K., Brinkmann, J., Ivezić, Ž., Lupton, R. H., Nichol, R. C., & Szalay, A. S. 2004, *ApJ*, 600, 681
- Baldwin, J. A., Phillips, M. M., & Terlevich, R. 1981, *PASP*, 93, 5
- Bell, E. F., et al. 2004, *ApJ*, 608, 752
- Belokurov, V., et al. 2006, *ApJ*, 642, L137
- Benson, A. J. 2010, *Phys. Rep.*, 495, 33
- Bentz, M. C., Peterson, B. M., Netzer, H., Pogge, R. W., & Vestergaard, M. 2009, *ApJ*, 697, 160
- Blandford, R. D., Netzer, H., Woltjer, L., Courvoisier, T. J.-L., & Mayor, M., eds. 1990, *Active Galactic Nuclei*
- Burkert, A., & Tremaine, S. 2010, *ApJ*, 720, 516
- Cappellari, M., et al. 2011, *MNRAS*, 413, 813
- Christensen, L., Jahnke, K., Wisotzki, L., & Sánchez, S. F. 2006, *A&A*, 459, 717
- Cisternas, M., et al. 2011, *ApJ*, 726, 57
- Collin, S., Kawaguchi, T., Peterson, B. M., & Vestergaard, M. 2006, *A&A*, 456, 75
- Combes, F. 2001, in *Advanced Lectures on the Starburst-AGN*, ed. I. Aretxaga, D. Kunth, & R. Mújica, 223
- Decarli, R., Labita, M., Treves, A., & Falomo, R. 2008, *MNRAS*, 387, 1237
- Dumas, G., Mundell, C. G., Emsellem, E., & Nagar, N. M. 2007, *MNRAS*, 379, 1249
- Emsellem, E., et al. 2007, *MNRAS*, 379, 401

- Faber, S. M., et al. 2007, *ApJ*, 665, 265
- Fath, E. A. 1909, *Lick Observatory Bulletin*, 5, 71
- Ferrarese, L., & Merritt, D. 2000, *ApJ*, 539, L9
- Flores, H., Hammer, F., Puech, M., Amram, P., & Balkowski, C. 2006, *A&A*, 455, 107
- Gebhardt, K., et al. 2000, *ApJ*, 539, L13
- Genzel, R., Eckart, A., Ott, T., & Eisenhauer, F. 1997, *MNRAS*, 291, 219
- Green, P. J., Myers, A. D., Barkhouse, W. A., Mulchaey, J. S., Bennert, V. N., Cox, T. J., & Aldcroft, T. L. 2010, *ApJ*, 710, 1578
- Häring, N., & Rix, H.-W. 2004, *ApJ*, 604, L89
- Hopkins, P. F., & Quataert, E. 2010, *MNRAS*, 407, 1529
- Hopkins, P. F., et al. 2010, *ApJ*, 724, 915
- Hoyle, F., & Fowler, W. A. 1963, *Nature*, 197, 533
- Humason, M. L. 1932, *PASP*, 44, 267
- Husemann, B., Wisotzki, L., Sánchez, S. F., & Jahnke, K. 2008, *A&A*, 488, 145
- Ibata, R. A., Gilmore, G., & Irwin, M. J. 1995, *MNRAS*, 277, 781
- Jahnke, K., Kuhlbrodt, B., & Wisotzki, L. 2004a, *MNRAS*, 352, 399
- Jahnke, K., & Macciò, A. V. 2011, *ApJ*, 734, 92
- Jahnke, K., Wisotzki, L., Courbin, F., & Letawe, G. 2007, *MNRAS*, 378, 23
- Jahnke, K., Wisotzki, L., Sánchez, S. F., Christensen, L., Becker, T., Kelz, A., & Roth, M. M. 2004b, *Astronomische Nachrichten*, 325, 128
- Jogee, S. 2006, in *Physics of Active Galactic Nuclei at all Scales*, edited by Danielle Alloin, Rachel Johnson and Paulina Lira. *Lecture Notes in Physics*, Vol. 693. ISBN-10 3-540-31207-2; ISBN-13 978-3-540-31207-9; ISSN 0075-8450. Library of Congress Catalog Card No. 2006925838. Published by Springer, Berlin and Heidelberg, 2006, p.143, ed. D. Alloin, Vol. 693, 143
- Kaspi, S., Smith, P. S., Netzer, H., Maoz, D., Jannuzi, B. T., & Giveon, U. 2000, *ApJ*, 533, 631
- Kauffmann, G., et al. 2003, *MNRAS*, 346, 1055
- Kelly, B. C., & Bechtold, J. 2007, *ApJS*, 168, 1
- Kewley, L. J., Dopita, M. A., Sutherland, R. S., Heisler, C. A., & Trevena, J. 2001, *ApJ*, 556, 121
- Koehler, T., Groote, D., Reimers, D., & Wisotzki, L. 1997, *A&A*, 325, 502
- Kormendy, J., & Richstone, D. 1992, *ApJ*, 393, 559
- . 1995, *ARA&A*, 33, 581
- Krajnović, D., Cappellari, M., de Zeeuw, P. T., & Copin, Y. 2006, *MNRAS*, 366, 787
- Kronberger, T., Kapferer, W., Schindler, S., Böhm, A., Kutdemir, E., & Ziegler, B. L. 2006,

- A&A, 458, 69
- Le Fèvre, O., et al. 2003, in Presented at the Society of Photo-Optical Instrumentation Engineers (SPIE) Conference, Vol. 4841, Society of Photo-Optical Instrumentation Engineers (SPIE) Conference Series, ed. M. Iye & A. F. M. Moorwood, 1670–1681
- Letawe, G., Magain, P., Courbin, F., Jablonka, P., Jahnke, K., Meylan, G., & Wisotzki, L. 2007, *MNRAS*, 378, 83
- Lotz, J. M., Jonsson, P., Cox, T. J., & Primack, J. R. 2008, *MNRAS*, 391, 1137
- Lynden-Bell, D. 1969, *Nature*, 223, 690
- Mackey, A. D., et al. 2010, *ApJ*, 717, L11
- Magorrian, J., et al. 1998, *AJ*, 115, 2285
- Marconi, A., & Hunt, L. K. 2003, *ApJ*, 589, L21
- Markwardt, C. B. 2009, in *Astronomical Society of the Pacific Conference Series*, Vol. 411, *Astronomical Data Analysis Software and Systems XVIII*, ed. D. A. Bohlender, D. Durand, & P. Dowler, 251
- Martínez-Delgado, D., Peñarrubia, J., Gabany, R. J., Trujillo, I., Majewski, S. R., & Pohlen, M. 2008, *ApJ*, 689, 184
- Martini, P. 2004, in *IAU Symposium*, Vol. 222, *The Interplay Among Black Holes, Stars and ISM in Galactic Nuclei*, ed. T. Storchi-Bergmann, L. C. Ho, & H. R. Schmitt, 235–241
- McLure, R. J., Kukula, M. J., Dunlop, J. S., Baum, S. A., O’Dea, C. P., & Hughes, D. H. 1999, *MNRAS*, 308, 377
- Peng, C. Y. 2007, *ApJ*, 671, 1098
- Peterson, B. M. 1997, *An Introduction to Active Galactic Nuclei*
- Peterson, B. M., et al. 2004, *ApJ*, 613, 682
- Pych, W. 2004, *PASP*, 116, 148
- Reimers, D., Koehler, T., & Wisotzki, L. 1996, *A&AS*, 115, 235
- Rubin, V. C., Waterman, A. H., & Kenney, J. D. P. 1999, *AJ*, 118, 236
- Salpeter, E. E. 1964, *ApJ*, 140, 796
- Sánchez, S. F., García-Lorenzo, B., Jahnke, K., Mediavilla, E., González-Serrano, J. I., Christensen, L., & Wisotzki, L. 2006, *Astronomische Nachrichten*, 327, 167
- Sánchez, S. F., et al. 2012, *A&A*, 538, A8
- Sanders, D. B., Soifer, B. T., Elias, J. H., Madore, B. F., Matthews, K., Neugebauer, G., & Scoville, N. Z. 1988a, *ApJ*, 325, 74
- Sanders, D. B., Soifer, B. T., Elias, J. H., Neugebauer, G., & Matthews, K. 1988b, *ApJ*, 328, L35
- Sarzi, M., et al. 2006, *MNRAS*, 366, 1151
- Schulze, A., Wisotzki, L., & Husemann, B. 2009, *A&A*, 507, 781
- Slipher, V. M. 1917, *Lowell Observatory Bulletin*, 3, 59

- Snyder, G. F., Hopkins, P. F., & Hernquist, L. 2011, *ApJ*, 728, L24
- Sofue, Y., Tutui, Y., Honma, M., Tomita, A., Takamiya, T., Koda, J., & Takeda, Y. 1999, *ApJ*, 523, 136
- Swaters, R. A., Sancisi, R., van Albada, T. S., & van der Hulst, J. M. 2009, *A&A*, 493, 871
- Toomre, A., & Toomre, J. 1972, *ApJ*, 178, 623
- Urry, C. M., & Padovani, P. 1995, *PASP*, 107, 803
- van de Ven, G., & Fathi, K. 2010, *ApJ*, 723, 767
- Veilleux, S., & Osterbrock, D. E. 1987, *ApJS*, 63, 295
- Wisotzki, L., Christlieb, N., Bade, N., Beckmann, V., Köhler, T., Vanelle, C., & Reimers, D. 2000, *A&A*, 358, 77
- Wisotzki, L., Koehler, T., Grootte, D., & Reimers, D. 1996, *A&AS*, 115, 227
- Zanichelli, A., et al. 2005, *PASP*, 117, 1271
- Zel'dovich, Y. B. 1964, *Soviet Physics Doklady*, 9, 195